EXAMINING THE RELIABILITY OF THE NORTHEAST U.S. HEAVY SNOW CONCEPTUAL MODEL

Chad M. Gravelle, B.S., M.S. (R)

An Abstract Presented to the Graduate Faculty of
Saint Louis University in Partial Fulfillment
of the Requirements for the Degree of
Doctor of Philosophy

2011

Abstract

A 28-yr climatology and conceptual model of coastal-track Northeast heavy snow events, objectively identified near-miss coastal-track Northeast heavy snow events, and distinguishing characteristics between the conceptual model and near-miss events are presented. Over the 28 winters (December–February) between 1 December 1980 and 29 February 2008, 500 organized snowfall events (>2″) affected the northeastern United States. Forty-one of eighty heavy snowfall events (one standard deviation or greater snowfall) associated with a coastal surface cyclone track were composited to create a quantitative conceptual model. Using the conceptual model, 25 near-miss events were objectively identified and analyzed. A majority (62%) of coastal-track surface lows similar to the conceptual model produce heavy snow in the Northeast. Although the near-miss event synoptic patterns were similar to the conceptual model, they were associated with a progressive upper-level trough and weaker low-level mass fields. The differences in the low-level mass fields were statistically significant and the 850-hPa *u*- component of the wind was the most distinguishing characteristic.

EXAMINING THE RELIABILITY OF THE NORTHEAST U.S. HEAVY SNOW CONCEPTUAL MODEL

Chad M. Gravelle, B.S., M.S. (R)

A Dissertation Presented to the Graduate Faculty of
Saint Louis University in Partial Fulfillment
of the Requirements for the Degree of
Doctor of Philosophy

2011

COMMITTEE IN CHARGE OF CANDIDACY:

Associate Professor Charles E. Graves,
Chairperson and Advisor

Adjunct Assistant Professor Marty A. Baxter

Assistant Professor Timothy P. Eichler

Table of Contents

List of Tables

List of Figures

Chapter 1. Statement of the Problem

Winter weather, in particular heavy snow, significantly impacts the United States' society and economy. Between 1949 and 2000, on average two snowstorms per year produced losses greater than $35 million and those that affected the eastern portion of the United States exceeded $18 billion (Changnon and Changnon 2006). Annually, flight delays due to heavy snow cost the airline industry $3.2 billion with over $2 billion of the total spent on snow removal (Adams et al. 2004). Therefore, one of the goals of the National Oceanic and Atmospheric Administration's (NOAA) strategic plan for the 21st century is to provide information, services, and products that support the United States society and economy with safe and efficient transportation systems (NOAA 2005). One of NOAA's performance objectives is to increase the accuracy of winter storm warnings from 90% to 92% by 2014, which can reduce economic impacts. Each winter, improved forecasts can save over $600 million at United States airports and $29 million by authorizing the rerouting of trucks (Adams et al. 2004).

Early research on improving snowfall forecasting was initiated by the lack of success in identifying these high-impact events (Mook and Norquest 1956; Goree and Younkin 1966). These studies focused on using low- and midlevel mass fields to assist in forecasting snowfall (e.g., Goree and Younkin 1966; Browne and Younkin 1970). Case studies that centered around major snowstorms that affected the East Coast during the 1980s and early 1990s such as the February 1983 "Megalopolitan Snowstorm" (Sanders and Bosart 1985b,a; Bosart and Sanders 1986) and the March 1993 "Superstorm" (e.g., Gilhousen 1994; Kocin et al. 1995; Uccellini et al. 1995; Caplan 1995; Huo et al. 1995; Bosart et al. 1996)

led to a compilation of articles focused on winter weather forecasting in the eastern United States (Maglaras et al. 1995; Gurka et al. 1995; Keeter et al. 1995; Niziol et al. 1995). These case studies, and other operational research (e.g., Nicosia and Grumm 1999; Banacos 2003; Moore et al. 2005), have also shown the importance that the mesoscale environment has on heavy snowfall. Through their conceptual models (hereafter CM) and climatological composite studies (e.g., Novak et al. 2004; Thomas and Martin 2007) better forecast strategies for heavy snowfall were developed (Novak et al. 2006).

Even though snowfall forecasting has greatly improved over the last half century, due to in part from better identification of high-impact events and numerical weather prediction (NWP) advances (Olsen et al. 1995), many snowfall events continue to be missed (over or under snowfall forecasting, hereinafter termed "snow busts"). For example, in December 1982 an unforecast band of light snowfall occurred from the Ohio Valley into western New York (Gyakum 1987), and in December 1988 a heavy mesoscale north-south oriented snow swath occurred over Long Island into interior New England that was not forecast (Maglaras et al. 1995). There has been extensive research on the "surprise" snowstorm along the East Coast that occurred in January 2000 (Langland et al. 2002; Zhang et al. 2002; Kleist and Morgan 2005; Durnford et al. 2009). Even with the aforementioned improvements in quantitative precipitation forecasts (QPF), the accuracy of heavy snow forecasts remain challenging.

A significant factor that influences forecast accuracy is forecaster experience, especially when the experience is gained in the same area over an extended period of time (Schmit and Hultquist 2009). A portion of this experience can be gained with exposure to regional CMs and climatological composite studies. These methods that utilize past events can improve forecasting skill, multitasking

ability, and situational awareness (Stuart et al. 2006). In particular, by using CMs, forecasters can become familiar with the atmospheric signals that are typically associated with significant winter storms in their region (Schmit and Hultquist 2009). When these high-impact events are imminent, forecasters with experience add the most value to computer-generated model guidance (Stuart et al. 2006).

The extensive number of CMs in published literature suggest their value. However, the predictive ability of CMs is rarely, if ever, tested. The major objectives of this research are to:

- develop and test an algorithm for objectively identifying null events similar to the Northeast heavy snow CM.
- identify distinguishing characteristics between the Northeast heavy snow CM and null events.
- determine the climatological frequency of Northeast heavy snow events.

A forecaster who is anticipating a heavy snowfall event unfolding, as depicted in the CM, does not know which fields in the CM are the critical for heavy snowfall. For example, Kocin and Uccellini (2005) state that moderate and heavy snowstorms along the East Coast have similar upper-level patterns and jet streaks. This suggests that the upper-level support associated with the CM for heavy East Coast snowstorms is a necessary but not a sufficient condition for heavy snowfall. These fields could be identified by comparing and contrasting the Northeast heavy snow CM and the subset of "null events" to determine if distinguishing characteristics exist. The results of this analysis could increase the value of the CM by focusing the forecasters attention on fields that may prevent the CM from verifying.

Chapter 2. Literature Review

2.1 Ingredients for Heavy Snow

An ingredients-based methodology (IM) approach to operational forecasting uses understood fundamental processes by providing focus on aspects of a particular weather phenomena that are relevant.(Schultz et al. 2002). In a strictly general framework, an ingredient is defined to be a necessary item that is clearly associated with a particular event. For example, heavy snow is associated with forcing for ascent, but the specific forcing can be from many different processes (e.g., large-scale ascent, frontogenesis, warm conveyor belt). The sufficiency of an ingredient is also essential, where the absence of the ingredient prevents the event but the sole presence of the ingredient is not enough to produce the event (Schultz et al. 2002).

For winter weather events, and specifically heavy snowfall, an IM was developed by Nietfeld and Kennedy (1998). This IM focused on snowfall rate, air temperature, and snowfall duration as the key ingredients. Their results indicate that the Garcia Method had better snowstorm verification over other methods because snowfall rate and duration are directly considered. The main ingredients in the IM for mid-latitude winter precipitation by Wetzel and Martin (2001) are forcing for ascent (e.g., Q-vector convergence and frontogenesis), moisture and saturation (e.g., mixing ratio and relative humidity), instability (i.e., gravitational, inertial, or slantwise), precipitation efficiency (i.e., cloud microphysics), and temperature. Wetzel and Martin (2001) state that their IM is useful for the assessment and evaluation of model-generated quantitative precipitation forecasts because their ingredients are based on the processes that

produce winter weather events. The Wetzel and Martin (2001) ingredients for mid-latitude winter precipitation are the primary focus of section 2.1.

2.1.1 Forcing For Ascent

Quasi-geostrophic (QG) vertical motion can be diagnosed using either the standard form of the QG ω-equation (Bluestein 1992) or the Q-vector form of the QG ω-equation (Hoskins et al. 1978). The standard form has two primary forcing terms: differential absolute vorticity advection and the Laplacian of thermal advection. The Q-vector form is defined as the local rate of change of the potential temperature gradient with respect to a parcel trajectory moving with the geostrophic wind (Hoskins et al. 1978). Keyser et al. (1992) and Martin (1999) showed that the Q-vector could be broken into across- (Q_n) and along-isentrope (Q_s) components to describe changes in the magnitude and direction of the potential temperature gradient. Wetzel and Martin (2001) stated that the Q-vector approach has become common in operational forecasting, and it has been shown to be related to the QG vertical motion field in both theoretical and operational environments (Hoskins et al. 1978; Keyser et al. 1992; Martin 1999). Finally, it should be noted that the assumption that parcel motion is nearly geostrophic suggests that Q-vectors are only valid for synoptic-scale motions.

Midlevel frontogenesis can enhance and sustain heavy snowfall by increasing upward vertical motion on the meso-alpha scale (i.e., 200–2000 km). Petterssen (1956) defined atmospheric frontogenesis as the temporal rate of change along a parcel trajectory of the magnitude of the horizontal potential temperature gradient, shown below:

$$\frac{d}{dt}|\nabla\theta| = \left(\frac{\partial}{\partial t} + u\frac{\partial}{\partial x} + v\frac{\partial}{\partial y}\right)\left(\frac{\partial\theta}{\partial x} + \frac{\partial\theta}{\partial y}\right) \tag{2.1}$$

This is often referred to as the "frontogenesis function." Frontogenesis is often associated with (but not limited to) the deformation zone, an area of the atmosphere where stretching and shearing deformation are large, often found in the northwest quadrant of a mid-latitude cyclone.

Petterssen (1956) developed a two-dimensional, scalar frontogenetic function (an abbreviated version of the Miller [1948] frontogenetic function) to calculate frontogenesis:

$$F = \frac{1}{2}|\nabla\theta|(Def_r\cos(2b) - DIV) \tag{2.2}$$

where $|\nabla\theta|$ is the magnitude of the potential temperature gradient, Def_r represents the resultant deformation, b is the angle between the isentropes and the axis of dilatation, and *DIV* is divergence. According to (2.2), frontogenesis (F>0) occurs in regions of stretching and shearing deformation of the horizontal wind field, and/or when there is convergence (DIV < 0). It is evident that frontogenesis is highly dependent on the angle between the isentropes and the axis of dilatation (Fig. 2.1). For frontogenesis to occur in a pure stretching deformation environment, the angle b must be between 0° and 45°. For frontolysis to occur, b must lie between 45° and 90°. Frontogenesis is maximized when the axis of dilatation is parallel to the isentropes in a deformation environment (Nicosia and Grumm 1999).

Vertical motions associated with frontogenesis can occur as a result of strengthening the horizontal temperature gradient through geostrophic confluence. Increasing the horizontal temperature gradient disrupts thermal

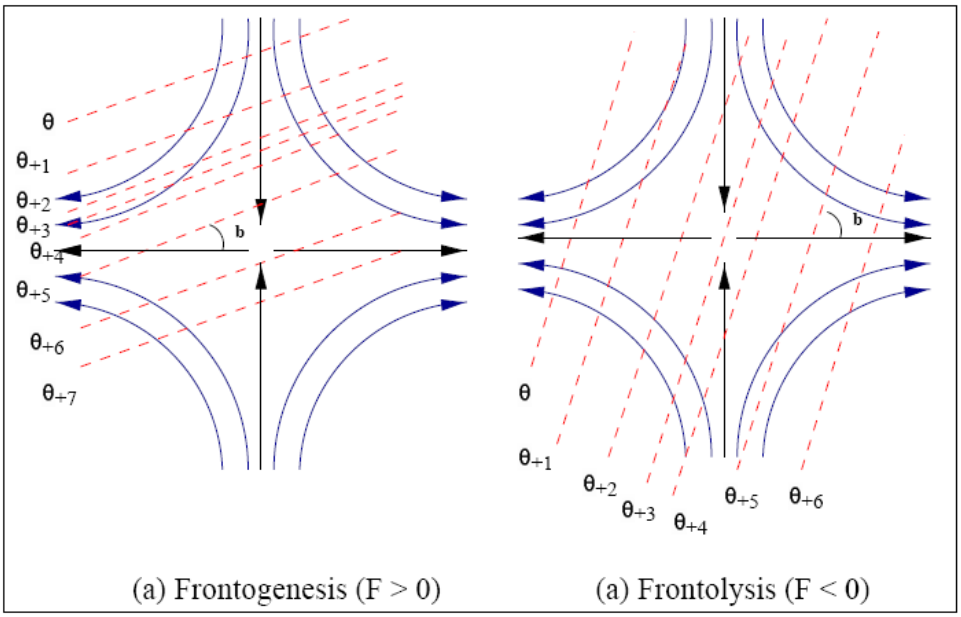

Figure 2.1: Relationship between the axis of dilitation (x-axis) and the isentropes (dashed, red) as determined by the angle (*b*). Streamlines (arrows, blue) are shown strengthening (left; frontogenesis) and weakening (right; frontolysis) the thermal gradient. From Bluestein (1993, p. 252); after Petterssen (1956).

wind balance, and the atmosphere responds by creating a vertical ageostrophic circulation. The resulting direct thermal circulation (DTC) attempts to restore thermal wind balance and weaken the horizontal frontal zone (Sanders and Bosart 1985b; Moore and Blakley 1988; Holton 1992; Carlson 1998).

2.1.2 Instability

Heavy precipitation events often display a spectrum of mesoscale instabilities concurrently, illustrated in Fig. 2.2: Convective Instability (CI), Conditional Symmetric Instability (CSI), and Weak Symmetric Stability (WSS). (In Fig. 2.2, WSS is represented as the region labeled 'NS' [neutral stability].) These mesoscale instabilities have a tendency to develop from south to north in the presence of strong unidirectional wind shear on the equatorward side of an

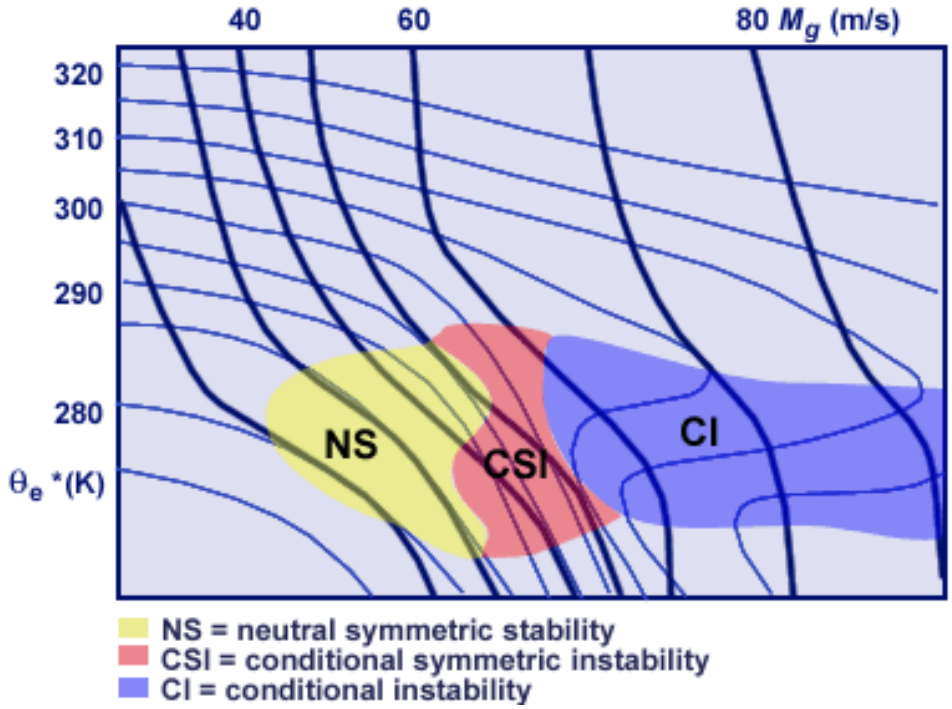

Figure 2.2: Stability regimes often observed near frontal zones. Contours represent typical values of M_g (thick black lines) and θ_e (thin blue lines). Based on a figure originally constructed by James Moore and Sean Nolan. From Schultz and Schumacher (1999, p. 2718).

upper-level jet streak. CI usually develops in the warm, moist air to the south and southeast of the cyclone, while CSI and WSS tend to develop further north in the presence of a cold, stable boundary layer. Occasionally CSI may be a precursor to elevated CI as the vertical circulation associated with CSI may overturn θ_e surfaces with time, thereby creating a convectively unstable zone aloft.

It has been recognized since the early part of the 20th century that precipitation is often organized in bands (Bjerknes 1919) and later suggested by Bennetts and Hoskins (1979) that these bands may materialize due to symmetric baroclinic instability. The bands develop in the form of rolls that are oriented along the thermal wind, with their circulation often generating conditional gravitational instability at midlevels (∼600–700 hPa). Here, the term conditional

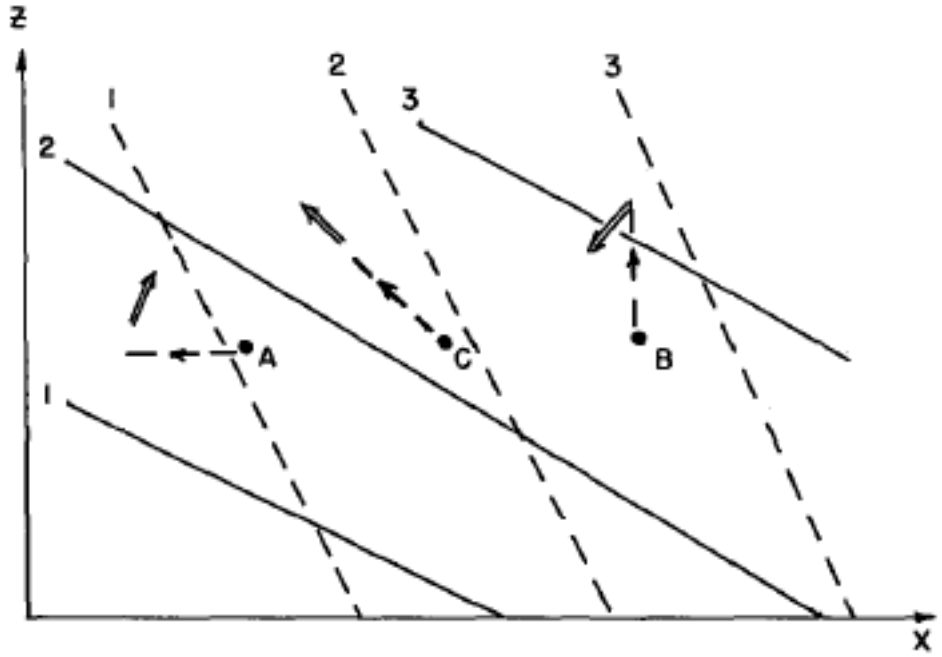

Figure 2.3: Schematic vertical cross-section demonstrating parcels in an inertially and convectively stable environment. Dashed lines represent constant θ_e surfaces, while the solid lines represent constant M_g surfaces of basic flow. Lettered points show sample displacements (dashed) and accelerations (arrowheads). From Sanders and Bosart (1985b, p. 1053).

is used because the atmosphere needs to be at or near saturation for the instability to be released.

Emanuel (1985) demonstrated that the circulations associated with CSI are mesoscale in nature and that they are a combination of gravitational and inertial forces acting vertically and horizontally to yield a slantwise displacement. CSI represents the circulation from both forces that result in a slantwise motion where inertial energy is converted into buoyant energy. Furthermore, the author stated that a parcel could be stable with respect to purely vertical or horizontal displacements but unstable to slantwise displacements (Fig. 2.3).

CSI can be qualitatively evaluated by comparing the slope of the saturated equivalent potential temperature (θ_{es}) surfaces to the slope of the absolute geostrophic momentum (M_g; defined below) surfaces. CSI is diagnosed in

regions where the M_g surfaces are more horizontal than θ_{es} surfaces, as in Fig. 2.2 (Schultz and Schumacher 1999) and Fig. 2.3 (Sanders and Bosart 1985b). The absolute geostrophic momentum for the environment can be defined in the following equation:

$$M_g = v_g + fx \tag{2.3}$$

where v_g is the geostrophic wind component normal to the thermal gradient, f is the Coriolis parameter, and x is the distance along the x-axis increasing toward the warm air.

CSI is illustrated by Sanders and Bosart (1985b) in a schematic vertical cross-section of an inertially and convectively stable environment (Fig. 2.3). The dashed lines represent constant θ_e surfaces, while the solid lines represent constant M_g surfaces. (Note: since θ_{es} is not used in this cross-section as Schultz and Schumacher [1999] have suggested, the assumption is made that in order for CSI to occur the relative humidity [RH] must be greater than 80% ; see Halcomb and Market [2003]). In Fig. 2.3, parcel A has a horizontal displacement that results in larger M_g and θ_e than the environment. The inertial and gravitational forces are in equilibrium and in time will restore the parcel to its original position. Parcel B has a vertical displacement, causing the parcel to have smaller M_g and θ_e than the environment. Again, inertial and gravitational forces are in equilibrium and the parcel will return to its original position. Parcel C is given a slantwise displacement (e.g., frontogenetical circulation). Here, the parcel is inertially and convectively unstable which allows the parcel to accelerate in a slantwise direction. In these examples, parcels that are given purely horizontal or vertical displacements are stable while parcels that are given slantwise

displacements are unstable.

A more convenient way to diagnose CSI is to use equivalent potential vorticity (EPV), which is defined as:

$$EPV = -\vec{\eta} \cdot \vec{\nabla}\theta_e \tag{2.4}$$

where $\vec{\eta}$ is the three-dimensional absolute vorticity vector, $\vec{\nabla}$ is the gradient operator in x, y, and p coordinates, and θ_e is the equivalent potential temperature. Moore and Lambert (1993) expanded (2.4) as:

$$EPV = g\left[\left\{\frac{\partial M_g}{\partial p}\frac{\partial \theta_e}{\partial x}\right\} - \left\{\frac{\partial M_g}{\partial x}\frac{\partial \theta_e}{\partial p}\right\}\right] \tag{2.5}$$

where g is the gravitational acceleration, M_g is the geostrophic absolute momentum, θ_e is the equivalent potential temperature, and p is pressure. The gravitational acceleration is multiplied through to ensure that EPV is expressed in potential vorticity units (PVU), where:

$$1\,PVU = 1 \times 10^{-6} K m^2 kg^{-1} s^{-1} \tag{2.6}$$

The first term in (2.5) is the contribution from the vertical wind shear and the horizontal θ_e gradient to EPV. If the environment is saturated, CSI is favored when θ_e increases in the x-direction ($\partial\theta_e/\partial x > 0$) and the vertical wind shear is large ($\partial M_g/\partial p < 0$). In the second term, the absolute vorticity is almost always positive ($\partial M_g/\partial x > 0$) so if the stability ($\partial\theta_e/\partial p$) is small then the second term is only partially working against the first term. However, if CI exists ($\partial\theta_e/\partial p > 0$) then EPV is more negative.

Moore and Lambert (1993) have shown that CSI can be diagnosed in regions

where EPV < 0 in a convectively stable environment with RH values greater than 80%. However, it has been shown that EPV can also be negative in regions of CI. Under these conditions, upright convection will dominate because slantwise convection (associated with the release of CSI) can take a few hours to develop, while upright convection (via the release of CI) can occur within tens of minutes. Even though both CSI and CI can be associated with heavy banded snow, as in Nicosia and Grumm (1999), it is important to distinguish between the two.

One way to differentiate between the two instabilities is to look at a cross-section using θ_e and M_g. In Fig. 2.2, the Schultz and Schumacher (1999) CM demonstrates that CSI occurs where M_g surfaces are flatter than the θ_e surfaces in a moist environment. It also shows that CI occurs where θ_e surfaces start to fold over. This usually occurs on the warmer side of the cross-section, while CSI tends to occur on the cooler side (Schultz and Schumacher 1999). It is also advantageous to recognize the region of WSS, as described by Schumacher (2001), where M_g and θ_e are nearly parallel, this typically occurs on the cooler side of the cross-section (the region labeled 'NS' on Fig. 2.2). Emanuel (1985); Sanders and Bosart (1985b); Sanders (1986b), and Nicosia and Grumm (1999) found that WSS can enhance the DTC by contracting and strengthening the updraft (see Fig. 2.4). The presence of WSS enhances the updraft and narrow banded structures within clouds and precipitation. The stronger ascent is usually aligned parallel to the isotherms and leads to stronger low-level convergence and upper-level divergence that is perpendicular to the isotherms. The convergence leads to increased frontogenesis and a stronger temperature gradient which reduces the EPV. This feedback process (Fig. 2.5) can show how frontogenesis may become strong close to a region of highly negative EPV (Nicosia and Grumm 1999).

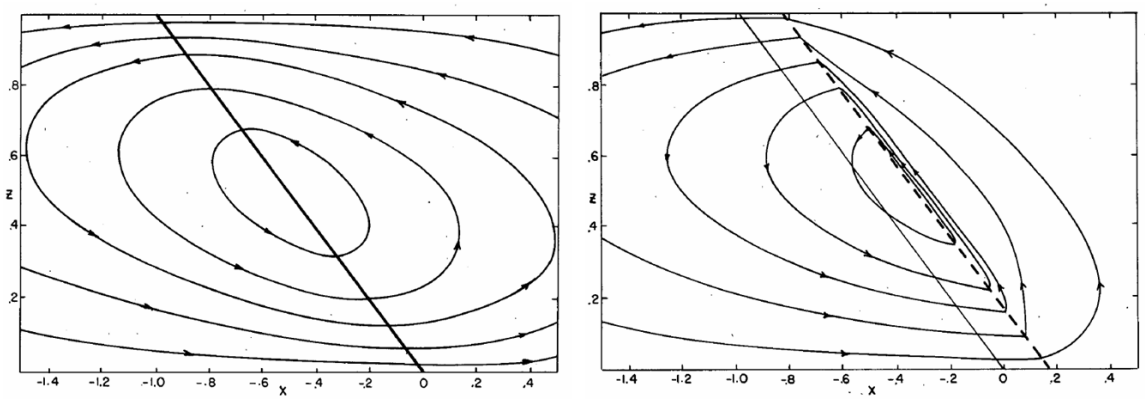

Figure 2.4: The standard cross-front circulation (streamlines) in physical space (left) and with geostrophic potential vorticity reduced (right) on the warm side of the frontogenesis axis (solid line). From Emanuel (1985, p. 1068).

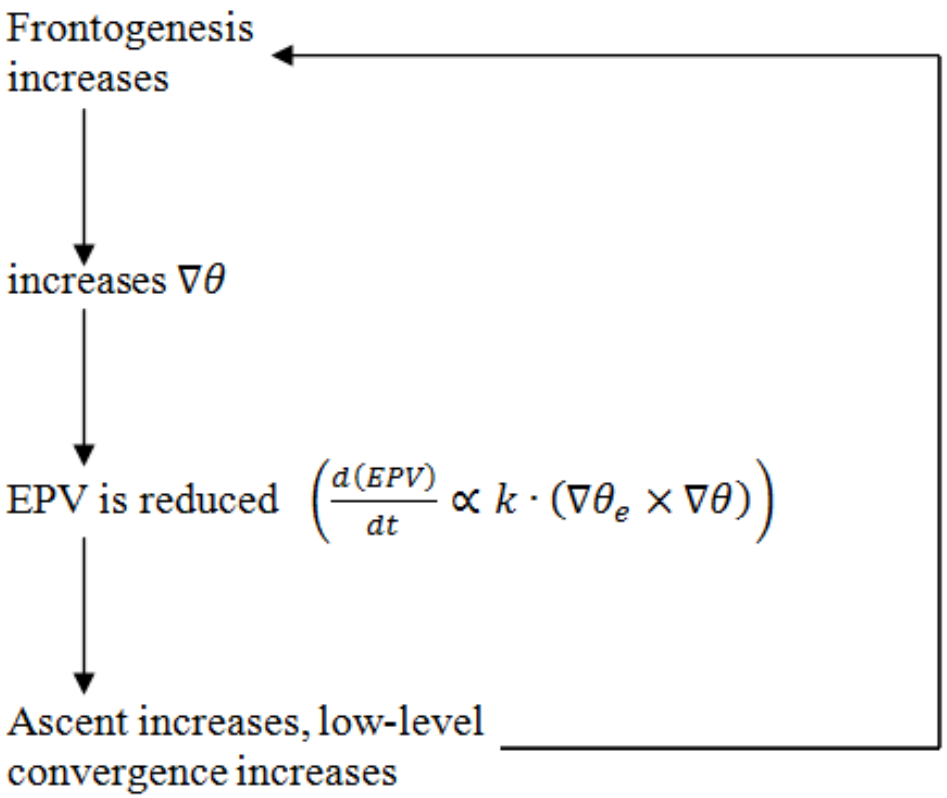

Figure 2.5: Schematic depicting a positive feedback mechanism between frontogenesis and the reduction of equivalent potential vorticity. From Nicosia and Grumm (1999, p. 364).

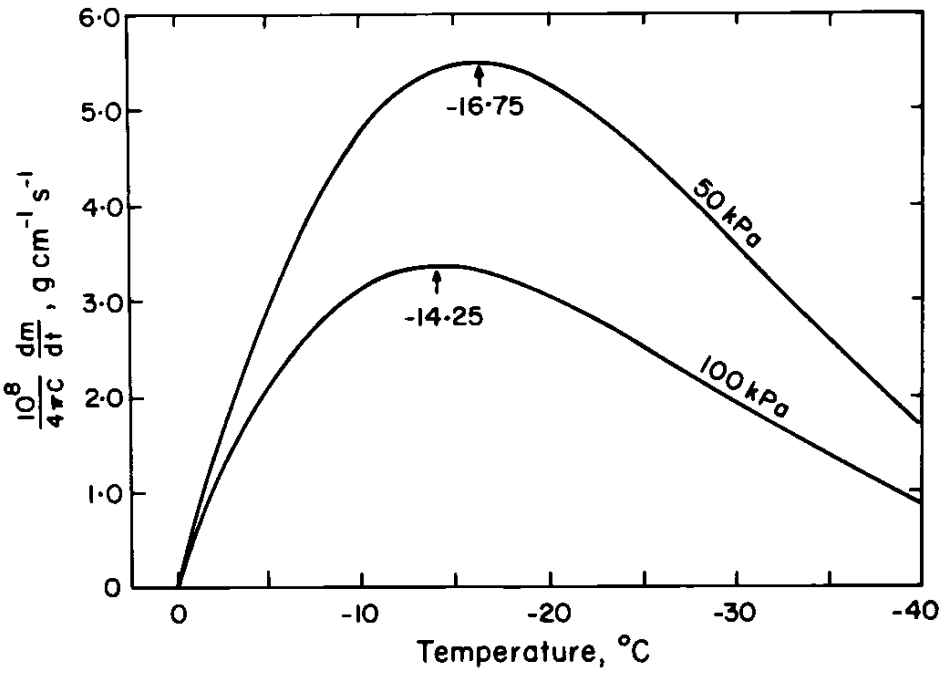

Figure 2.6: Normalized ice crystal growth rate (g cm^{-1} s^{-1}) as a function of temperature (°C), for 50 kPa and 100 kPa. From Rogers and Yau (1989, p. 161).

2.1.3 Microphysics

The efficiency ingredient in the Wetzel and Martin (2001) IM focuses on two parameters: in-cloud temperatures and growth rate. In-cloud temperatures are diagnosed to assess the likelihood of ice nucleation and to anticipate enhanced precipitation rates associated with rapid snowflake growth. Cold-cloud precipitation processes occur when ice crystals form through heterogeneous nucleation, homogeneous nucleation, or by deposition on an existing ice crystal (Rogers and Yau 1989). Based on statistical studies (e.g., Mossop [1970]), Baumgardt (2000) developed the guideline that -12°C to -14°C is the warm threshold for the presence of ice in a cloud and that -10°C is the operational cutoff (i.e., if this temperature is not reached somewhere in the cloud it is likely that the cloud contains only supercooled water droplets).

The second efficiency parameter is ice crystal growth rate, where ice crystals grow by deposition, accretion, or aggregation. Physically, deposition is the change of state from water vapor directly to ice crystals in a heteorogeneous environment. Often referred to as the Bergeron-Findeisen process, deposition occurs when ice crystals grow at the expense of liquid droplets in an environment that is subsaturated with respect to water but supersaturated with respect to ice (Rogers and Yau 1989). The change of state takes place because the saturation vapor pressure over ice is less than that over water. The vapor pressure gradient that develops permits the transfer of water vapor from liquid droplets (higher pressure) to ice crystals (lower pressure). The process occurs until the air surrounding the liquid droplets is sub-saturated, at which time the liquid droplets will evaporate and make additional water vapor available for ice crystal growth. Unless there is a physical process that can replenish the liquid droplets, in time they will evaporate and the cloud will be glaciated. Figure 2.6 shows that the growth of an ice crystal by diffusion is maximized between -12°C and -18°C. Research has shown that dendritic ice crystals are common in this temperature range (Power et al. 1964), which is also known as the dendritic growth zone.

Accretion occurs after an ice crystal grows initially by diffusion to a sufficient size, begins to fall, and overtakes supercooled liquid droplets. Much like the collision and coalescence growth process for warm clouds, accretion is most efficient when the collector crystal falls rapidly. Growth by accretion is most common in the lower portion of the cloud where there is a greater concentration of supercooled liquid droplets. Temperature also plays a role in the growth of ice crystals through aggregation, the joining of multiple snowflakes to form a larger snowflake. Growth by aggregation is most efficient by dendrites and generally occurs when snowflakes have grown large enough to begin to fall and when

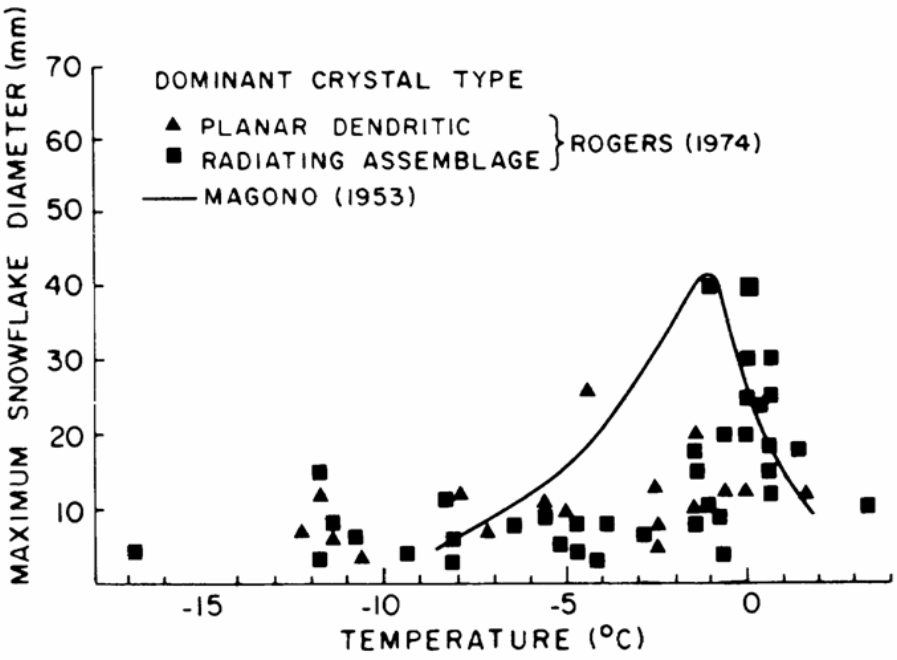

Figure 2.7: Maximum observed snowflake diameters (mm) as a function of air temperature (°C) for two types of snowflake composition. From Pruppacher and Klett (1997, p. 501); after Rogers (1974).

temperatures are warmer than -10°C. Figure 2.7 shows that this process is most efficient at and just below 0°C. Roebber et al. (2003) states that aggregation decreases the density of snowfall, which in turn will increase snowfall amounts.

The role of microphysical concepts can be applied in operational meteorology and heavy snow forecasting. In a climatological study of 75 heavy snowfall episodes in the United States, Auer and White (1982) used representative upper-air soundings from the left-front quadrant of each storm. They found that heavy snow episodes are distinguished by the collocation of the maximum vertical velocity and the -12°C to -18°C temperature regime in the presence of saturated conditions. This allows for the maximum amount and continued delivery of saturated air parcels to maximize crystal growth rates and the Bergeron-Findeisen process. With operational forecast model data and the

BUFKIT forecast analysis tool kit, Waldstreicher (2001) reinforced the importance of microphysics in an operational setting. This study analyzed 64 winter storm warning and 75 winter storm advisory snow events in the northeastern United States and their correlation with the cross-hair signature (maximum vertical velocity within the dendritic growth zone). Waldstreicher (2001) found that 76% of the warning criteria events had the cross-hair signature while only 9% of the advisory events had the signature present. This emphasizes the early research by Auer and White (1982) and the importance of continued transport of moist air into the dendritic growth zone.

2.2 Winter Weather Conceptual Models

2.2.1 Mid-Latitude Cyclone Conceptual Models

Despite early attempts at outlining the structure of extratropical cyclones (ETCs) by FitzRoy and Shaw, synopticians did not begin to accept the model of a cyclone until the work of Bjerknes at the end of World War I (Petterssen 1956). Using a dense network of surface observations from Norway, Sweden, and Denmark, Bjerknes (1919) was able to present a model of an ETC (Fig. 2.8). The planar view in the conceptual model illustrates the airflow around the cyclone, cold and warm frontal positions, precipitation (shaded area), and the warm sector. Bjerknes (1919) was clear that rainfall extended in a broad zone along the cool side of the warm front and in a narrow one along the cool side of the cold front. He also noted that precipitation was irregularly dispersed in the warm sector and that the distribution of upward vertical motions were collocated with clouds and precipitation. The cross section through the warm sector (lower portion of Fig. 2.8) shows both frontal zones, cloud types, and air streams. Along

the warm front, cloud types range from nimbus/nimbostratus with the precipitation shield to cirrus at upper levels due to the gradual sloped ascent originating in the warm sector while focused ascent of the warm sector air along the cold front forms a squall line. The cross section north of the low center (upper portion of Fig. 2.8) depicts a warm pool of air above a cold dome and precipitation shield.

The CM of an ETC presented by Bjerknes (1919) is taken to represent the typical structure of the cyclone at a given time. Bjerknes and Solberg (1923) found that ETCs change regularly during their life cycles and pass through a series of stages (Fig. 2.9). Initially, the cyclone formation takes place on a boundary of two oppositely directed currents of different temperature (Fig. 2.9a). Along the low-level baroclinic zone, a small-amplitude disturbance forms and warm air bulges toward the cold side (Fig. 2.9b). The newly formed cyclone is found at the apex of this warm tongue and propagates eastward along the baroclinic zone. As the disturbance moves eastward, the warm sector increases in size and cold air is advected to the south by the northwesterly current behind of the low-level center (Fig. 2.9c). This stage of the cyclone evolution is most similar to the ETC CM discussed in Fig. 2.8. As the amplitude of the disturbance continues to increase, the warm tongue narrows (Fig. 2.9d) and the cold air from behind the cyclone reaches the cold air along the warm front (Fig. 2.9e). At this point, the low-level cyclone is detached from warm sector air and the cyclone is said to be occluded. The cyclone continues to decay and propagate further from the warm sector until a cold vortex remains (Fig. 2.9f-h).

The evolution of an ETC cyclone was also illustrated by Bjerknes and Solberg (1923) through vertical cross sections (Fig. 2.10). From the inception of the cyclone through the occlusion stage (Fig. 2.9c-e and Fig. 2.10c-e), warm air is

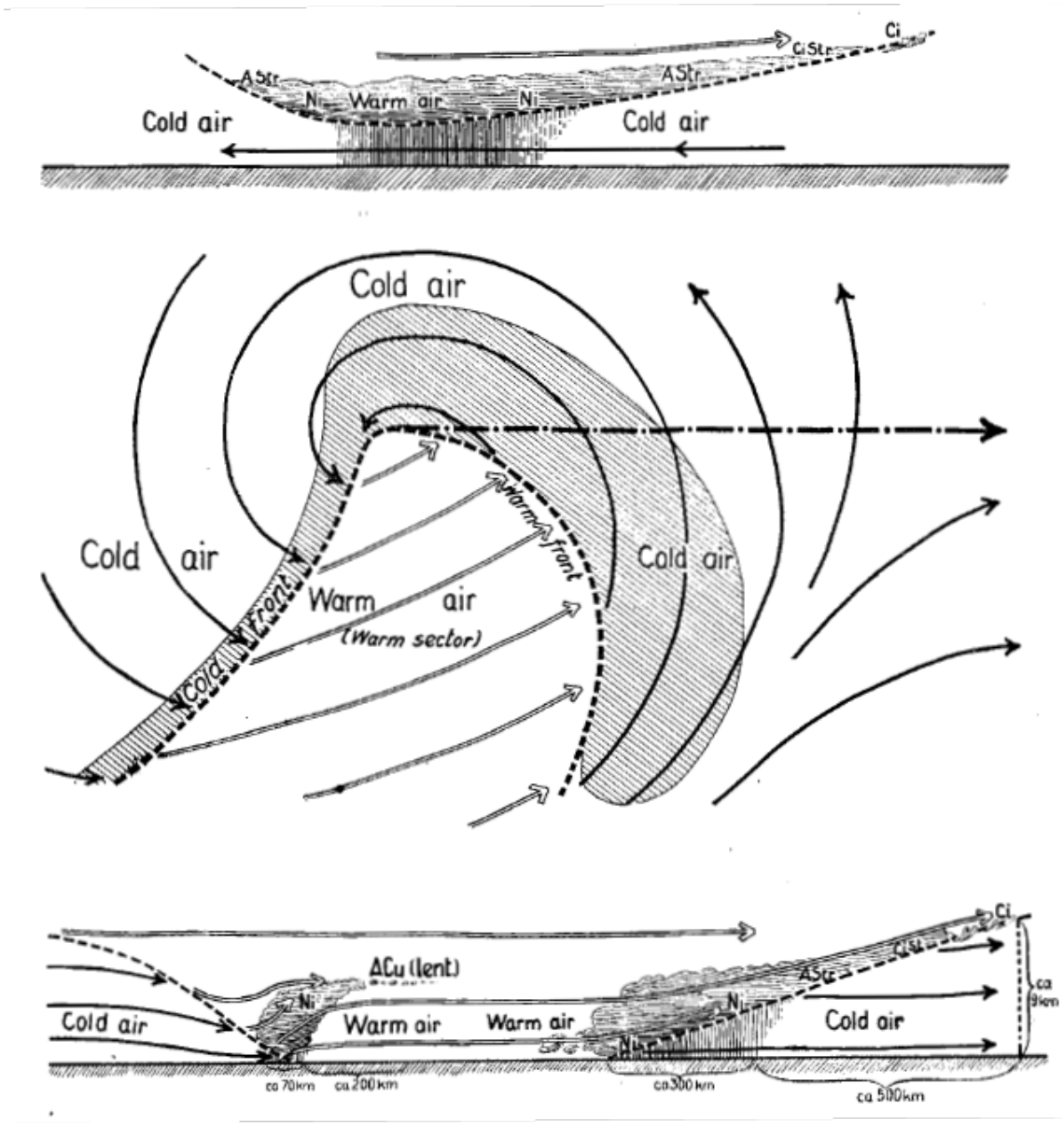

Figure 2.8: Cloudiness and precipitation in moving cyclones. From Bjerknes and Solberg (1923, p. 3).

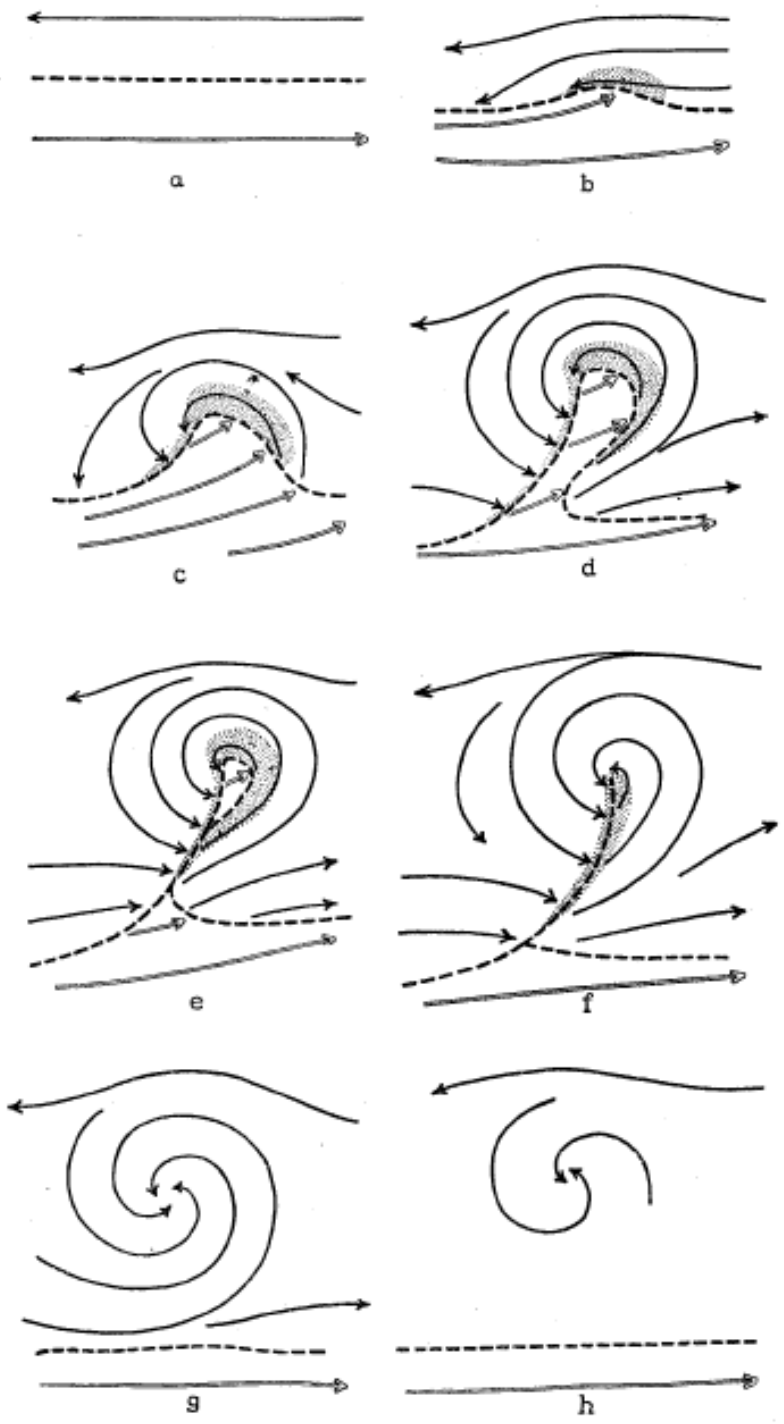

Figure 2.9: The life cycles of cyclones. From Bjerknes and Solberg (1923, p. 5).

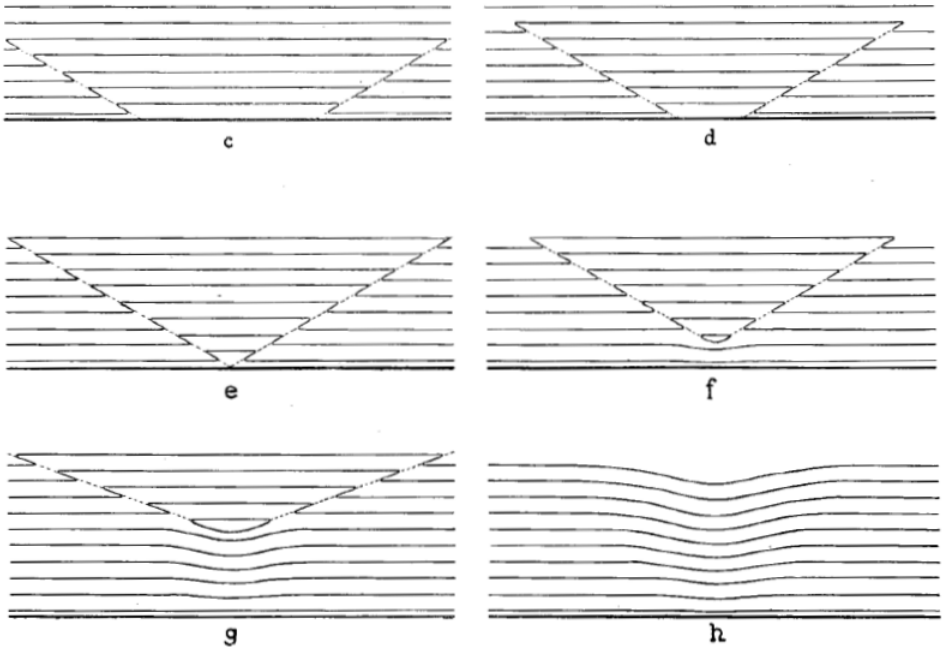

Figure 2.10: Vertical cross sections through cyclones in different stages of development. Solid contours are isotherms and dotted contours are discontinuities. The cross sections were cut to the south of the surface cyclone from west (left) to east (right). From Bjerknes and Solberg (1923, p. 6).

being lifted by the cold and warm fronts. Bjerknes and Solberg (1923) state that this process transforms some of the system's potential energy into kinetic energy. As a result, winds increase and the disturbance deepens due to releasing baroclinic instability supplied by the warm sector. Once the two wedges of cold air meet near the surface (Fig. 2.10e-f), warm sector air is still present aloft and will continue to be lifted until the warm air cools adiabatically to the temperature of the surrounding air at the same level (Bjerknes and Solberg 1923). While slight modifications of the surface cyclone model by Bjerknes (1919) and Bjerknes and Solberg (1923) occurred as upper-air observations became available, the basic features and processes suggested remained relatively unchanged through the mid-1950s (Petterssen 1956).

Even though the work of Bjerknes and Solberg (1923) documented the life

cycle of an ETC, there was little explanation as to why the low-level cyclone developed and strengthened. Bjerknes and Holmboe (1944) began to explain the ETC's low-level development by using the surface pressure tendency equation:

$$\left(\frac{\partial p}{\partial t}\right)_0 \approx -\int_0^\infty \mathrm{div}_H(\rho v)\delta\phi \tag{2.7}$$

where the local rate of change of the surface pressure is proportional to the inverse of the vertically integrated divergence through the column of the atmosphere. Figure 2.11 summarizes how pressure changes occur in eastward moving cyclones. Bjerknes and Holmboe (1944) found that pressure falls ahead of the low-level cyclone occur because upper-level divergence is strong enough to overcompensate for the convergence of air into the cyclone's center. The convergence/divergence couplet found in the vertical is present because there is a phase difference between the upper-level trough and the low-level cyclone center (Fig. 2.11). Palmen and Newton (1969) expanded on low-level cyclone development by using the "self-development" process that was first introduced by Sutcliffe and Forsdyke (1950). Figure 2.12 illustrates the development of an upper-level baroclinic wave and the related low-level ETC. When a low-level cyclone develops, low-level temperature advection increases and in turn distorts the thickness field and upper-level flow pattern (Fig. 2.12, top left to top right). As the upper-level wave's amplitude increases, it contributes to increasing vorticity advection above the low-level cyclone which implies an increase in upper-level divergence and low-level convergence into the strengthening cyclone. This positive feedback process will continue until the wave takes on barotropic characteristics when the upper-level wave becomes aligned with the low-level cyclone as in Fig. 2.12 (bottom).

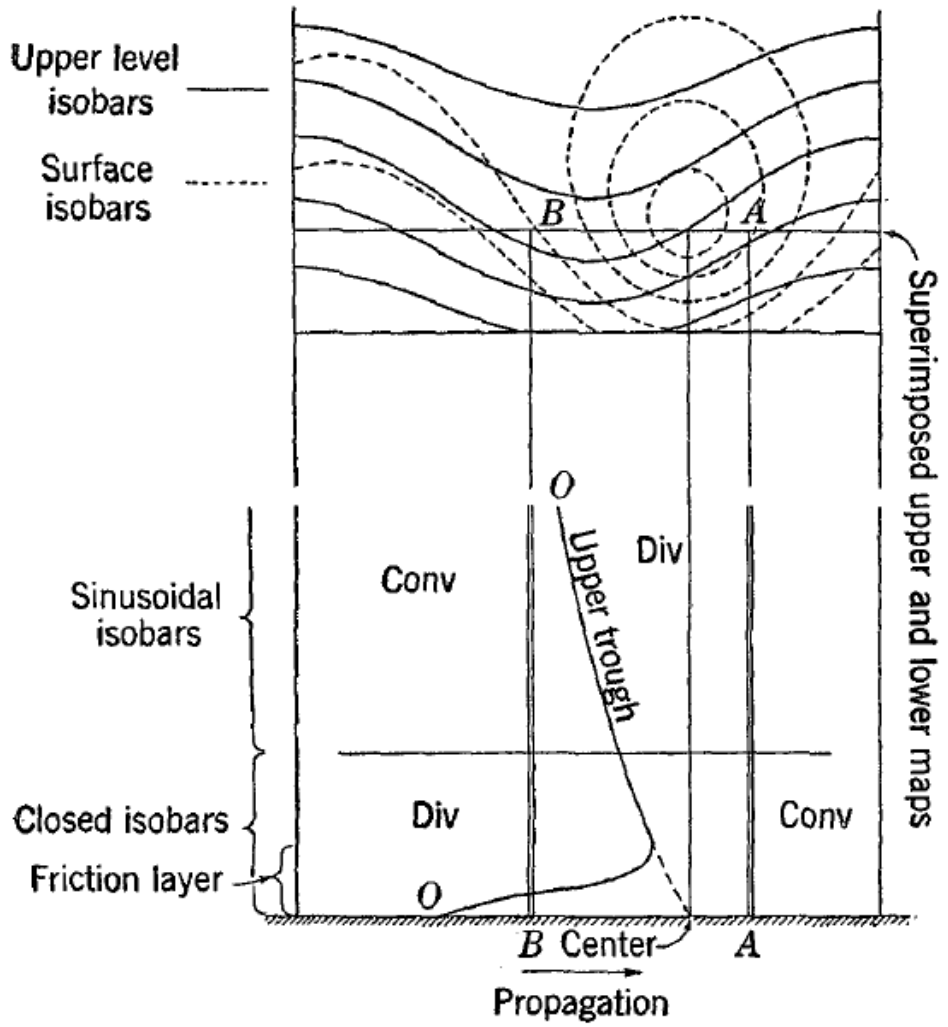

Figure 2.11: Closed concentric isobars (dashed) in low levels coexistent with sinusoidal isobars (solid) in the upper levels. From Bjerknes and Holmboe (1944, p. 21).

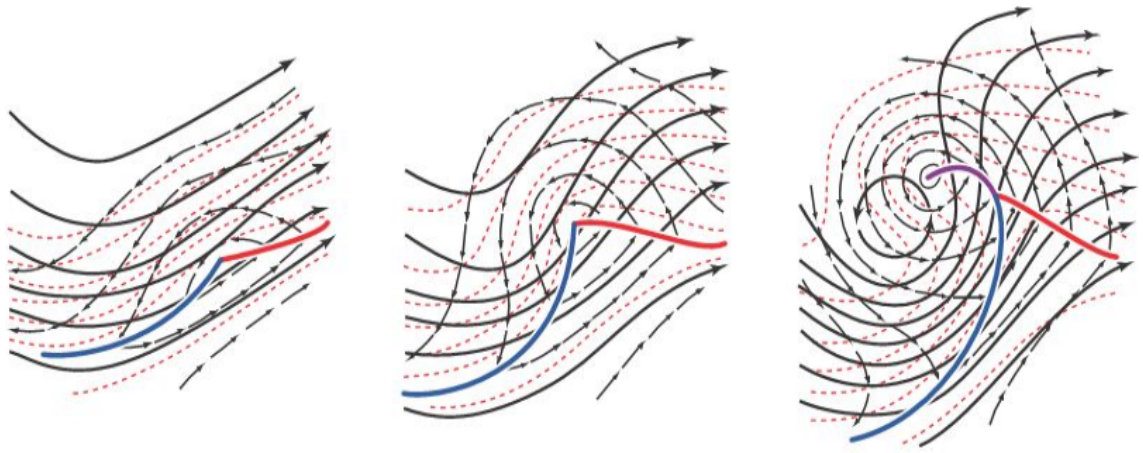

Figure 2.12: Schematic 500-hPa contours (heavy solid lines), 1000-hPa contours (thin lines), and 1000-500 hPa thickness contours (dashed), illustrating the "self-development" process during growth cycle of a cyclone. From Palmen and Newton (1969, p. 326).

2.2.2 Air Streams and Conveyor Belt Conceptual Models

Air streams were first introduced in the early 20th century by Shaw and others (e.g., Shaw and Lempfert 1906; Shaw 1911; Bjerknes 1919; Bjerknes and Solberg 1923). However, there were limitations to these early CMs (e.g., Fig 2.13) as they did not depict airflow very far above the surface (Schultz 2001). As upper-air observations became more available, detailed analysis was provided of air streams (e.g., Namias 1939; Palmen and Newton 1951; Danielsen 1964). Conveyor belts (i.e., air streams), first termed by Harrold (1973), are an ensemble of air parcels that originate from a common source region and layer that are tracked over synoptic-scale time periods (on the order of 24–36 h) and best viewed on isentropic surfaces (Moore et al. 2005). Three major conveyor belts have been identified with cyclogenesis: warm conveyor belt (WCB; Harrold 1973), cold conveyor belt (CCB; Carlson 1980), and dry conveyor belt (DCB; Danielsen 1964).

The WCB (shown in Fig. 2.14 top) is a well-defined ribbon of high-θ_w air

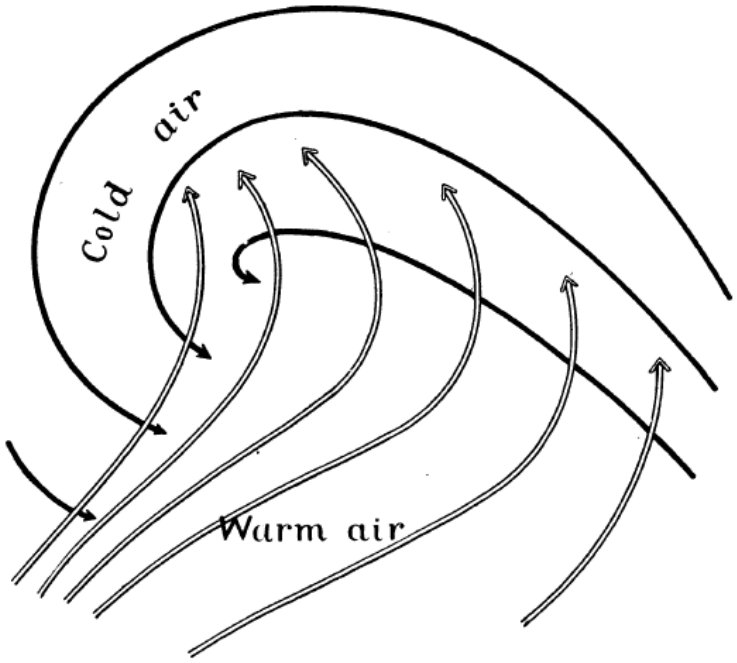

Figure 2.13: Cyclone motion in lower strata. From Bjerknes (1919, p. 7).

between 100 km and 1000 km wide and a few km deep that gradually ascends northward from the warm sector until eventually ascending over the warm front. With respect to an ETC, the WCB is oriented parallel to the surface cold front and accompanied by a low-level jet until until it turns anticyclonically north of the warm front (Harrold 1973). In the warm sector, convective precipitation is common with the WCB while stratiform precipitation occurs north of the warm front. In addition to the anticyclonic turning branch of the WCB, there is also a cyclonic turning branch associated with ETCs (shown in Fig. 2.14 middle and bottom).

The cyclonic branch of the WCB is also known as the trough of warm air aloft (TROWAL). First identified in occluding cyclones by Crocker et al. (1947) as warm sector air aloft that extends several hundred miles to the northwest of the surface junction of the warm and cold fronts (Figs. 2.14 bottom and 2.15).

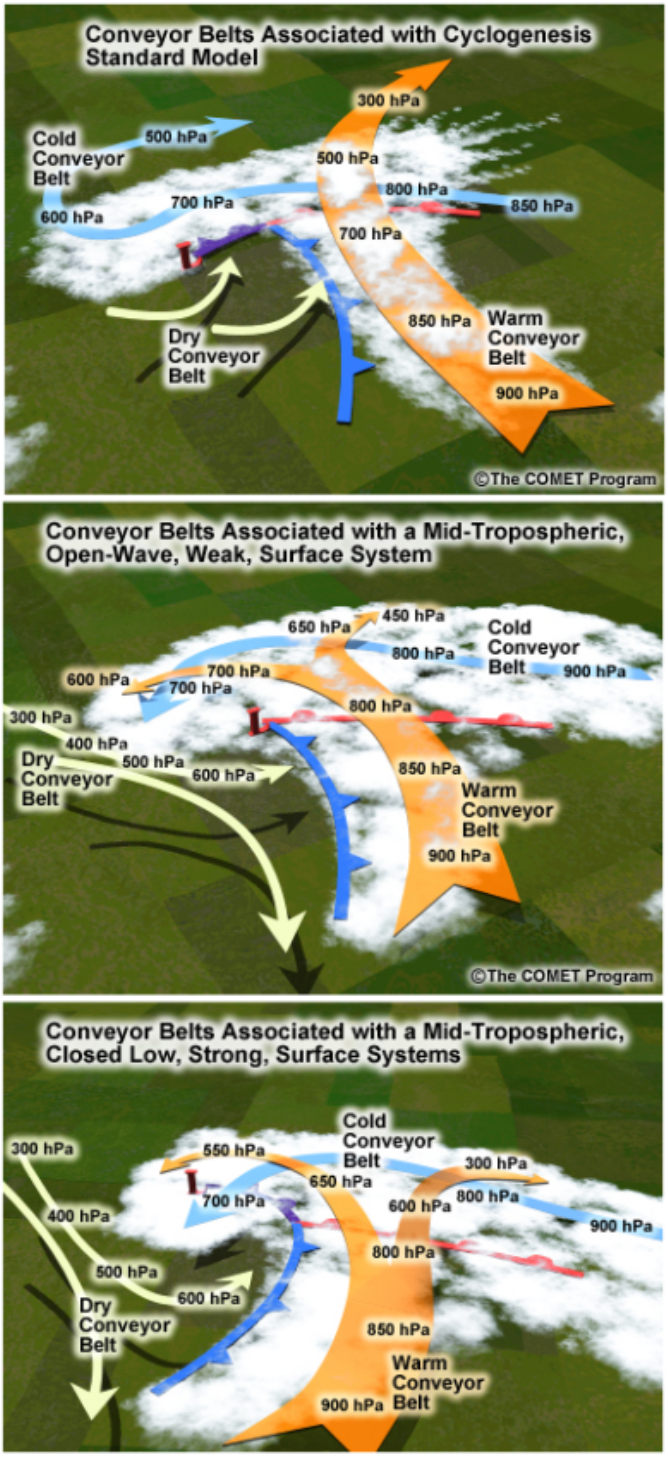

Figure 2.14: Conceptual model of conveyor belts associated with cyclogenesis. Standard model (top), open mid-tropospheric wave with weak surface system model (middle), and closed mid-tropospheric wave with strong surface system model (bottom). From COMET (2002).

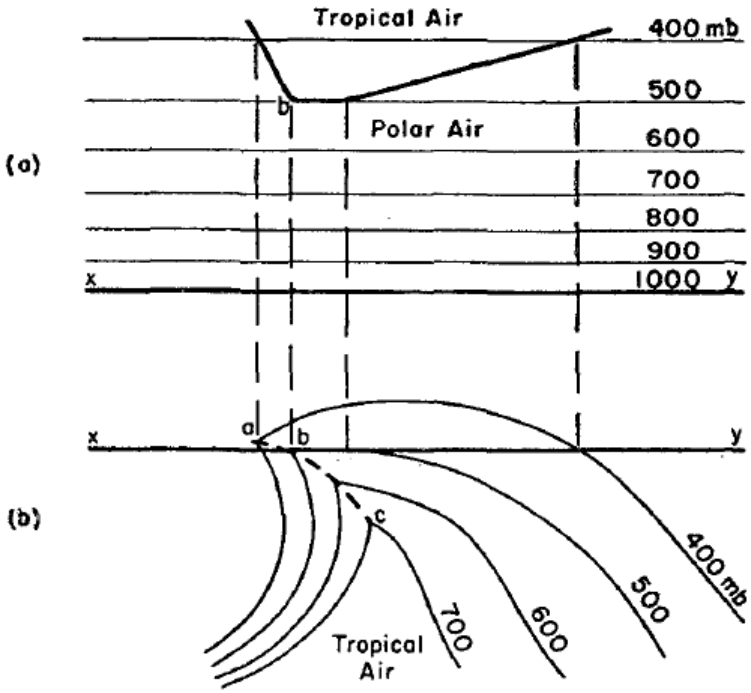

Figure 2.15: An upper cold front portrayed by (a) a vertical cross section; (b) a frontal contour chart. Line abc would be the line marked as an upper cold front on a surface map. From Crocker et al. (1947, p. 97).

However, Penner (1955) showed that a TROWAL is not always associated with an occluding surface system (Figs. 2.14 middle and 2.16). Martin (1999) reintroduced the concept of the TROWAL and defined it as the three dimensional sloping intersection of the upper cold frontal portion of the warm occlusion with the warm frontal zone (Fig. 2.17). He identified that the TROWAL is often responsible for the production of precipitation to the north and west of the occluded surface cyclone center and its position had a greater correlation to cloud and precipitation features than the occluded front.

The CCB (shown in Fig. 2.14 top) originates from high pressure to the east northeast of the surface cyclone that approaches from the east and rises under the WCB before turning anticyclonically to the northwest of the cyclone center (Carlson 1980). However, early CMs (e.g., Figs. 2.13), and more recently Schultz

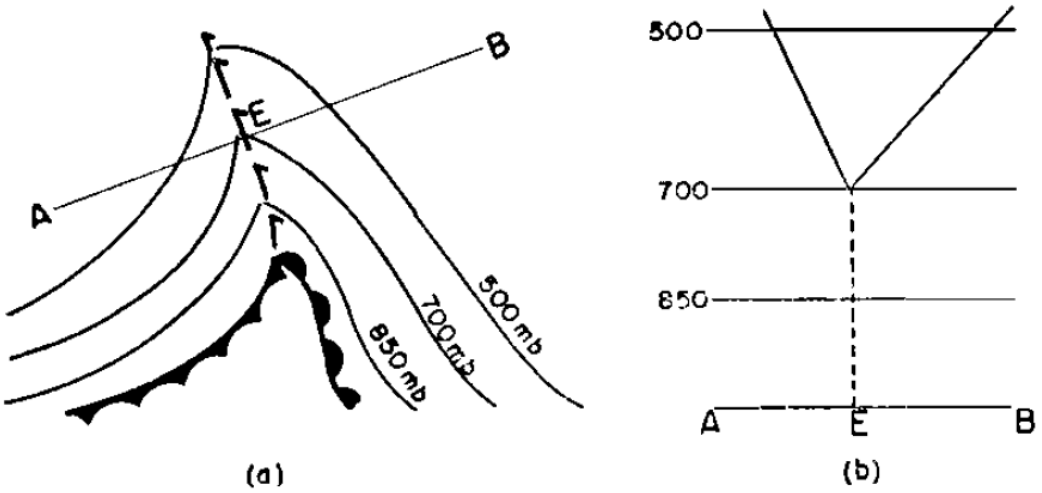

Figure 2.16: Polar-front model of a cyclone wave. (a) Frontal contours, (b) vertical cross section. From Penner (1955, p. 90).

(2001), showed the CCB turning cyclonically around the surface cyclone (Fig. 2.14 middle and bottom). Schultz (2001) found that both the cyclonic and anticyclonic paths of the CCB existed and the anticyclonic path of the CCB represented a transition between the WCB and the cyclonic path of the CCB. While often associated with a low-level jet, the CCB is less defined than the WCB and can contain a large range of θ_w values due to its location within the warm frontal zone (Browning 1999). Precipitation generated north of the warm front and within the WCB must fall through the CCB. Therefore, the temperature and humidity of the CCB can play an important role in controlling the type and amount of precipitation reaching the surface north of the warm front (Schultz 2001).

The DCB (shown in Figs. 2.14 and 2.18) is characterized by low-θ_w air that descends from the upper troposphere and lower stratosphere on the western side of the surface cyclone (Danielsen 1964). As the DCB descends through the midlevel trough, it fans out into a southern branch that continues to descend and

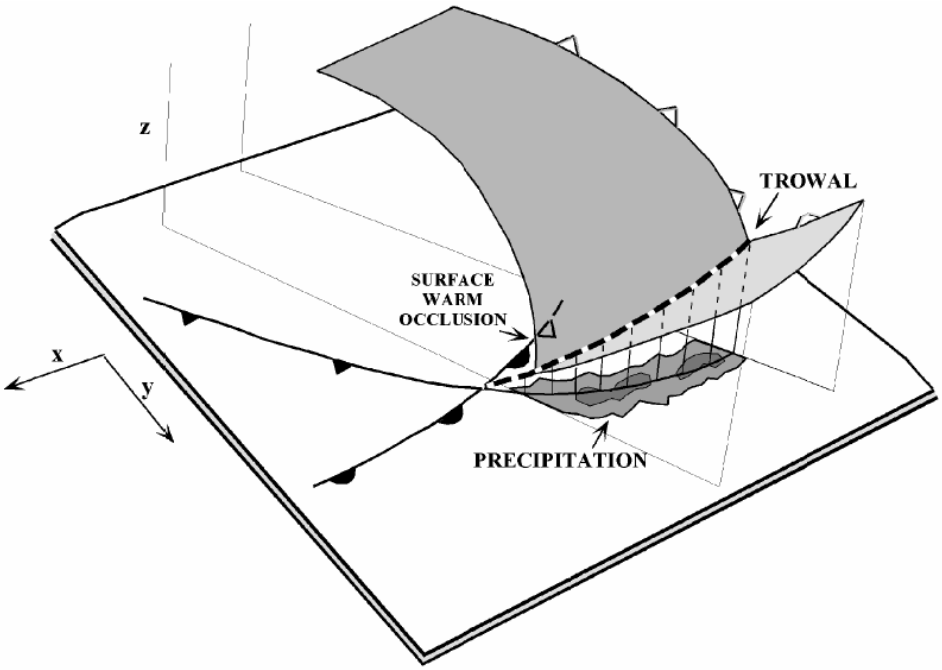

Figure 2.17: Schematic illustration of the TROWAL conceptual model. The lightly shaded surface represents the warm edge of the cold frontal baroclinic zone. The darker shaded surface represents the warm edge of the warm frontal baroclinic zone. The thick dashed line (marked TROWAL) represents the three-dimensional sloping intersection between the cold and warm frontal zones characteristic of warm occlusions. Schematic precipitation band is indicated as are the positions of the surface warm, cold, and occluded fronts. From Martin (1999, p. 72).

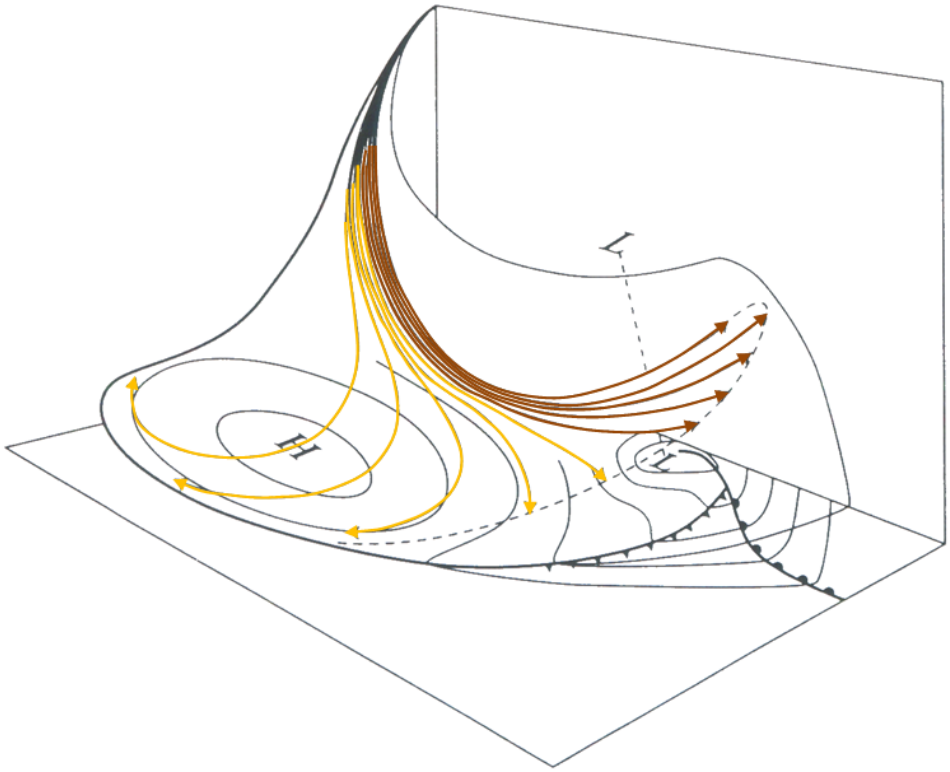

Figure 2.18: Trajectories of air originating from a small region near the tropopause, drawn within a curved isentropic surface. The surface is shown sloping from a position near a tropopause fold down to the ground. Trajectories come close to the ground in the left part of the diagram but not in the right-hand part, where they overrun the surface fronts. From Browning (1999, p. 273); after Danielsen (1964).

a northern branch that begins to ascend. The southern branch (yellow arrows in Fig. 2.18) descends into the lower troposphere and turns anticyclonically. The portion near the cyclone's trailing cold front is often the descending limb of an ana-cold frontal circulation while the portion to the east and south of the surface high pressure flows rearward ahead of the warm front associated with the next cyclone in the sequence and may develop into its CCB (Browning 1999). The northern branch (brown arrows in Fig. 2.18) begins to ascend and becomes the dry intrusion or dry slot of the ETC (Danielsen 1964). In this region, stability is reduced as the dry, stable stratospheric air flows above moist air below.

2.2.3 Heavy Snow Conceptual Models

As the structure and evolution of ETCs became better understood, studies evolved that examined these systems and their associated weather on a regional scale. Miller (1946) found that two types of cyclogenesis are common in the Atlantic coastal region of the United States during the cool season: type A and type B. Type-A cyclones usually form along the polar front of a cold outbreak when a cold anticyclone covers most of the United States east of the Rocky Mountains (Fig. 2.19). These cyclones develop over the ocean and move in a northeasterly direction affecting only areas along the immediate coast. In contrast, type-B cyclones originate to the southeast of an existing cyclone's warm front near the coast line. Type-B ETCs also move northeastward but their proximity to the coast line allows sensible weather to affect a larger portion of the East Coast. In the central United States, cool-season (February–April) ETCs that developed in the lee of the Colorado Rockies and moved east northeast through the Great Lakes were studied by Fawcett and Saylor (1965). Their results revealed that these ETCs were associated with synoptic-scale dynamics, baroclinicity, and high-impact weather (i.e., blizzards and severe weather). Figure 2.20 shows the composite ETC at peak intensity 24 h after development. In this stage of the cyclones' development, heavy snow and severe thunderstorms were observed 84% and 81% of the time respectively.

These synoptic-scale analyses of ETCs and their sensible weather led to a series of studies that focused on improving operational forecasting of heavy snowfall east of the Rocky Mountains. Goree and Younkin (1966) found that heavy snow east of the Rocky Mountains tends to be located 2.5° latitude (278 km) to the left of the 500-hPa absolute vorticity maximum and the surface

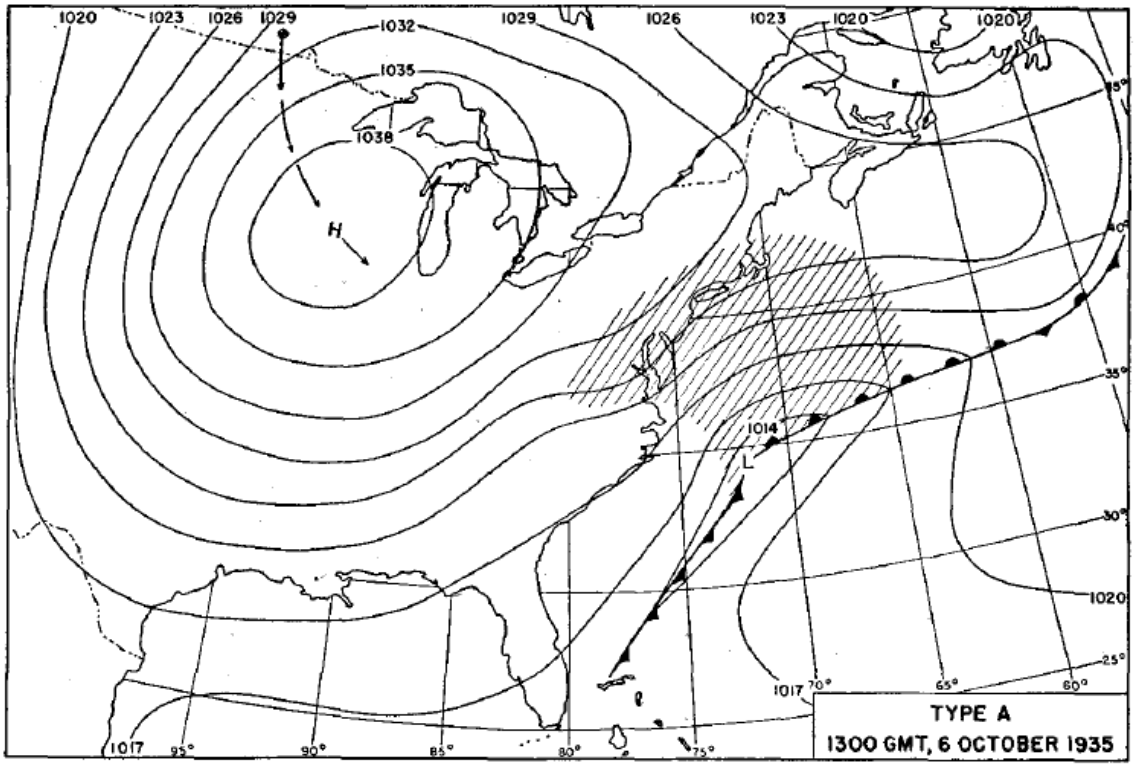

Figure 2.19: Example of type-A cyclone at time of origin. Fronts are indicated by conventional symbols; areas where precipitation is occurring are covered by hatching, whether the precipitation is intermittent or continuous; the lines are isobars labeled in millibars; and 24-hourly positions of pressure centers are marked by a cross enclosed in a circle. From Miller (1946, p. 32).

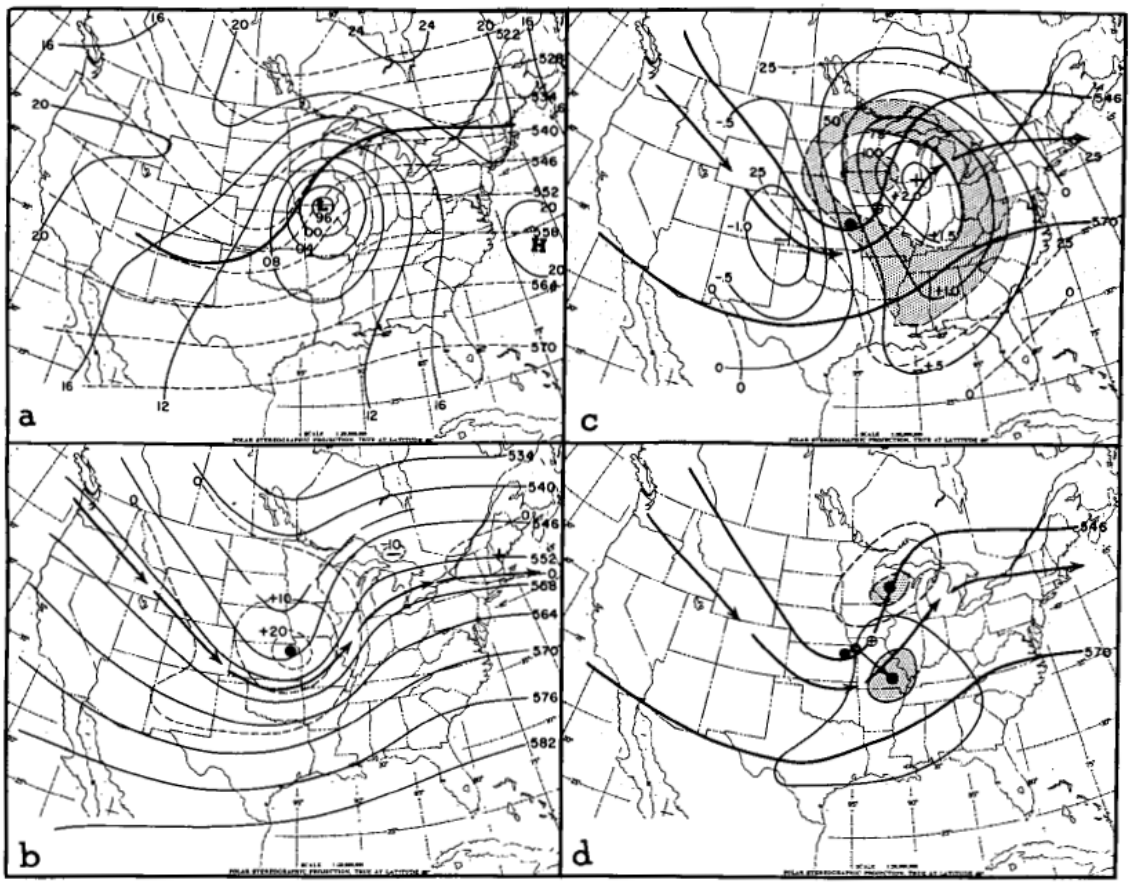

Figure 2.20: Mean charts for 24 h after cyclogenesis. (a) Mean surface pressure in hPa. (solid), mean 1000-500 hPa thickness in decameters (dashed) and equal probability line of frozen vs. nonfrozen precipitation (heavy solid). (b) Mean 500-hPa height in decameters (solid) and relative vorticity in relative units (dashed). Arrowed line shows mean position of jet stream. (c) Mean 600-hPa omega in μb s^{-1} (solid) and percentage frequency of cases in which predominant synoptic weather was precipitation (dashed). Solid circle indicates position of 500-hPa vorticity maximum and crossed circle, position of surface cyclone. (d) Outer dashed line encircles all observed areas of heavy snow in past 12 h; inner dashed line and stippling show mean size and position of heavy snow in past 12 h. Both curves given in relation to mean position of surface low (crossed circle). Solid curves give a similar analysis of occurrences of severe thunderstorm activity. From Fawcett and Saylor (1965, p. 362).

low-pressure center tracks. They also found that most cases have warm air advection and positive vorticity advection over a region, which contributes to the upward vertical motion for major snowstorms. Browne and Younkin (1970) expanded on this approach by developing a study at 850 hPa. They found that the 850-hPa lows deepened significantly during the period of heavy snowfall, and that the -5°C isotherm nearly bisects the heavy snowfall area. In addition, the highest probability for heavy snowfall occurs approximately 90 nm (167 km) to the left of the 850-hPa low track. Spiegler and Fisher (1971) examined the relationship between the 850-hPa cyclone and heavy snowfall along the East Coast. They found that there is a high frequency (i.e., >60%) of the precipitation type being entirely snow approximately 75 to 200 miles to the left of the 850-hPa low track and the rain-snow line was usually 50-75 miles on either side of the track. Browne and Younkin (1970) and Spiegler and Fisher (1971) each found few occurrences where heavy snowfall occurred without a discernible 850-hPa low (one case and <5% of cases, respectively). These results show the importance of 850-hPa low in forecasting the location and the occurrence of heavy snowfall associated with ETCs.

In one of the first long-term climatologies of synoptic-scale conditions associated with snowstorms along the East Coast, Kocin and Uccellini (1990) examined the 20 most crippling from 1955 to 1985. Much like Miller (1946), Kocin and Uccellini (1990) found two distinct surface low-pressure paths with East Coast snowstorms: secondary redevelopment and primary or no redevelopment. Secondary redevelopment occurred over the southeastern United States after an initial surface low-pressure center moved towards the Appalachian Mountains from the Ohio Valley (Fig. 2.21). Primary redevelopment occurred with systems that passed south of the Appalachian Mountains and tracked northeastward

along the East Coast where they exhibited a center jump. In total, 17 of the 20 cases clearly showed secondary or primary redevelopment (Kocin and Uccellini 1990). At midlevels, the 20 snowstorms were associated with the three geopotential height patterns shown in Fig. 2.22. Even though there were three distinct midlevel height patterns, the half-wavelength (the distance from the trough to the downstream ridge) decreased during cyclogenesis in all 20 cases. This suggests that these snowstorms were associated with an increase in vorticity advection and upper-level divergence (Kocin and Uccellini 1990). An examination of the upper-level flow patterns with eight East Coast snowstorms by Uccellini and Kocin (1987) revealed the collocation of a direct circulation within a confluent entrance region of an upper-level jet streak over the northeastern United States or southeastern Canada and an indirect circulation within the exit region of an upper-level jet streak entering the base of the upstream trough (Fig. 2.23). Their results showed that the jet streak interaction was responsible for enhancing the low-level jet, which in turn increased differential moisture and temperature advections necessary for heavy snowfall along the East Coast.

During the end of the 20th century, case studies (e.g., Sanders and Bosart 1985b; Moore and Blakley 1988), increased numerical weather prediction resolution, and improved atmospheric observations showed the importance in understanding the mesoscale processes that are associated with heavy snowfall. Using the National Centers for Environmental Predictions Meso Eta Model and Weather Surveillance Radar-1988 Doppler (WSR-88D) base reflectivity data, Nicosia and Grumm (1999) investigated heavy banded snowfall associated with three strong northeastern United States snowstorms. Their CM showed the juxtaposition of frontogenesis and negative EPV in the deformation zone, north

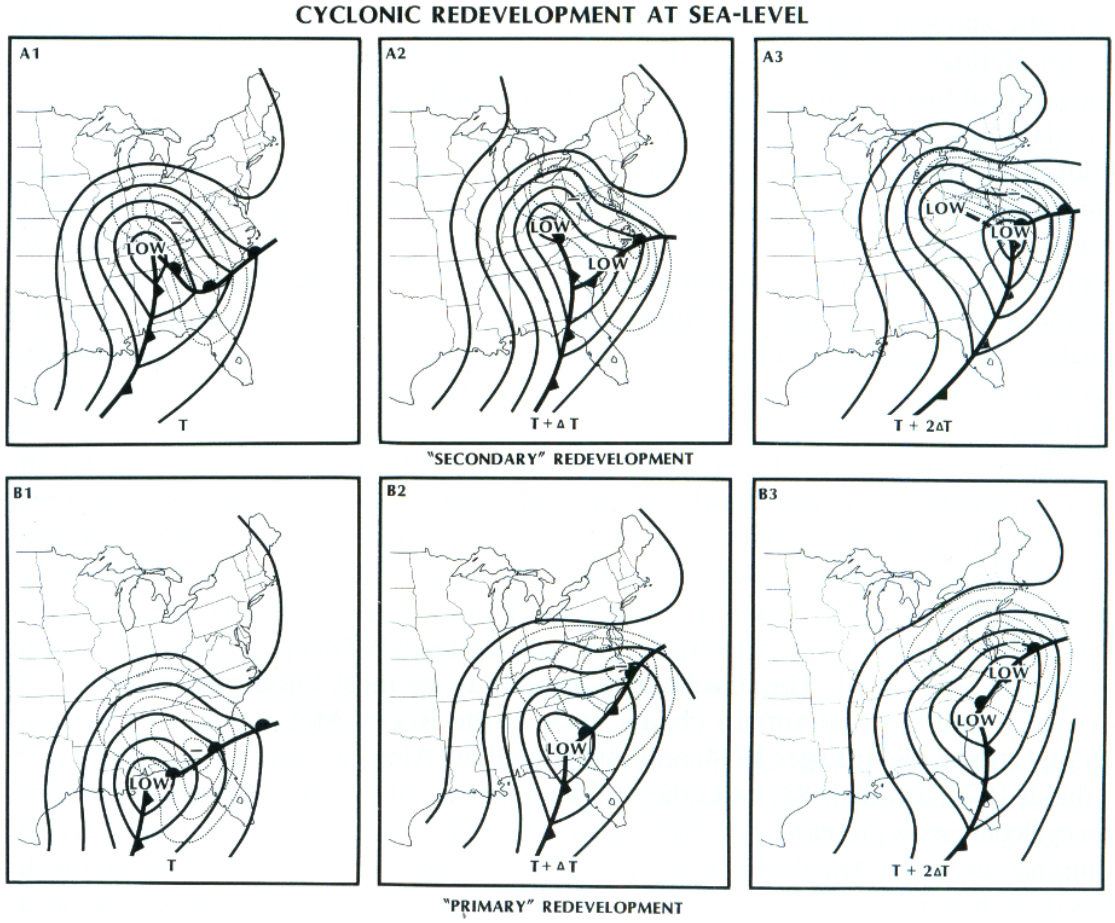

Figure 2.21: Schematic representation of cyclogenesis along the East Coast, including (a) "secondary" redevelopment as an Ohio Valley system fills and (b) "primary" redevelopment or center jump as a Gulf of Mexico system moves northeastward. Solid lines are isobars and thin dotted lines represent isallobars for regions of greatest pressure falls. From Kocin and Uccellini (1990, p. 25).

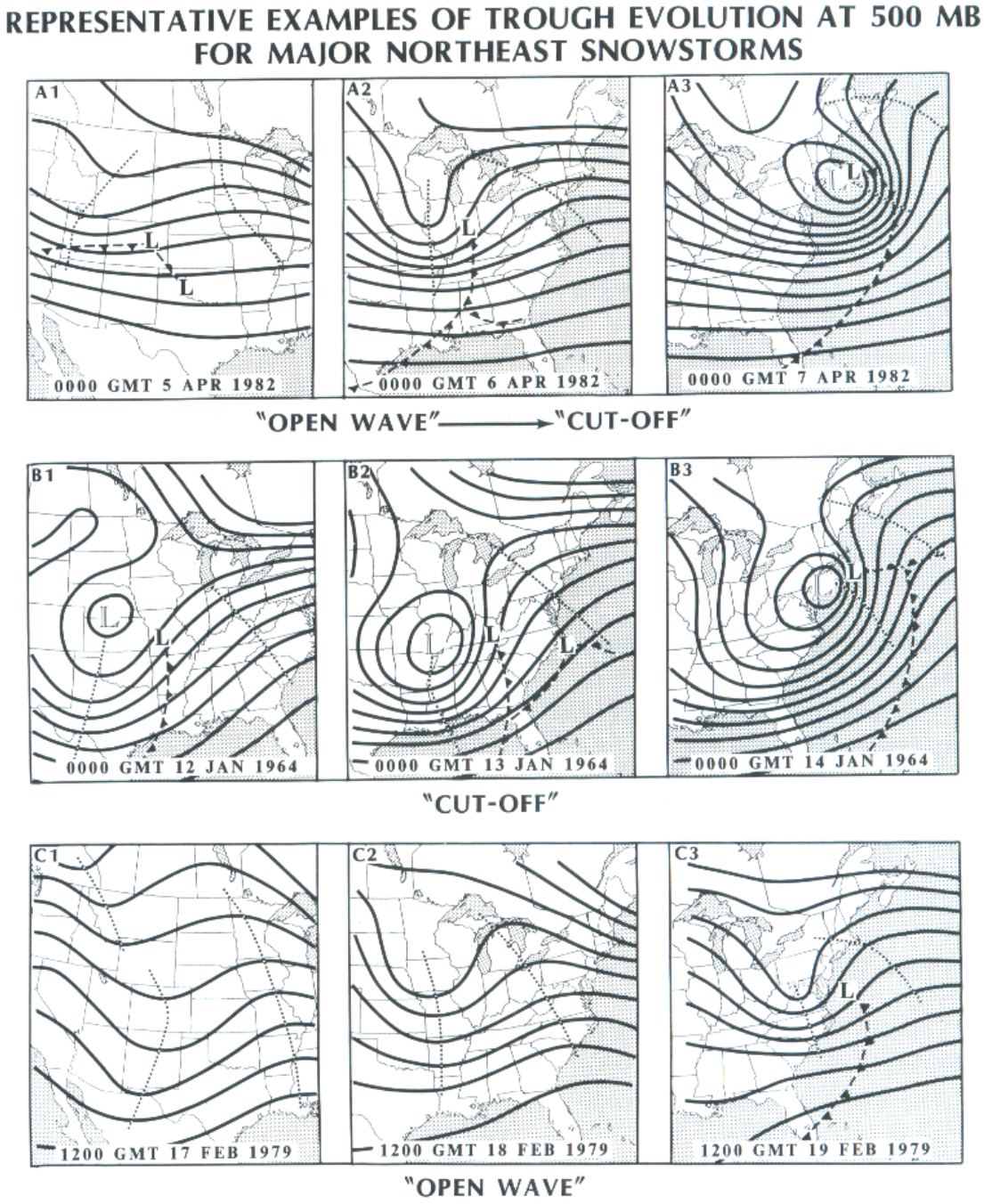

Figure 2.22: Representative examples of trough evolution for major Northeast snowstorms. (A1, A2, A3) Illustration of "open wave" to "cutoff" system, by storm of 5-7 April 1982. (B1, B2, B3) Illustration of cutoff system prior to and during cyclogenesis by storm of 12-14 January 1964. (C1, C2, C3) Illustration of an open wave trough that did not evolve into a cutoff system by storm of 17-19 February 1979. Solid lines are 500-hPa geopotential height contours. Dotted lines indicate trough and ridge axes. Positions of sea-level cyclone and surface fronts are also shown. From Kocin and Uccellini (1990, p. 47).

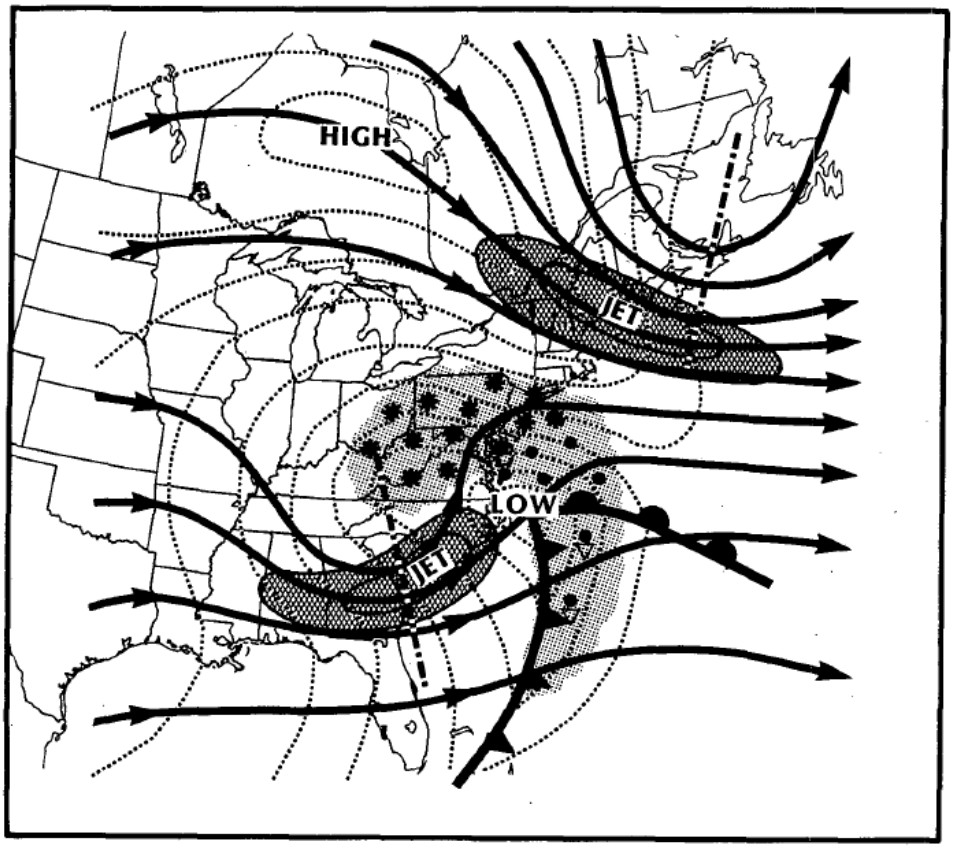

Figure 2.23: Schematic of surface cold and warm fronts, high and low pressure centers, sea level isobars (dotted), precipitation (shading–asterisks represent snowfall; dots represent rain), upper-level flow (arrows), upper-level trough axes (dot-dashed), and jet streaks (cross-hatched shading) associated with a "typical" heavy snow event along the East Coast. From Uccellini and Kocin (1987, p. 290).

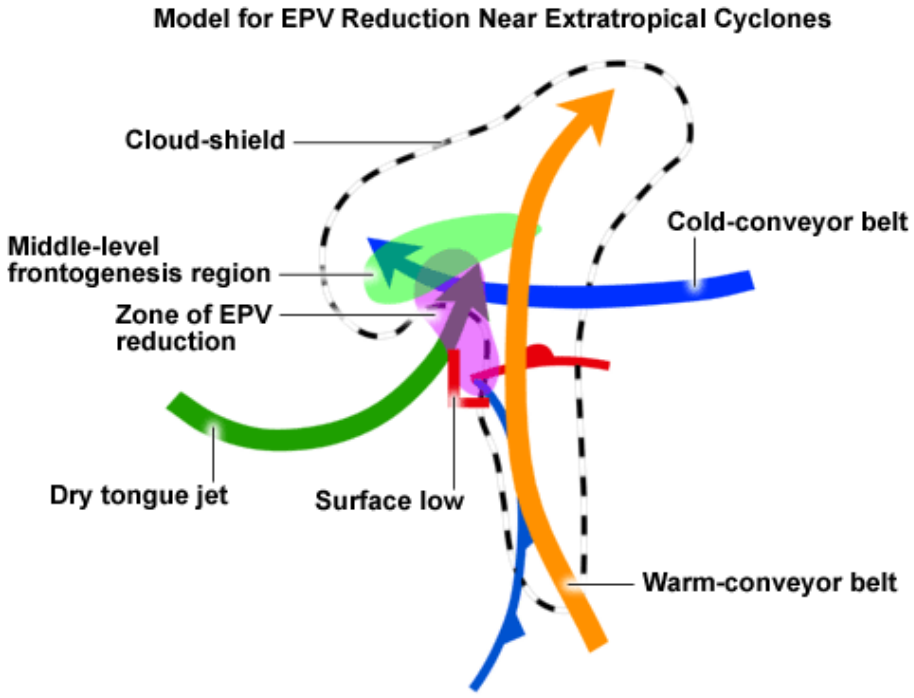

Figure 2.24: Conceptual model depicting the frontogenesis region and zone of equivalent potential vorticity reduction within the context of the major components of a developing extratropical cyclone. From COMET (2002); after Nicosia and Grumm (1999).

of the developing midlevel cyclone (Fig. 2.24). The reduced stability and negative EPV developed south of a midlevel frontogenesis maximum when the DCB overlaid a moist easterly low-level jet streak associated with the CCB. This interaction provided an increase in ascent and the initiation of the positive feedback mechanism in Fig. 2.5.

Banacos (2003) used three operational cases in different regions of the United States to support his CMs of the synoptic-scale settings associated with heavy banded precipitation. He used horizontal deformation to locate mesoscale banding potential because of its first-order contribution to the two-dimensional frontogenesis function shown in Eq. 2.2. Shown in Fig. 2.25, the Banacos (2003) CMs are characterized by horizontal deformation in the 850-500-hPa layer. In the top of Fig. 2.25, the deformation develops as the cyclone deepens from an open

wave to a closed low. In the northwest portion of the cyclone, diffluent flow develops where the CCB splits into its cyclonic and anticyclonic branches. In the bottom of Fig. 2.25, the deformation occurs due to confluent flow associated with a positively-tilted 700-hPa trough that is parallel to the baroclinic zone. This category is often associated with a weak surface cyclone and is common in the Great Plains in the cool season. A case study of a long, narrow band of heavy snowfall in the central United States by Moore et al. (2005) supported the modest surface cyclone CM of Banacos (2003). In this case, a strong area of deformation contributed to a midlevel frontogenesis maximum for an extended period of time where the heavy snowfall was observed. The Moore et al. (2005) CM (Fig. 2.26) for this case is also similar to the CM in Fig. 2.24 by Nicosia and Grumm (1999). An area of negative EPV extends from the south of the surface cyclone northward to the nose of the DCB. Here, a region of CSI (in the absence of convective instability) is present to the southeast of a midlevel frontogenesis maximum that developed as the WCB or TROWAL turned cyclonically.

It was stated in Banacos (2003) that the observational cases presented demonstrated the need for comprehensive climatologies of banded precipitation. A lack of climatological studies was most likely due a lack of observational data on the scale of banded precipitation structures (Novak et al. 2004). However, with the implementation of the WSR-88D network, climatologies such as Novak et al. (2004) and Novak et al. (2010) have taken place. In Novak et al. (2004), a climatology of cold-season banded events in the northeast United States was used to compare the frontal environments associated with banded and nonbanded events. Their results showed that during a five-year period from 1996–2001, 75 events exhibited banded structures with single-banded events in the northwest portion of the surface cyclone being the most common. The

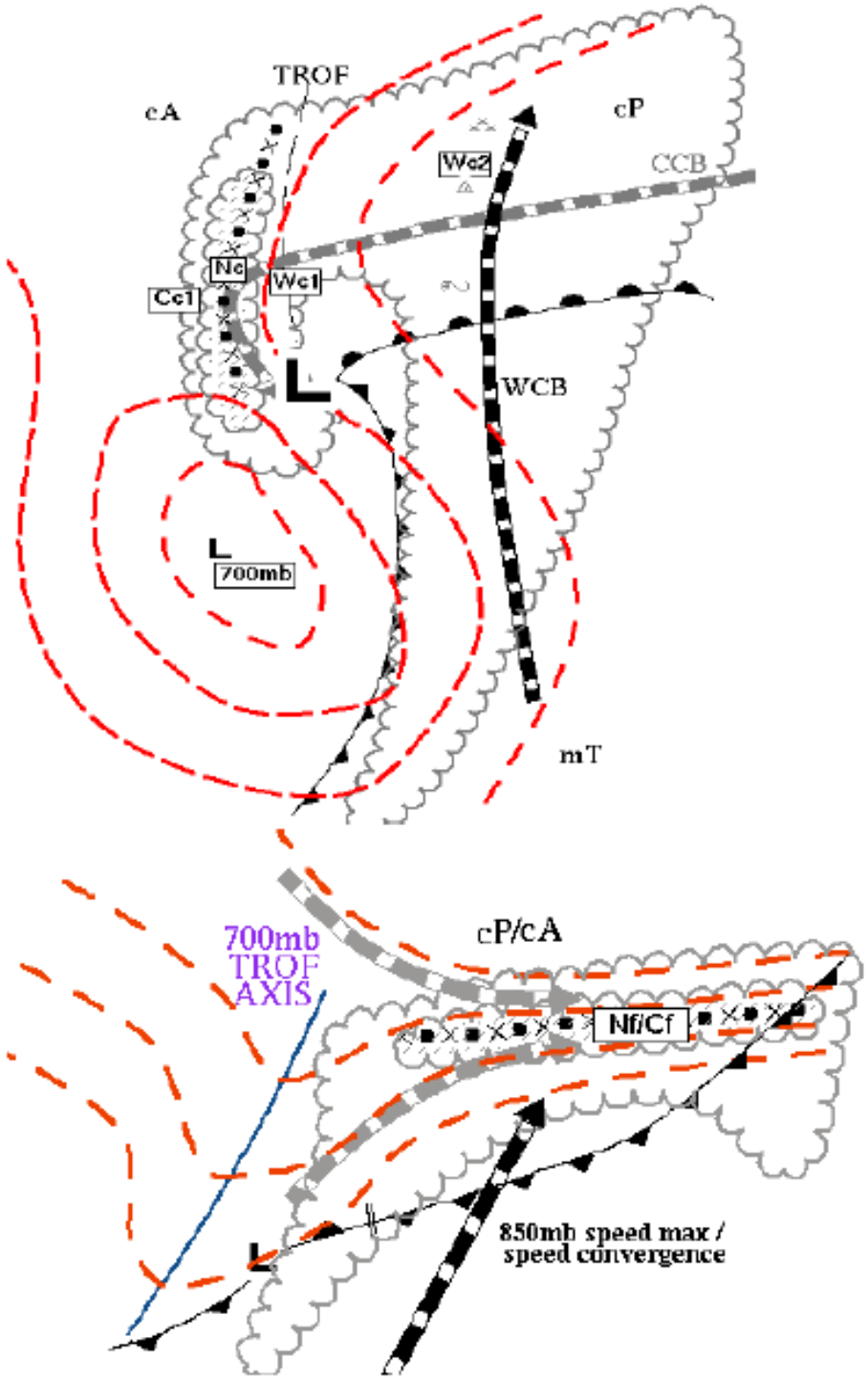

Figure 2.25: Schematic deformation zones (denoted by axes of filled circles and Xs) occurring in association with (a) rapid cyclogenesis and (b) frontal zones with modest surface cyclone development. Dashed lines represent 700-hPa height. Scalloped region denotes high-level cloud pattern. From Banacos (2003, p. 1).

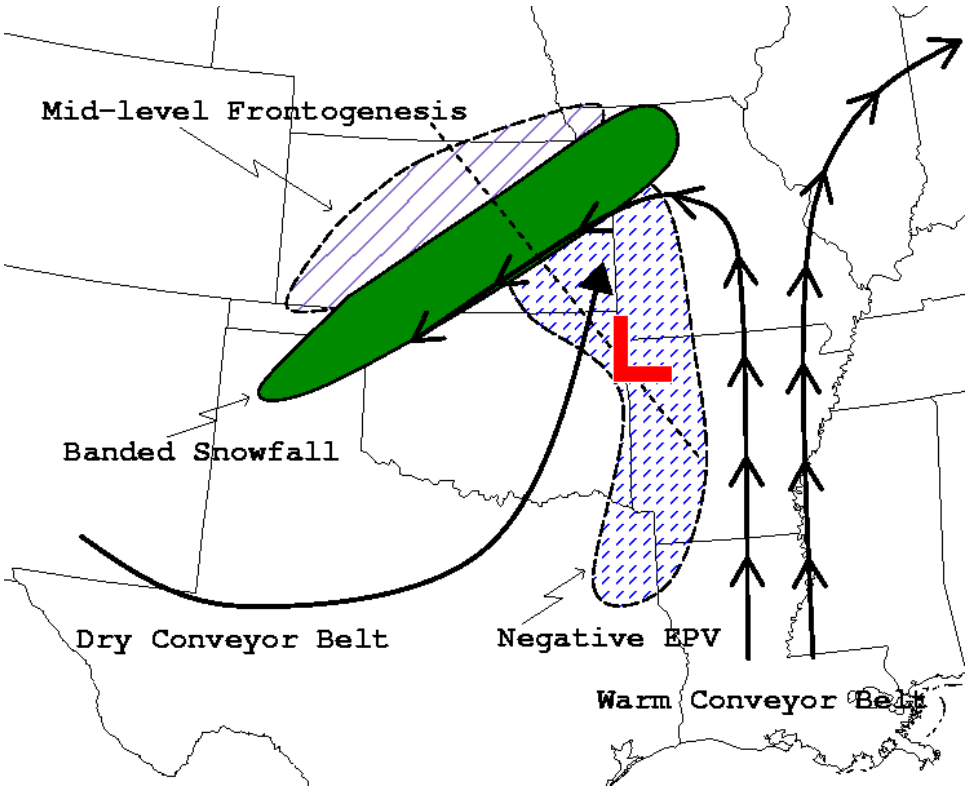

Figure 2.26: Conceptual model of those physical processes contributing to heavy banded snow formation for this case study. Plan view indicating the warm conveyor belt, dry slot, areas of negative EPV_g, midlevel frontogenesis, and banded snowfall. Here, L indicates position of surface low. From Moore et al. (2005, p. 48).

single-banded event CM by Novak et al. (2004) in Fig. 2.27 is consistent with previous CMs. Upper-level jet streak interaction is present with a midlevel closed circulation and surface cyclone under the area of upper-level divergence. In addition, a deformation zone exists to the northwest of the surface cyclone, which supports an area of frontogenesis. In the nonbanded CM, a weak surface low and open midlevel trough are located within the entrance region of an upper-level jet streak. Novak et al. (2004) states that the confluent flow ahead of the midlevel trough contributes to the deformation and frontogenesis.

More recently, a high-resolution observational climatology by Novak et al. (2010) sought to distinguish the characteristics between cyclones with closed midlevel circulations that develop snow bands and those that do not (null events). Their results suggest that even though there is a common band life cycle (formation, maturity, dissipation), there is not a common banded cyclone. The CM of the most common banded cyclone has a surface low that is beginning to occlude with a TROWAL extending to the northwest, a midlevel trough with speed shear that focuses the area of frontogenesis, and upper-level support by the exit region of a jet streak and potential vorticity (PV) anomaly hook that forces midlevel height falls (Fig. 2.28). The authors note that the difference between single-banded events and null events is the strength of the frontogenesis six hours prior to band formation, which is due to stronger temperature gradients observed in the single-banded events.

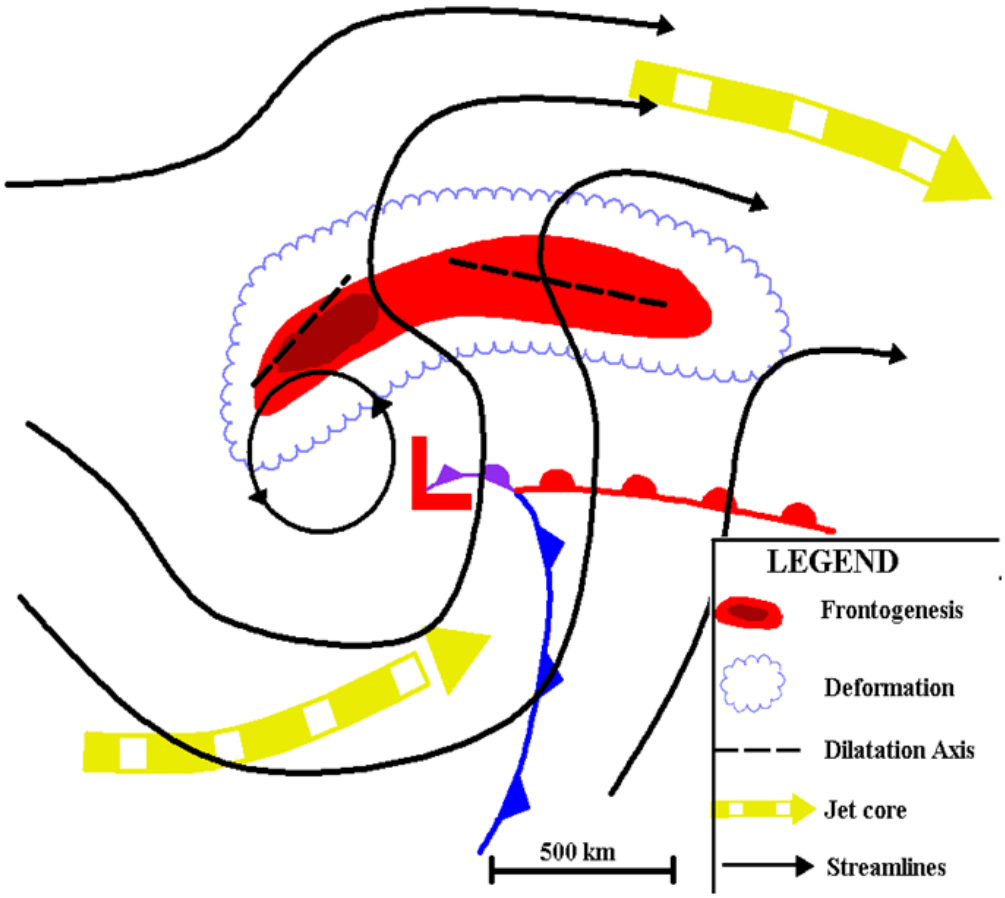

Figure 2.27: Conceptual model of the synoptic and mesoscale flow environment associated with a single-banded event and highlighting the key features. Features shown include midlevel frontogenesis (red shading), midlevel deformation zone (encompassed by scalloped blue line) and associated primary dilatation axes [dashed lines in (a)], midlevel streamlines (black lines), and upper-level jet cores (wide dashed arrows). From Novak et al. (2004, p. 1008).

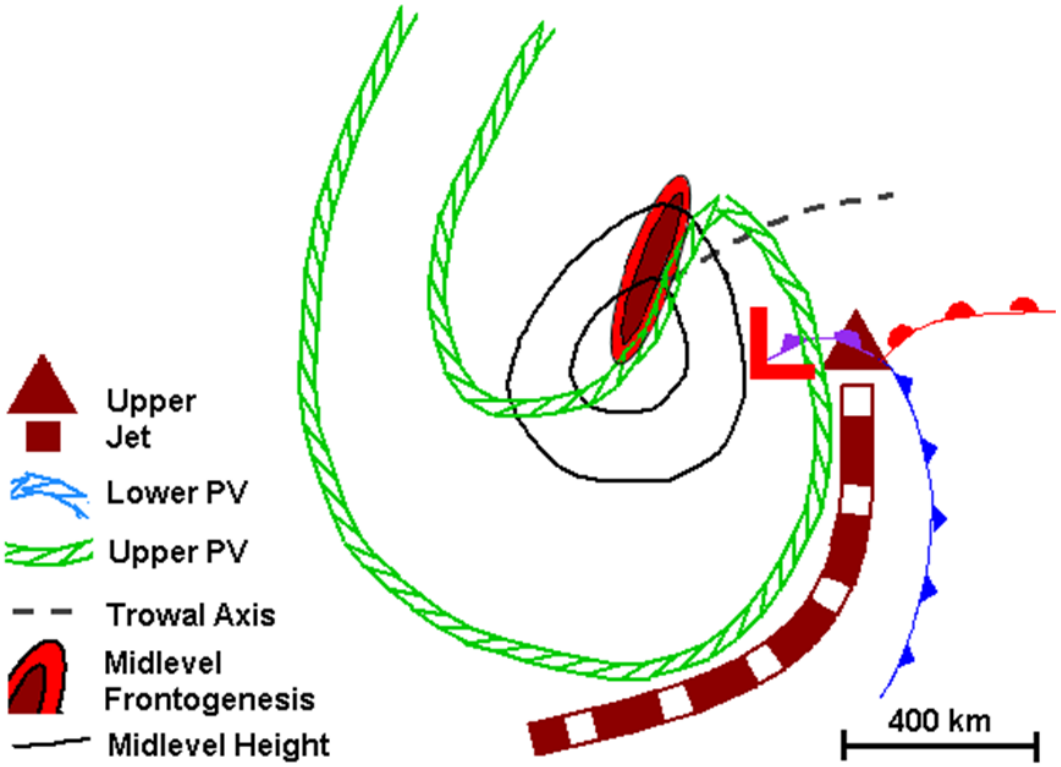

Figure 2.28: Conceptual model of the common cyclone at the time of initial band development highlighting the key features. Features shown include surface low position and fronts, midlevel height contours (black lines), midlevel frontogenesis (red shading), upper-level jet core (wide dashed arrow), upper-level potential vorticity anomaly (green cords), lower-level potential vorticity anomaly (blue cords), and TROWAL axis (dashed black). From Novak et al. (2010, p. 2371).

Chapter 3. Methodology

3.1 Creation of a Northeast Heavy Snow Conceptual Model

Previous research has shown the effectiveness of a composite analysis approach to diagnose the synoptic and mesoscale environments associated with certain weather events (e.g., Byrd 1989; Weisman et al. 2002; Moore et al. 2003; Novak et al. 2004, 2010). These composite results led to the development of CMs for cool-season banded precipitation, warm-season elevated thunderstorms, and heavy snowfall. A Northeast CM (hereafter NCM) that depicts the common heavy snow-producing cyclone that affects the northeastern United States was created through the composite approach. By using this approach with a long-term climatological dataset, it is hypothesized that the resulting NCM is a representative depiction of Northeast heavy snow CMs from previous research.

3.1.1 Case Selection

Snowfall data used in this research were obtained from the National Climatic Data Center (NCDC) Cooperative Summary of the Day (COOP) collection for the months of December, January, and February between 1 December 1980 and 29 February 2008. This dataset contains daily snowfall observations taken by trained weather observers once every 24 h, or (to a maximum of the sum of) four six-hourly observations to capture the greatest accumulation over the 24-h period. The daily COOP snowfall data and NCDC publications of the Daily Weather Maps' surface and 500-hPa charts were examined for temporal and spatial continuity between successive days to create organized snowfall events (i.e., >2 in.).

Northeast snowfall event anomalies were created by area averaging the snowfall events for the area bounded by the U.S.-Canadian border, the western Atlantic coastline, 83.0°W, and 35.5°N (Fig. 3.1). Similar to Kocin and Uccellini (2004), each snowfall event's area-average snowfall was weighted by the ratio of the area encompassed by greater than the 2-in. snowfall isohyet to the mean area of all snowfall events. This ensured that widespread events were ranked higher than regional events with similar area averages. Next, since precipitation data often exhibit a positive skew, a power transformation was applied to the snowfall events to create a nearly symmetric distribution (Wilks 2006). An individual snowfall event anomaly was computed by subtracting the mean of the transformed snowfall event values and dividing by the standard deviation:

$$z = \frac{x - \bar{x}}{s_x} = \frac{x'}{s_x} \tag{3.1}$$

A heavy Northeast snowfall event was defined as having an anomaly of at least +1.0 to be considered for inclusion into the NCM. Miller type-A, type-B, and continental storm tracks were associated with the anomalous snowfall events and the dominant track was chosen for inclusion in the NCM.

3.1.2 Composite Analysis Procedure

Similar to Moore et al. (2003), Novak et al. (2004), and Thomas and Martin (2007), the composite analysis was created using a system-relative approach. An advantage to system-relative composites is that the synoptic and mesoscale features are more likely to be representative of the individual cases because they are placed on a common grid at the same position when averaging. However, some features may still lose definition due to case-to-case variability with respect

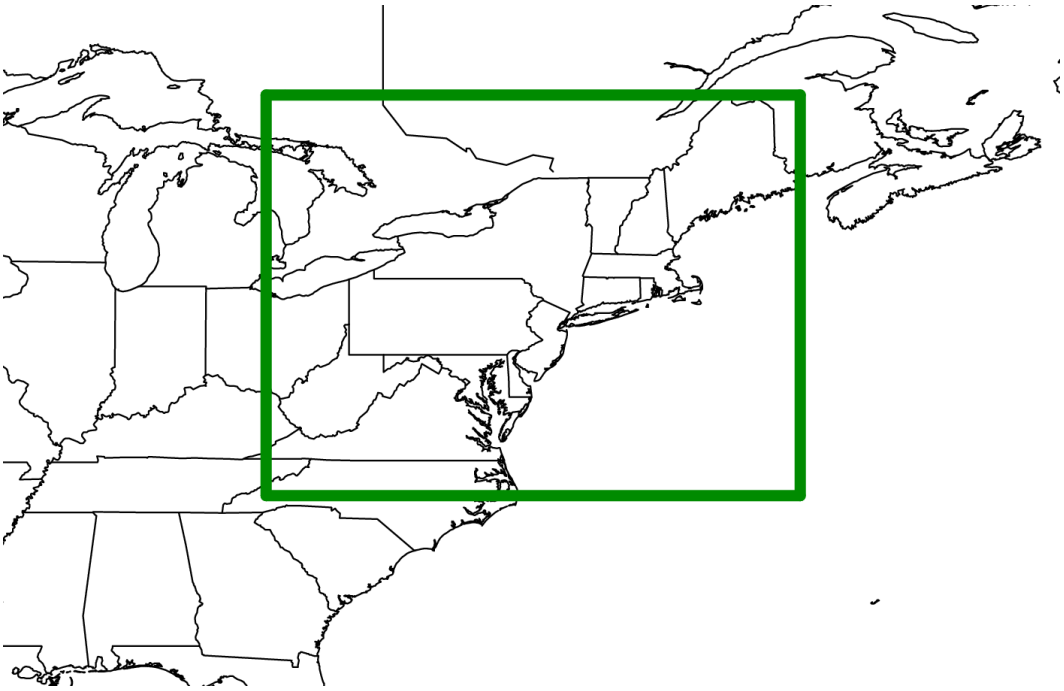

Figure 3.1: The domain used to calculate the snowfall event time series of Northeast snowfall event anomalies.

to the locations of features relative to the cyclone center (Lackmann et al. 1996).

Using sea-level pressure fields from the 32-km North American Regional Reanalysis (NARR; Mesinger et al. 2006) dataset, an initial analysis time (t = 0 h) for each heavy snowfall event was defined as the date and time the 6-h sea-level pressure tendency exceeded the average life-cycle 6-h pressure tendency of all snowfall events chosen for the composite analysis. A characteristic of the 30 Northeast snowstorms examined by Kocin and Uccellini (2005) was that the storms were associated with deepening surface pressures. All but three of the 30 cases showed a decrease in central pressure of at least 1 hPa $(3\ \mathrm{h})^{-1}$ and only 4 cases deepened 15 hPa or less during the 60-h period analyzed. Using pressure tendency to determine the initial analysis time provided a physically-based uniform snapshot of each surface cyclone's life cycle.

After the initial analysis time was determined for each snowfall event,

compositing software centered a 60° by 75° latitude-longitude grid on each surface cyclone's position to extract the NARR fields over that domain. The 32-km resolution grids were then moved to a common latitude–longitude position, averaged, and placed at the mean positions of the initial analysis times of all composited cases. The locations of the surface cyclones were also used at 6-h intervals, from 6 h before to 24 h after the initial analysis time, to show the evolution of the composite system. Finally, to display the resulting composite fields in a geographical framework, the mean latitude and longitude positions of the surface cyclones at each time were used. The results of the composite analysis procedure became the four-dimensional NCM for heavy snowfall that is investigated in this research.

3.2 Northeast Heavy Snow Conceptual Model Verification

3.2.1 Conceptual Model Representativeness

Before investigating the predictability of the NCM, the NCM's representativeness needs to be investigated. First, the NCM was qualitatively examined against existing heavy snow CMs developed in previous research (e.g., Kocin and Uccellini 1990; Nicosia and Grumm 1999; Banacos 2003; Kocin and Uccellini 2005; Moore et al. 2005; Novak et al. 2004, 2010). The fields and features focused on were those that are considered critical to the production of heavy snowfall in existing CMs (e.g., midlevel frontogenesis and deformation). The NCM was analyzed for the existence and placement of these fields with respect to the ETC center.

Once the qualitative analysis was complete, the NCM was quantitatively tested against the individual heavy snowfall events included in the NCM

Table 3.1: Fields, domains, and weights used for assessment of the NCM.

Field	Domain	Weight: COR-MAE
300-hPa height	Large	3-1
500-hPa height	Large	3-1
700-hPa height	Small	3-1
850-hPa height	Small	3-1
Sea-level pressure	Small	3-1
300-hPa isotachs	Large	3-1
850-hPa isotachs	Small	3-1
500-hPa RH	Small	2-1
700-hPa RH	Small	2-1
925-hPa mixing ratio	Small	2-1
PWTR	Small	2-1
700-hPa θ_e	Small	2-1
850-hPa θ_e	Small	2-1
850-hPa temp	Small	2-1
2-m temp	Small	2-1
700:850-hPa avg fgen	Small	3-1
PV	Large	3-1

(hereafter termed NCM members). Completing this analysis, as in Moore et al. (2003), allowed the following to be examined:

- representativeness of the typical conditions with Northeast heavy snowstorms.
- degree of variability within the NCM members.
- NCM members that may be discernibly different than the NCM.

In addition to the base fields associated with ETC CMs (i.e., mass, temperature, and moisture), the derived fields considered critical to the production of heavy snowfall found in the qualitative analysis were also tested. Statistics were computed and then combined to determine the robustness of these fields between the NCM and individual heavy snowfall events (Table 3.1).

The field statistics were computed by moving the NCM's surface cyclone center over the NCM member's surface cyclone centers and then positioning domains, as in Fig. 3.2, over the common center. Linear spatial correlations and mean absolute errors were computed over the large domain for large-scale fields and over the small domain for small-scale fields (Table 3.1 and Fig. 3.2). Next, the statistics for each field were combined to compute a field score that is equal to the correlation reduced by the normalized mean absolute error:

$$\text{field score} = \text{COR} - \frac{\text{MAE}}{\text{weight} \cdot \text{fctr}} \tag{3.2}$$

where COR is the linear spatial correlation, MAE is the mean absolute error, weight is the contribution of the COR and MAE to the field score (e.g., 75% COR to 25% MAE), and fctr is defined as:

$$\text{fctr} = \frac{\text{CLIMO } 95^{th} \text{ PCT MAE} - \text{CLIMO } 75^{th} \text{ PCT MAE}}{\text{CLIMO } 95^{th} \text{ PCT COR} - \text{CLIMO } 75^{th} \text{ PCT COR}} \tag{3.3}$$

where each term is the field's 30-year conditional climatological value of the linear spatial correlation or mean absolute error at the 95^{th} or 75^{th} percentile. The conditional climatology distribution for each field's statistics was determined by comparing the date and time 6 h after each NCM member's initial analysis time (i.e., t = +6 h) and the climatological dataset. After the comparison, each field's linear spatial correlation and mean absolute error distribution had approximately 712,800 values. The final field score for each field was weighted as shown in Table 3.1. For temperature and moisture fields, where the absolute values of the fields are more important, more contribution of the mean absolute error was given to the field score. Finally, a total score was computed for each NCM member by summing the 17 individual field scores. Summary statistics,

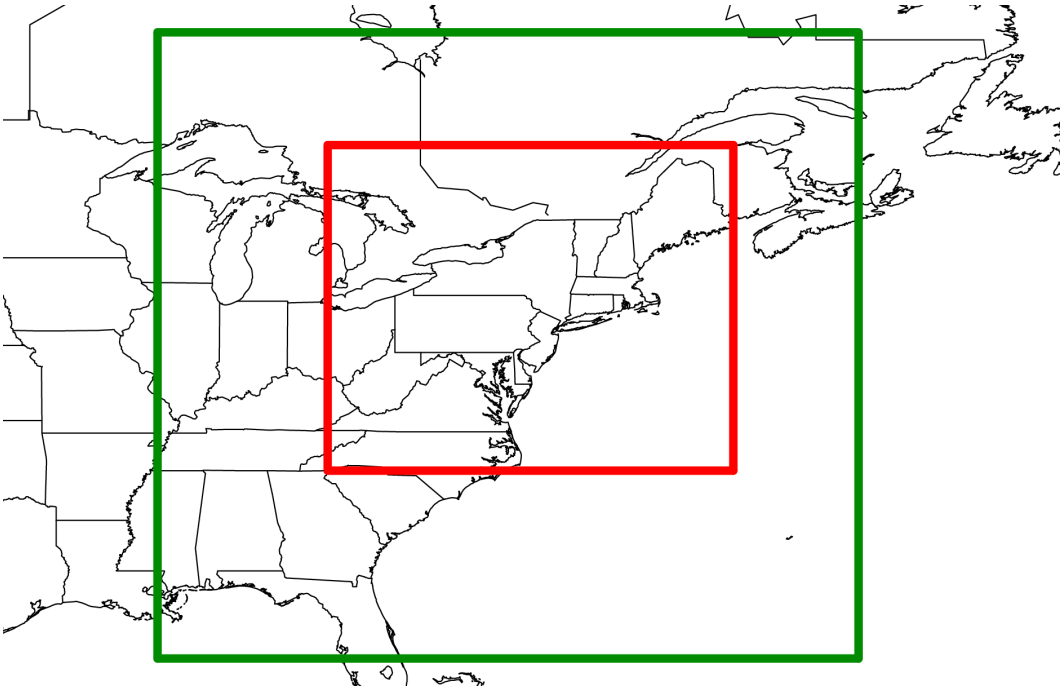

Figure 3.2: An example of the size of the domains used to calculate statistics between the NCM and the individual snowfall events included in the NCM.

including a lower threshold, were computed for each field and the total scores. The results of both the qualitative and quantitative analysis dictated the validity of the composite analysis procedure and if the NCM should be revised.

3.2.2 Conceptual Model Predictability

"Near misses" are defined by Kocin and Uccellini (2005) as situations in which heavy snow is a possible outcome from a forecasting perspective but does not materialize. To find "potential near misses", the NCM was compared to every surface low with a similar track that occurred during the months of December, January, and February between 1 December 1980 and 29 February 2008. It was important for the potential near miss surface lows to have similar tracks as the NCM because the sensible and latent heat fluxes from the western Atlantic Ocean have a significant impact on Northeast snowstorms (Kocin and

Uccellini 1990, 2005). Similar to the methodology in section 3.2.1, statistics and resultant total scores between the NCM and each potential near miss were computed when the associated surface low was in the approximate location of the NCM at t = +6 h (i.e., a time when the NCM would be affecting the Northeast). Each potential near-miss total score that exceeded the lowest NCM member total score was considered statistically similar to the NCM and a Northeast heavy snow near miss. Based on the collection of Northeast heavy snow near misses, the probability of detection (POD) and false-alarm ratio (FAR) were computed to investigate the predictability of the NCM.

3.3 Examination of Near Misses

Investigating the differences between the NCM and the Northeast heavy snow near misses will suggest which atmospheric fields are necessary conditions for heavy snowfall in the Northeast. Similar to the methodology in section 3.1.2, a composite analysis was created for the Northeast heavy snow near misses using the date and time found in 3.2.2. To statistically determine similarities and differences in fields, field statistics and resultant total scores were computed as in sections 3.2.1 and 3.2.2 between the NCM and the Northeast heavy snow near-miss composite. In addition to the domains used in Table 3.1 and Fig. 3.2, statistics were also computed on sub domains that partitioned the large and small domains into quadrants. The sub domains were necessary to exploit the differences between the NCM and near-miss composite in the different quadrants of the surface low.

Chapter 4. Northeast Heavy Snow Conceptual Model

4.1 Conceptual Model Development

To develop the NCM, organized Northeast snowfall events for the months of December, January, and February between 1 December 1980 and 29 February 2008 were objectively ranked. A total of 500 events were identified and the snowfall events were indexed by area-averaging and weighting the area encompassed by greater than the 2-in. snowfall isohyet similar to the method used for the Northeast Snowfall Impact Scale (NESIS) by Kocin and Uccellini (2004). Since the distribution of snowfall event indices was positively skewed, a power transformation using a value of λ equal to 0.34 was performed to make the distribution more symmetric (Fig. 4.1). Finally, standardized Northeast snowfall event anomalies were computed by subtracting the distribution mean of the transformed snowfall event index and dividing by the corresponding standard deviation. An organized Northeast snowfall event was categorized as heavy if the standardized anomaly was at least ≥ 1.0 (top-80 events). For example, snowfall statistics (Table 4.1) for the 10–13 February 1983 Northeast heavy snowfall event (Fig. 4.2) show that the area of greater than 2-in. of snowfall was twice as large as the average event and the total snowfall was more than two standard deviations above the climatological mean. This heavy snowfall event was ranked 9th and in the 98th percentile for all events which is similar to the NESIS rank by Kocin and Uccellini (2004).

The 80 Northeast heavy snow events were associated with Miller type-A (i.e., coastal), type-B (i.e., redevelopment), and continental surface-low tracks with Miller type-B tracks broken into redevelopment north and south of 38°

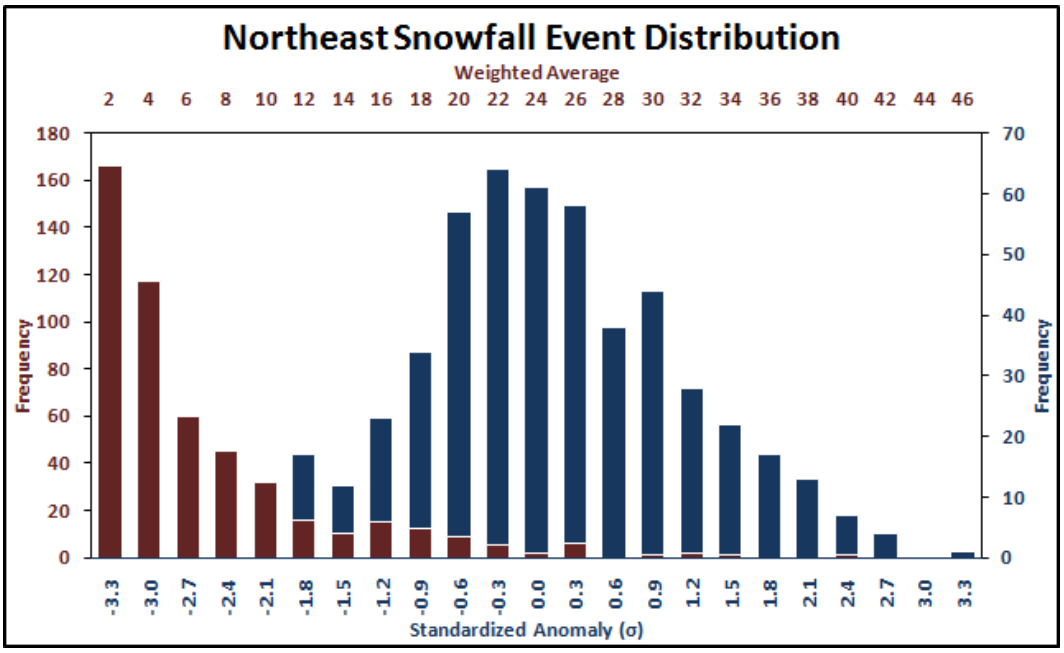

Figure 4.1: The frequency of organized Northeast snowfall events (red) and standardized anomalies of organized Northeast snowfall events (blue).

Table 4.1: Event snowfall statistics for the 96-h period ending 1200 UTC 13 February 1983.

13 February 1983 96-h heavy snow event
Area average >2.0 in.: 10.91 in.
No. total possible grid points: 22,302
No. grid points >2.0 in.: 6689
Climatological average No. grid points >2.0 in.: 2858
Gridded weight: 2.34
Gridded weight average: 25.49
Anomaly index: 2.30σ
Rank: 9th
NESIS rank: 10th

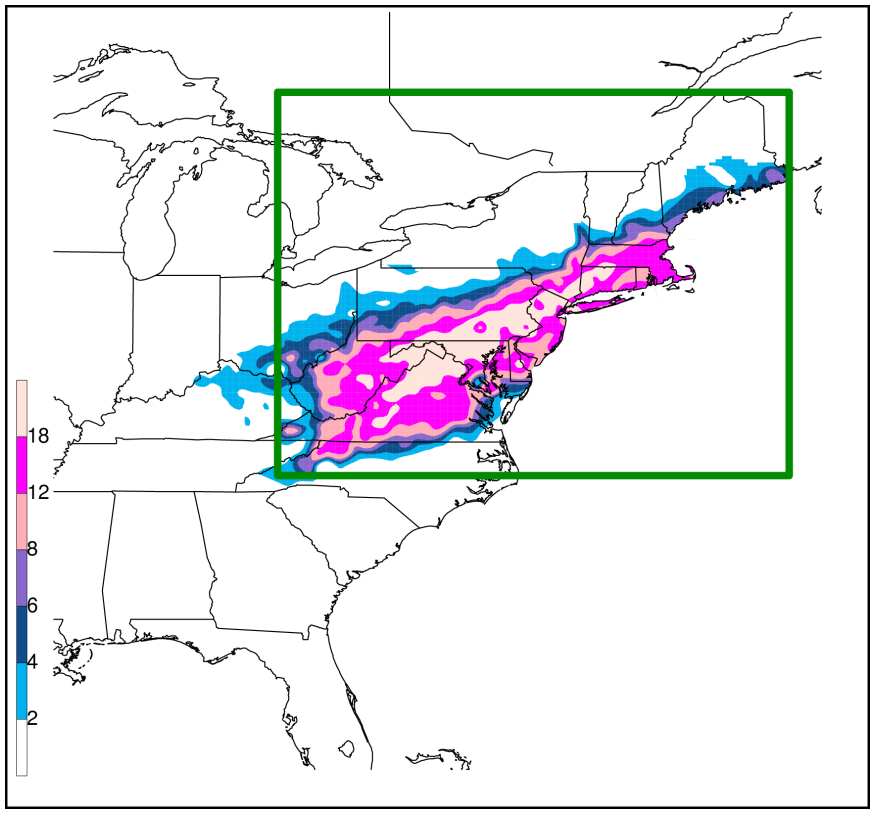

Figure 4.2: NCDC COOP event snowfall (in.) for the 96-h period ending at 1200 UTC 13 February 1983 and event snowfall statistical domain (green).

Table 4.2: The number of Northeast heavy snow events that fall within each surface low track category.

Surface low category	No. of events
Coastal	22
Redevelopment south of 38°N	22
Redevelopment north of 38°N	10
Continental	14
Undefinable	12

latitude (Table 4.2). Miller type-B surface lows that redeveloped south of 38° were combined with Miller type-A to make the dominant track category (n = 44) for inclusion in the NCM. This combination is justified because the Miller type-B surface lows tracked across more than two-thirds of the northern portion of the case selection domain shown in Fig. 4.2.

Similar to the 30 Northeast snowstorms examined by Kocin and Uccellini (2005), the 44 Northeast heavy snow events identified for the NCM featured a well-defined cyclonic circulation that strengthens off the East Coast. Kocin and Uccellini (2005) also found that all but 3 of the 30 snowstorms showed a decrease in central pressure of at least 1 hPa $(3\ \mathrm{h})^{-1}$ and only 4 cases deepened 15 hPa or less during the 60-h period analyzed. Using the NARR sea-level pressure fields, the NCM initial analysis time (t = 0 h) occurred when each NCM member surface low deepening rate exceeded the 44-member mean rate (6-h intervals) relative to climatological values bounded by the 80th parallel to the west, the 70th parallel to the east, the 44th meridian to the north, and 30th meridian to the south (Fig. 4.3). This area was selected because almost all of the snowstorms from Kocin and Uccellini (2005) underwent rapid intensification within that bounded region and the rapid intensification of cyclones in the western Atlantic Ocean has been shown to be a characteristic common to heavy snow-producing systems

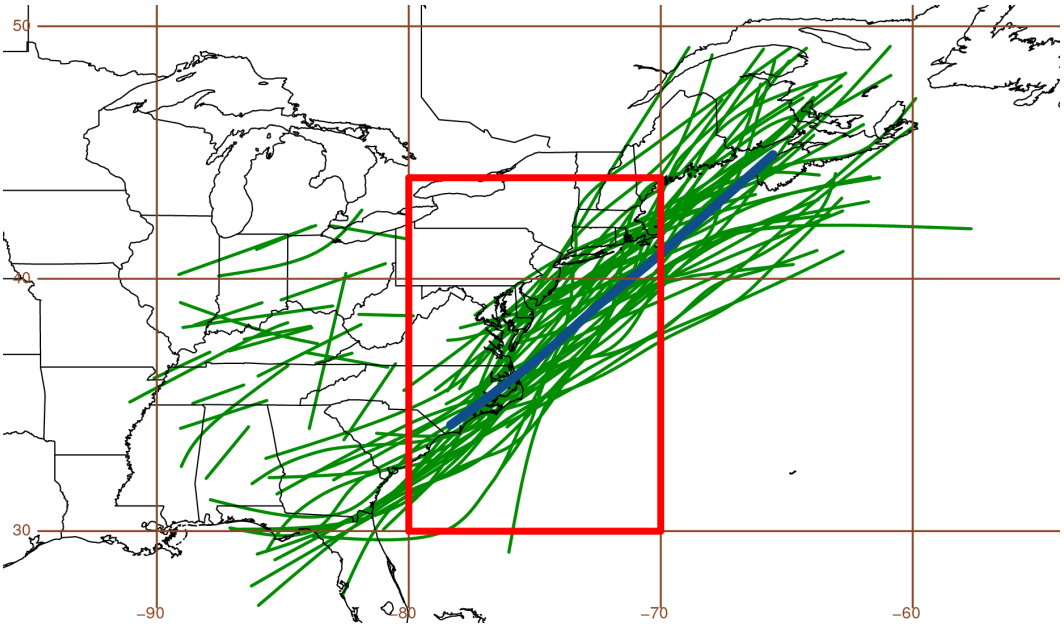

Figure 4.3: The 44 Northeast heavy snow event coastal surface low tracks (green) occurring during the months of December, January, and February between 1980 and 2008. The blue line represents the average track of the surface lows in the climatology.

that affect the Northeast (e.g., Brandes and Spar 1971; Sanders 1986b; Mote et al. 1997; Kocin and Uccellini 2005). For any NCM members that did not exceed the mean deepening rate within the bounded region, the initial analysis time was the max 6-h deepening rate.

Using the 44 NCM members and their respective initial analysis times, the NCM was created through a system-relative composite analysis approach utilizing the General Meteorological Package [GEMPAK; desJardins et al. 1991] and the NARR dataset. In addition to the initial analysis time, NCM composites were also calculated at 6-h intervals from 6 h before (t = -6 h) to 24 h after (t = +24 h) the initial analysis time to analyze the evolution of the NCM. The mean latitude and longitude positions of the surface lows at each time were used to display the resulting NCM fields in a geographical framework.

4.2 Analysis of Conceptual Model Members

4.2.1 Overview

All 44 Northeast heavy snow events identified for the NCM are listed in Table 4.3. To explore the magnitude of these events, a statistical assessment of the standardized anomalies was completed. The average standardized anomaly for the 44 NCM members is 1.79σ which is 0.33σ above the average anomaly for the remaining 36 top-80 events. Thirteen (87%) of the top 15 and 28 (70%) of the top-40 $\geq$ 1.0σ heavy snow events are NCM members. In contrast, NCM members consist of only 4 (27%) of the bottom 15 and 17 (43%) of the bottom-40 heavy snow events. These results suggest that the members classified for the NCM include the majority of the heaviest snow events in the top 80.

The surface low track and intensity characteristics of the NCM members are consistent with the findings from previous snowstorm studies (Miller 1946; Kocin and Uccellini 2005). The majority of the surface low tracks, shown in Fig. 4.3, are clustered around the mean track that begins (t = -6 h) near Wilmington, North Carolina and ends (t = +24 h) just east of the Bay of Fundy. While there is more variability in the surface low tracks east of the 73rd meridian, they are within the envelope of East Coast snowstorm tracks found by Kocin and Uccellini (2005). The track segments in Fig. 4.3 over the Ohio Valley and west of the Appalachian Mountains are the portion of the Miller type-B NCM member surface low tracks before secondary redevelopment along the East Coast. The cluster of surface low track segments are similar in location to the 13 redevelopment snowstorms found in Kocin and Uccellini (2005).

As illustrated in section 4.1, Northeast snowstorms are associated with deepening surface cyclones. To examine NCM member deepening rates, surface

Table 4.3: The 44 Northeast heavy snow events identified for the NCM. NCM members are listed in descending order of Northeast heavy snow event anomaly.

Anomaly rank	Ending date	Duration (h)	Surface low track	Anomaly (σ)
1	9 Jan 1996	168	Coastal	3.09
2	19 Feb 2003	144	Redevelop south of 38°N	2.69
3	24 Jan 1987	96	Coastal	2.66
4	15 Feb 2007	120	Redevelop south of 38°N	2.65
5	8 Dec 2003	144	Coastal	2.48
6	6 Feb 1995	96	Redevelop south of 38°N	2.33
8	5 Jan 1994	96	Coastal	2.32
10	16 Dec 2003	120	Coastal	2.25
11	22 Dec 1995	144	Redevelop south of 38°N	2.22
12	25 Jan 2005	120	Redevelop south of 38°N	2.13
13	16 Jan 1999	96	Redevelop south of 38°N	2.07
14	4 Jan 1987	96	Coastal	2.00
15	27 Jan 2000	96	Coastal	1.96
17	8 Feb 1983	120	Coastal	1.93
18	15 Jan 1982	96	Coastal	1.92
20	17 Dec 2007	96	Redevelop south of 38°N	1.86
21	13 Feb 1988	120	Redevelop south of 38°N	1.86
22	17 Jan 1983	96	Redevelop south of 38°N	1.85
24	1 Jan 2001	120	Coastal	1.81
25	26 Dec 2002	96	Redevelop south of 38°N	1.81
26	31 Jan 1990	72	Redevelop south of 38°N	1.79
27	31 Dec 1997	72	Coastal	1.76
29	5 Jan 2003	120	Redevelop south of 38°N	1.75
31	7 Dec 1984	96	Coastal	1.75
32	9 Jan 1994	144	Redevelop south of 38°N	1.73
37	13 Jan 1987	144	Redevelop south of 38°N	1.64
39	9 Jan 1988	96	Coastal	1.61
40	6 Feb 2001	48	Coastal	1.59
41	13 Jan 1991	120	Redevelop south of 38°N	1.55
44	8 Jan 2002	72	Coastal	1.46
45	13 Feb 2006	72	Coastal	1.44
46	18 Feb 1996	120	Coastal	1.44
47	26 Jan 1988	96	Coastal	1.44
50	13 Jan 1996	96	Redevelop south of 38°N	1.43
53	14 Feb 1993	120	Redevelop south of 38°N	1.42
54	1 Feb 2000	168	Redevelop south of 38°N	1.42
55	10 Dec 2005	96	Redevelop south of 38°N	1.38
61	22 Jan 2000	96	Redevelop south of 38°N	1.32
62	14 Feb 2008	96	Redevelop south of 38°N	1.30
63	17 Dec 1981	96	Coastal	1.22
72	27 Jan 1987	72	Coastal	1.11
77	26 Feb 1998	96	Coastal	1.06
78	23 Dec 1993	96	Coastal	1.04
80	21 Dec 2000	96	Redevelop south of 38°N	1.03

Table 4.4: Surface-low pressure summary statistics for the 44 Northeast heavy snow events.

	Surface low pressure at t = 0 h (hPa)	**Adjusted[1] 6-h surface low pressure tendency at t = 0 h (hPa)**	**24-h surface low pressure decrease (hPa)**	**Adjusted[1] 24-h surface low pressure decrease (hPa)**	**Avg 6-h surface low pressure tendency (hPa)**	**Avg Adjusted[1] 6-h surface low pressure tendency (hPa)**
Mean	1001.5	-4.7	-20.0	-15.3	-5.1	-3.9
Median	1001.2	-4.1	-19.7	-14.7	-5.0	-3.7
Std dev	6.8	2.0	7.9	7.8	1.9	1.9
75th pct	997.1	-5.5	-26.2	-21.1	-6.6	-5.3
25th pct	1005.5	-3.3	-12.7	-8.9	-3.2	-2.2

[1]The adjusted surface pressure tendency removes the climatological pressure decrease associated with the northward movement of the cyclone.

low pressure values were extracted for each member between t = -6 h and t = +18 h. Over the 24-h period, every NCM member surface low deepened for at least 18 hours and the average member 24-h pressure decrease and rate ending at t = +18 h was -20 hPa and -5.1 hPa $(6\ \text{h})^{-1}$, respectively (Table 4.4). However, since the cyclones are moving poleward, there is a climatological decrease in pressure which was determined by computing a 15-day running average over 30 years. The results indicate that approximately 25% of the average 24-h pressure decrease and rate is due to the increase in planetary vorticity. The NCM members also underwent periods of rapid intensification. Deepening rates exceeding -6 hPa $(6\ \text{h})^{-1}$ occurred in 29 of 44 members and -12 hPa $(12\ \text{h})^{-1}$ in 23 of 44 members. Surface low tracks for these rapidly intensifying NCM members are in similar locations to the tracks of explosive cyclones found by Roebber (1984) and Sanders (1986a).

4.2.2 Statistical Analysis

Field and total score summary statistics at t = +6 h for the 44 NCM members were computed on the full domains in Fig. 3.2 and are listed in Table 4.5. For mass fields, the measures of center decrease while the variability increases from upper to lower levels. 850-hPa height and sea-level pressure scores have more variability and lower measure of center values due to large height and pressure gradients associated with mid-latitude cyclones. Large gradients can also have an impact on isotach and relative humidity field scores as the means and medians are lower. For example, slight displacement of the dry conveyor belt depicted in the 500- and 700-hPa relative humidity fields, when compared to the NCM, can lead to a decrease in those field scores. Overall, low-level moisture and temperature field scores have similar median and standard deviation values. The NCM member 2-m temperature field scores tend to be higher and have the least variability than all other fields. This is likely due to the fact that a large portion of the mesoscale domain (Fig. 3.2) is over the ocean where low-level temperatures are more diurnally consistent when compared with those over land.

To find NCM members that may be statistically different than the NCM, the total scores that are presented in Table 4.5 (lower right) were examined. The distribution of total scores is negatively skewed (-0.289) and is supported by the summary statistics since the minimum total score is over two standard deviations from the median while the maximum total score is less than two. Furthermore, Fig. 4.4 shows that the slope of the total score distribution was relatively consistent until the last four total scores, where the decrease of the slope increased by 4.5 times. An examination of height and pressure fields from the three lowest scoring NCM members, 31 January 2000 (1.42σ), 9 December

Table 4.5: Field and total score summary statistics for the 44 Northeast heavy snow events.

	300-hPa height	**500-hPa height**	**700-hPa height**	**850-hPa height**	**Sea-level pressure**	**300-hPa isotachs**
Mean	0.933	0.925	0.877	0.788	0.646	0.386
Median	0.937	0.929	0.894	0.817	0.657	0.432
Std dev	0.035	0.036	0.067	0.115	0.181	0.205
Maximum	0.983	0.981	0.978	0.952	0.904	0.699
Minimum	0.842	0.822	0.648	0.390	0.163	-0.137

	850-hPa isotachs	**500-hPa RH**	**700-hPa RH**	**925-hPa mixing ratio**	**PWTR**	**700-hPa θ_e**
Mean	0.582	0.391	0.392	0.848	0.794	0.747
Median	0.591	0.450	0.419	0.861	0.814	0.774
Std dev	0.132	0.241	0.187	0.058	0.080	0.088
Maximum	0.790	0.685	0.675	0.939	0.906	0.909
Minimum	0.320	-0.310	-0.399	0.689	0.605	0.569

	850-hPa θ_e	**850-hPa temp**	**2-m temp**	**700:850-hPa avg fgen**	**PV**	**Total score**
Mean	0.819	0.844	0.939	0.229	0.596	11.738
Median	0.832	0.861	0.947	0.258	0.610	11.743
Std dev	0.072	0.065	0.024	0.225	0.127	1.079
Maximum	0.929	0.939	0.970	0.571	0.831	13.525
Minimum	0.642	0.685	0.862	-0.380	0.263	9.168

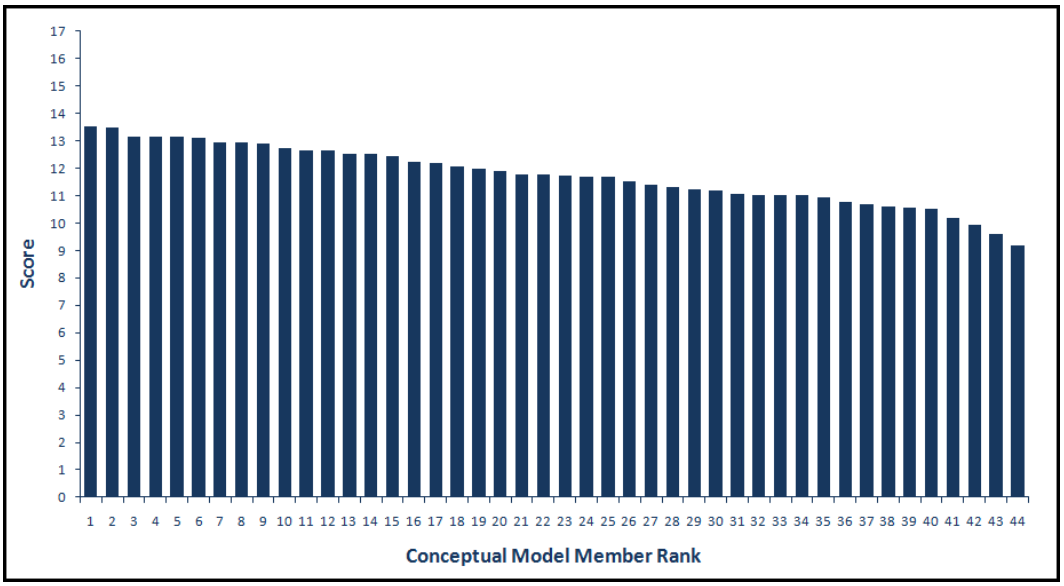

Figure 4.4: Total score distribution for the 44 Northeast heavy snow events.

2005 (1.38σ), and 14 February 2008 (1.30σ) revealed that these systems had positively titled 850-hPa troughs that did not develop closed cyclonic circulations until at least t = +18 h. In contrast, the fourth lowest total scoring NCM member, 5 December 2003 (2.48σ), was beginning to develop a closed cyclonic circulation which is consistent with the NCM at t = +6 h. Therefore, the three lowest scoring NCM members will be considered outliers and from here forward the remaining analysis will include the NCM with 41 members. After removing the 3 outliers (7% of members) and recomputing the summary statistics, the total score distribution became more symmetric. The skewness of the distribution was negligible (0.042) while the standard deviation dropped by 15% (not shown). A meteorological analysis of the outliers would be interesting, but beyond the scope and intent of this study.

4.3 Analysis of Conceptual Model

4.3.1 Synoptic-Scale Analysis

The NCM surface low is located over Wilmington, North Carolina (Fig. 4.5a), and is associated with a positively-tilted midlevel trough (Fig. 4.5c) at t = -6 h. The primary surface anticyclonic circulation is located downstream from the surface low across central Maine (Fig. 4.5a). At 850 hPa, an amplified, open cyclonic circulation is located over the mid-Atlantic states with a 30-kt low-level jet streak (LLJ) implying that warm, moist air is being transported poleward over the Gulf Stream (Fig. 4.5b). Weak upper-level diffluence downstream of a longwave trough is accompanied by two 100-kt jet streaks at 300 hPa (Fig. 4.5d). The upstream jet streak is found exiting the base of the 300-hPa trough while the jet streak downstream is located off the coast of Maine in association with confluent flow (Fig. 4.5d).

At the initial analysis time, the NCM surface low pressure has deepened approximately 4 hPa as it moved northeastward along the Atlantic Coast (Fig. 4.6a). The 850-hPa circulation has not completely closed, but has strengthened as the LLJ intensifies (Fig. 4.6b). At 500 hPa, the shortwave trough has become negatively tilted and the vorticity maxima has strengthened (Fig. 4.6c) which implies an increase in DPVA downstream from the trough axis. Surface cyclogenesis continued partially, due to the left-exit region of the 300-hPa jet streak exiting the base of the trough (Fig. 4.6d), resulting in implied upper-level divergence.

The NCM cyclone is beginning to occlude off the southeastern New Jersey coast 6 h later (t = +6 h) and has deepened approximately 6 hPa (Fig. 4.7a). Strengthening of the 850-hPa low has occurred as two closed height contours are

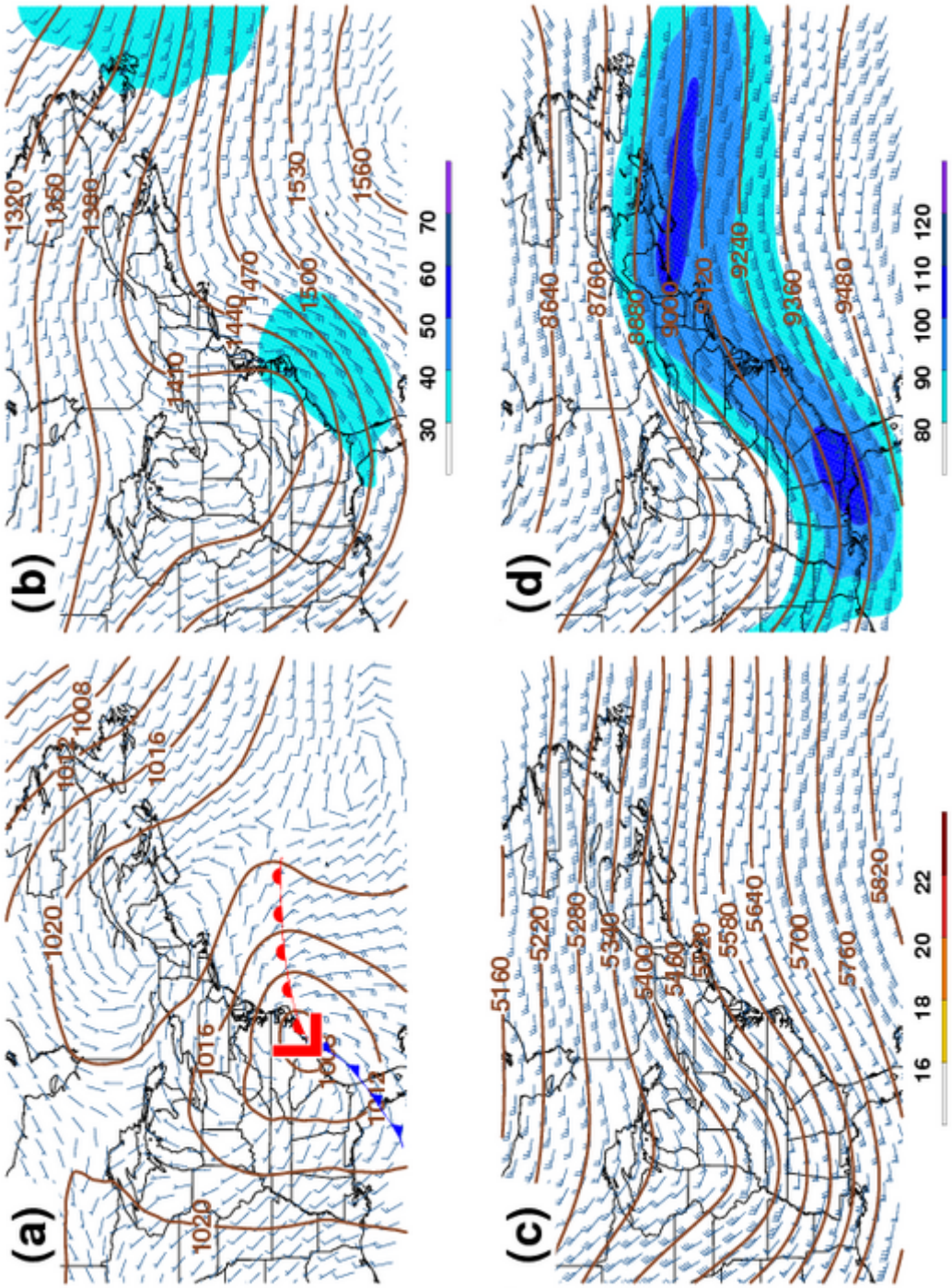

Figure 4.5: Northeast conceptual model at t = -6 h: (a) sea level pressure (solid brown; hPa) and 10-m wind (barbs; kts); (b) 850-hPa geopotential height (solid brown; m), wind speed (shaded; kts), and winds (barbs; kts); (c) 500-hPa geopotential height (solid brown; m), absolute vorticity (shaded; 10 $\times 10^{-5}$ s^{-1}), and winds (barbs; kts); (d) 300-hPa geopotential height (solid brown; m), wind speed (shaded; kts), and winds (barbs; kts). Surface low pressure center and fronts are shown in (a).

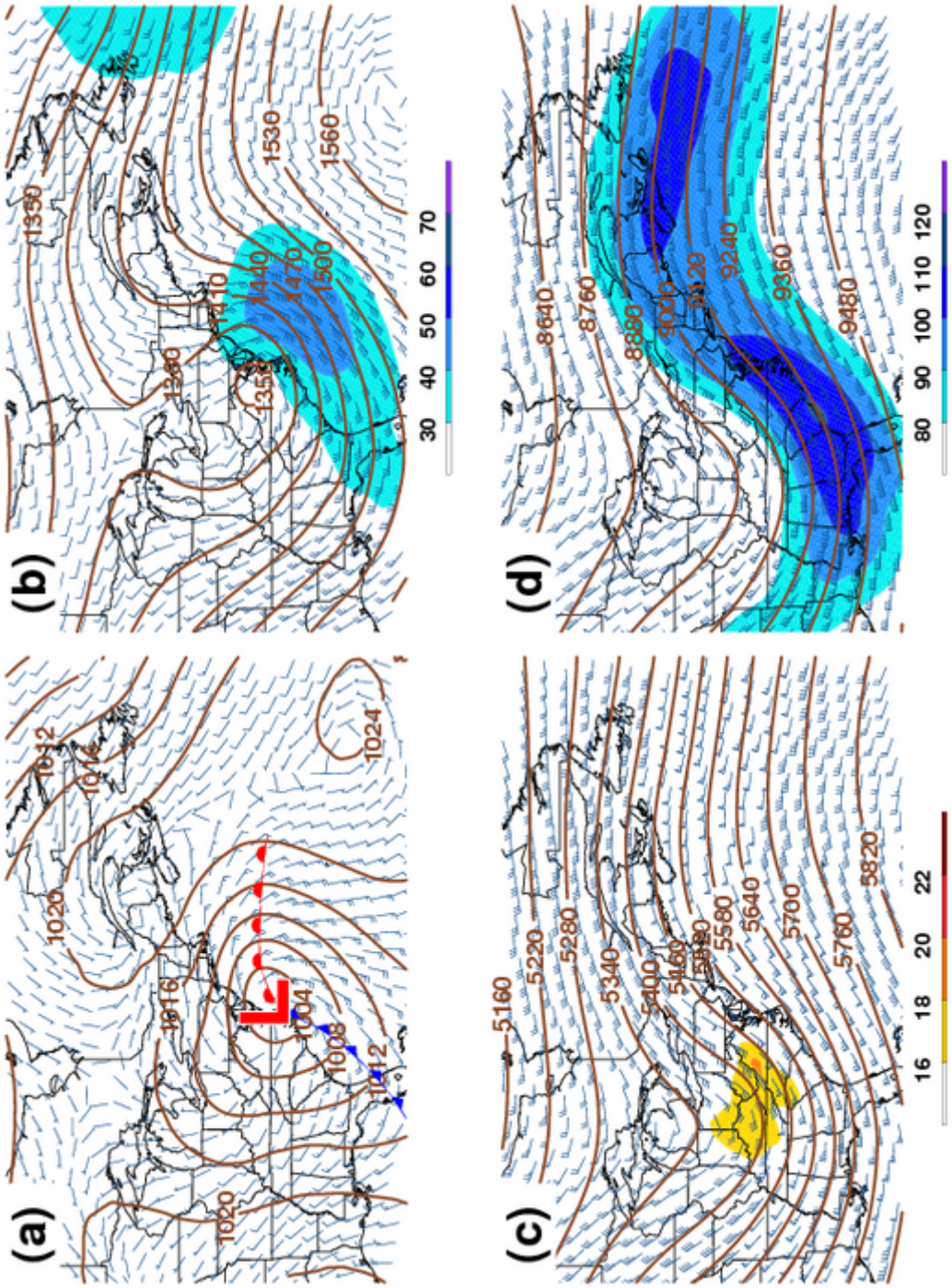

Figure 4.6: Northeast conceptual model at t = 0 h: (a) sea level pressure (solid brown; hPa) and 10-m wind (barbs; kts); (b) 850-hPa geopotential height (solid brown; m), wind speed (shaded; kts), and winds (barbs; kts); (c) 500-hPa geopotential height (solid brown; m), absolute vorticity (shaded; 10 $\times 10^{-5}$ s^{-1}), and winds (barbs; kts); (d) 300-hPa geopotential height (solid brown; m), wind speed (shaded; kts), and winds (barbs; kts). Surface low pressure center and fronts are shown in (a).

evident and a cyclonic-turning 50-kt LLJ is to the east and north of the cyclone. The stronger low-level wind fields suggest an increase in moisture and thermal advections into the system (Fig. 4.7b). Low-level mixing ratio and temperature fields depict a well-developed warm sector with moisture and thermal ridges extending into the NCM cyclone's circulation (Fig. 4.8). Flow along the aforementioned ridge axes implies strong moisture transport and warm air advection toward the northwestern quadrant of the NCM (Fig. 4.7). Aloft, implied upper-level divergence continues to increase above the deepening surface low as the 500- and 300-hPa troughs become negatively tilted (Figs. 4.7c,d). This, along with the increase in warm air advection downstream of the surface low, allowed the midlevel ridge to amplify.

During the next 12 h, the NCM surface low and 850-hPa heights continue to deepen (Figs. 4.9a,b). As the NCM circulation builds upward, a closed 700-hPa circulation develops (not shown). These height falls are in response to ongoing baroclinicity as the 500-hPa trough amplifies and becomes more negatively tilted (Fig. 4.9c). At 300 hPa, the double jet structure continues to strengthen as the downstream jet-streak back builds over eastern Quebec (Fig. 4.9d). In addition, coupling between the convergent flow from the 850-hPa LLJ right-entrance region of the upper-level jet streak is producing enhanced rising motion across portions of the northern Mid-Atlantic and New England.

4.3.2 Mesoscale Analysis

At t = 0 h, the NCM 850- and 700-hPa frontogenetical axes are oriented west-east across the Mid-Atlantic (Fig. 4.10a) and southern New England (Fig. 4.11a), respectively. The axes are embedded within low-level diffluent flow

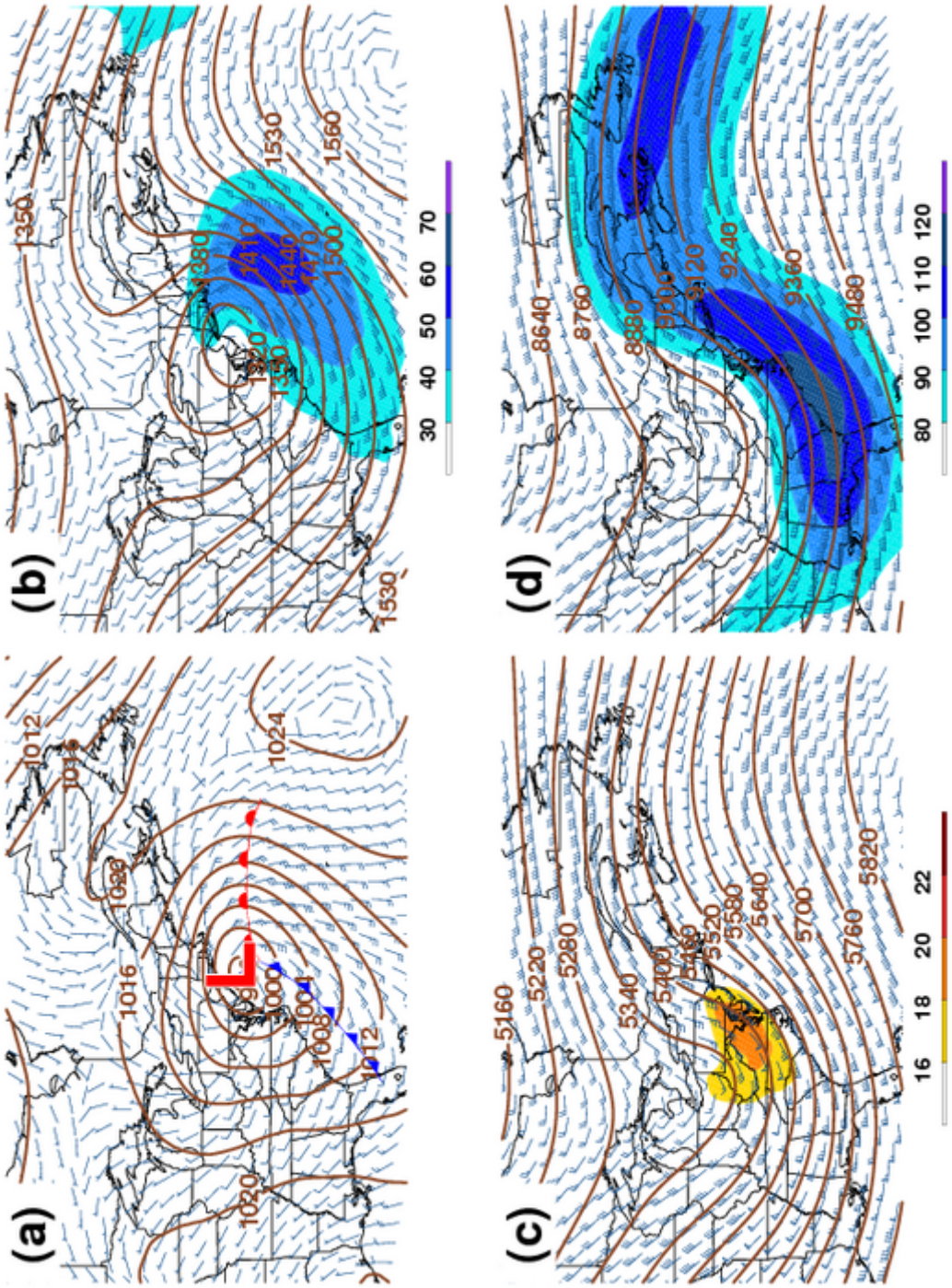

Figure 4.7: Northeast conceptual model at t = +6 h: (a) sea level pressure (solid brown; hPa) and 10-m wind (barbs; kts); (b) 850-hPa geopotential height (solid brown; m), wind speed (shaded; kts), and winds (barbs; kts); (c) 500-hPa geopotential height (solid brown; m), absolute vorticity (shaded; 10 $\times 10^{-5}$ s^{-1}), and winds (barbs; kts); (d) 300-hPa geopotential height (solid brown; m), wind speed (shaded; kts), and winds (barbs; kts). Surface low pressure center and fronts are shown in (a).

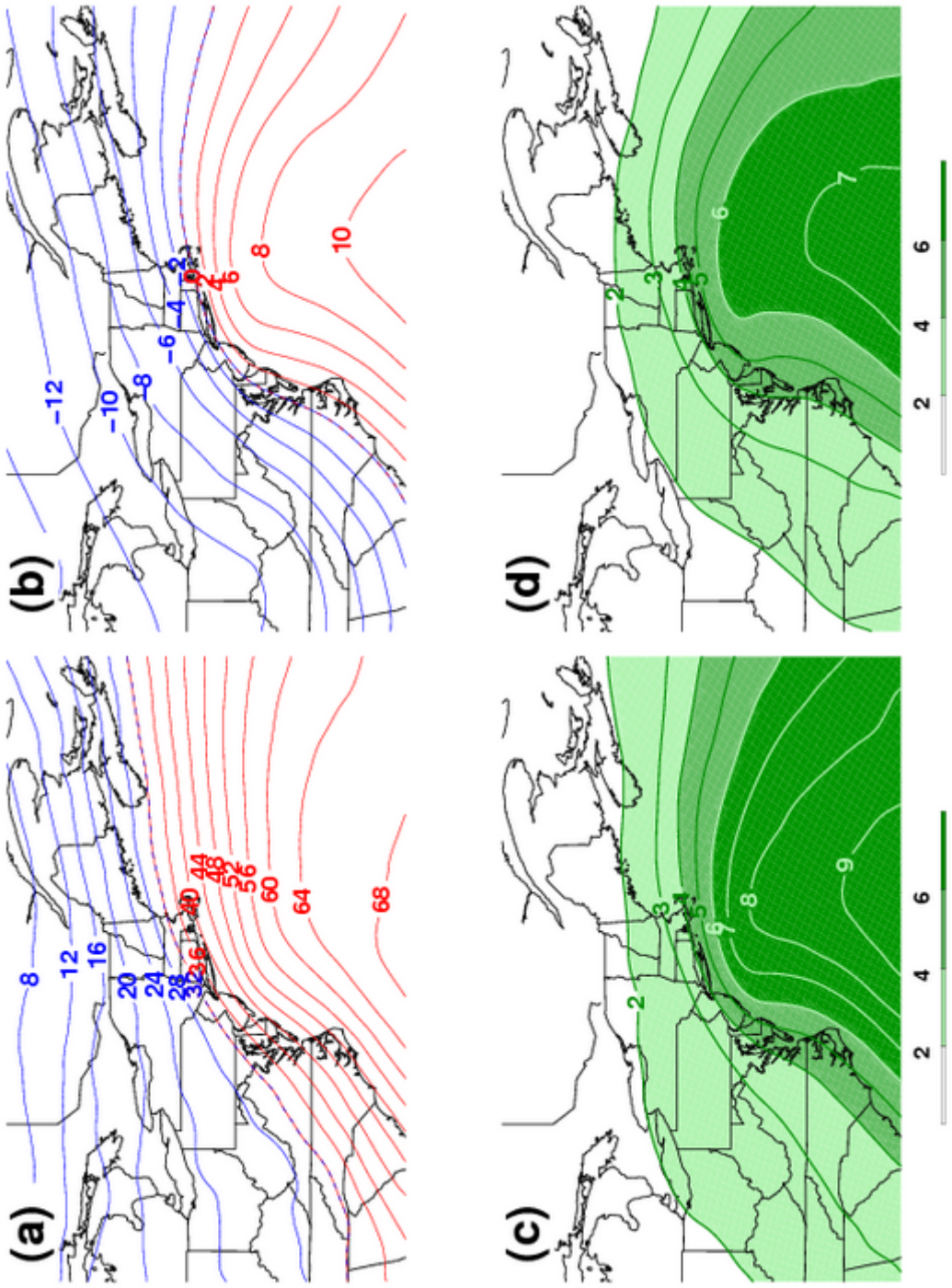

Figure 4.8: Northeast conceptual model at t = +6 h: (a) 2-m temperature (solid; °F); (b) 850-hPa temperature (solid; °C); (c) 925-hPa mixing ratio (shaded; 10 $\times 10^{-3}$ g kg^{-1}); (d) 850-hPa mixing ratio (shaded; 10 $\times 10^{-3}$ g kg^{-1}).

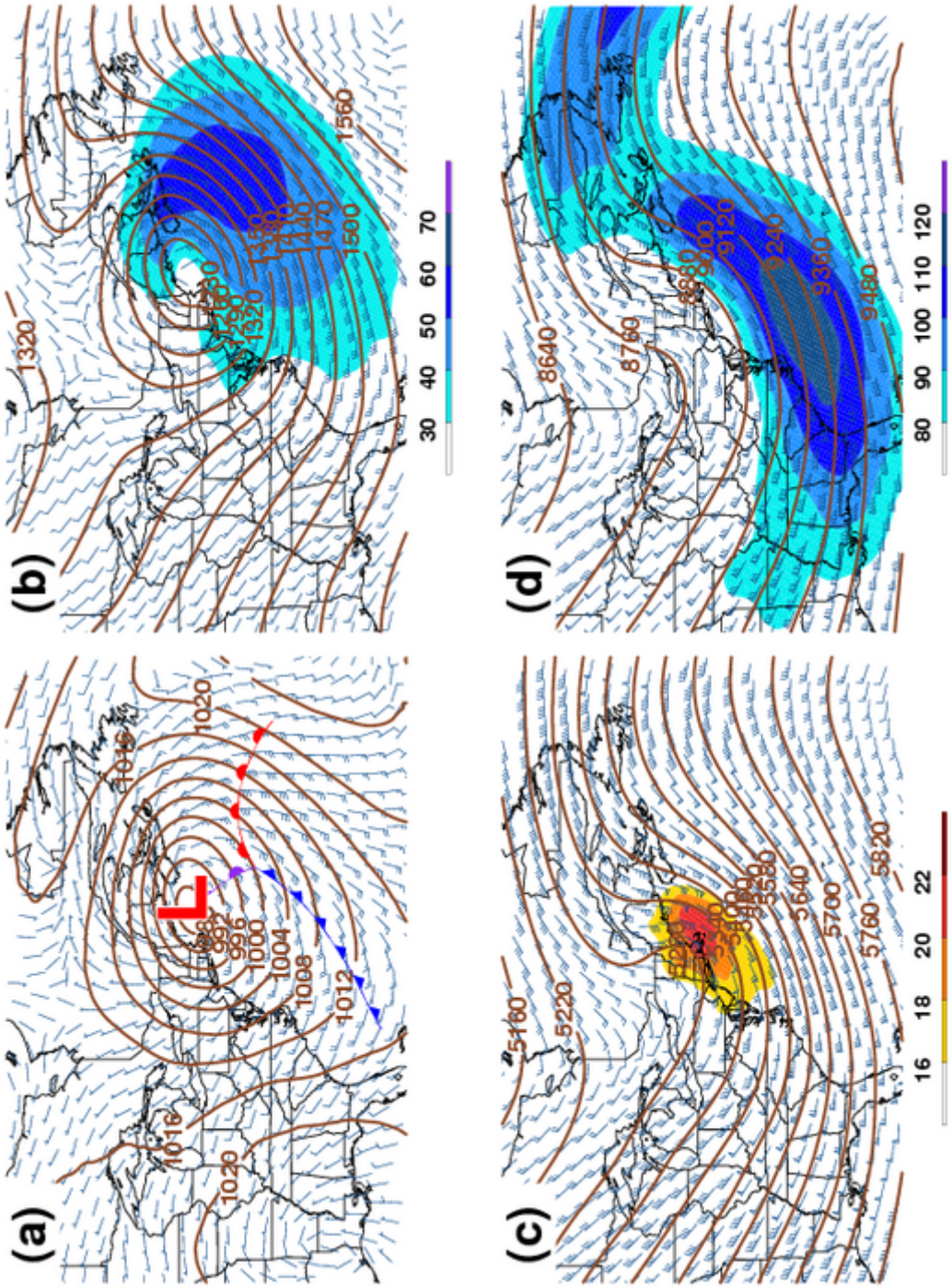

Figure 4.9: Northeast conceptual model at t = +18 h: (a) sea level pressure (solid brown; hPa) and 10-m wind (barbs; kts); (b) 850-hPa geopotential height (solid brown; m), wind speed (shaded; kts), and winds (barbs; kts); (c) 500-hPa geopotential height (solid brown; m), absolute vorticity (shaded; 10 $\times 10^{-5}$ s^{-1}), and winds (barbs; kts); (d) 300-hPa geopotential height (solid brown; m), wind speed (shaded; kts), and winds (barbs; kts). Surface low pressure center and fronts are shown in (a).

and warm-air advection associated with the exit region of the low-level wind maximum. Six hours later, an increase in 850- (Fig. 4.10b) and 700-hPa frontogenesis (Fig. 4.11b) is evident as values along both axes nearly double. This is likely due to the cyclonic circulation strengthening at midlevels, which implies an increase in the WCB, deformation, and frontogenesis in the 850-700-hPa layer. The frontogenetical axes continue to rotate counterclockwise and finally weaken as the cyclone becomes vertically stacked at t = +18 h.

Cross-section analysis at t = 0 h, oriented approximately 200-300 km downstream of the 700-hPa trough or low (i.e., inset in Figs. 4.12 and 4.13, top) and similar to Novak et al. (2004), shows a direct thermal circulation associated with the frontogenetical axis tilting to the northwest with height. Isentropes of θ_{es} (Fig. 4.12, top) show a convectively unstable environment within the warm sector and reduced stability above the frontogenetical axis as θ_{es} is nearly decreasing with height. Upward vertical motion with an environment near saturation is present within the dendritic growth zone (DGZ) in Fig. 4.12 (bottom). However, the maximum upward vertical motion is below the DGZ which implies needles and columns as the dominate ice crystal habit. By t = +12 h, coupling between the strengthening direct thermal circulation with increasing midlevel frontogenesis and the indirect thermal circulation from the exit region of the upper-level jet streak increased vertical velocity above the frontal zone (Fig. 4.13, top). This, in combination with reduced stability, allowed the vertical velocity field to contract and strengthen. In addition, a secondary vertical velocity maximum is evident within a saturated portion of the DGZ that suggests the presence of dendrites and increased snowfall rates, which are characteristics of single banded snowstorms.

In Fig. 4.14, NCM analyses of 700-hPa θ_e are presented. At t = 0 h (Fig. 4.14a)

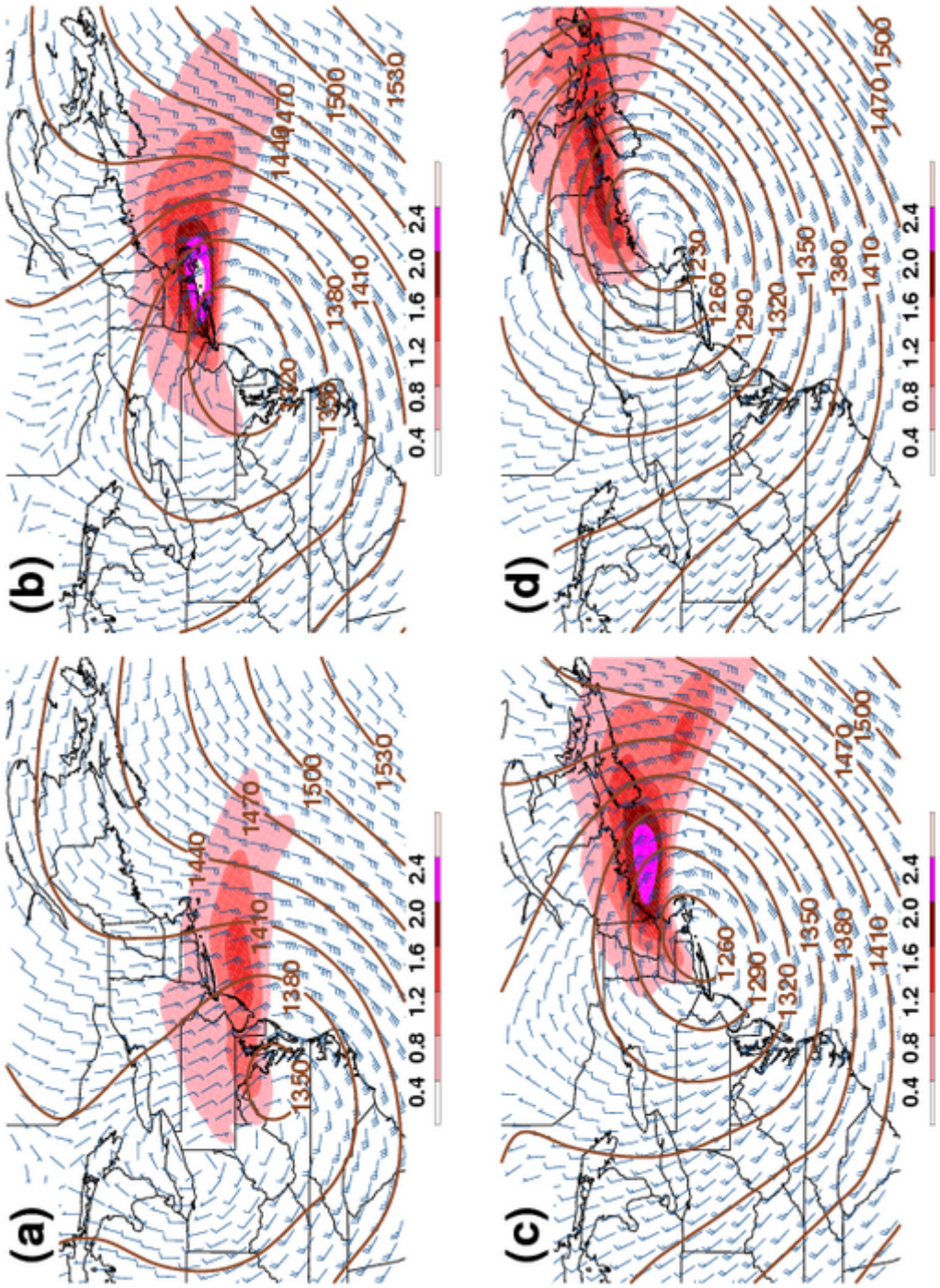

Figure 4.10: Northeast conceptual model 850-hPa geopotential height (solid brown; m) and Petterssen frontogenesis (shaded, K (100 km)$^{-1}$ (3 h)$^{-1}$) at: (a) t = 0 h; (b) t = +6 h; (c) t = +12 h; (d) t = +18 h.

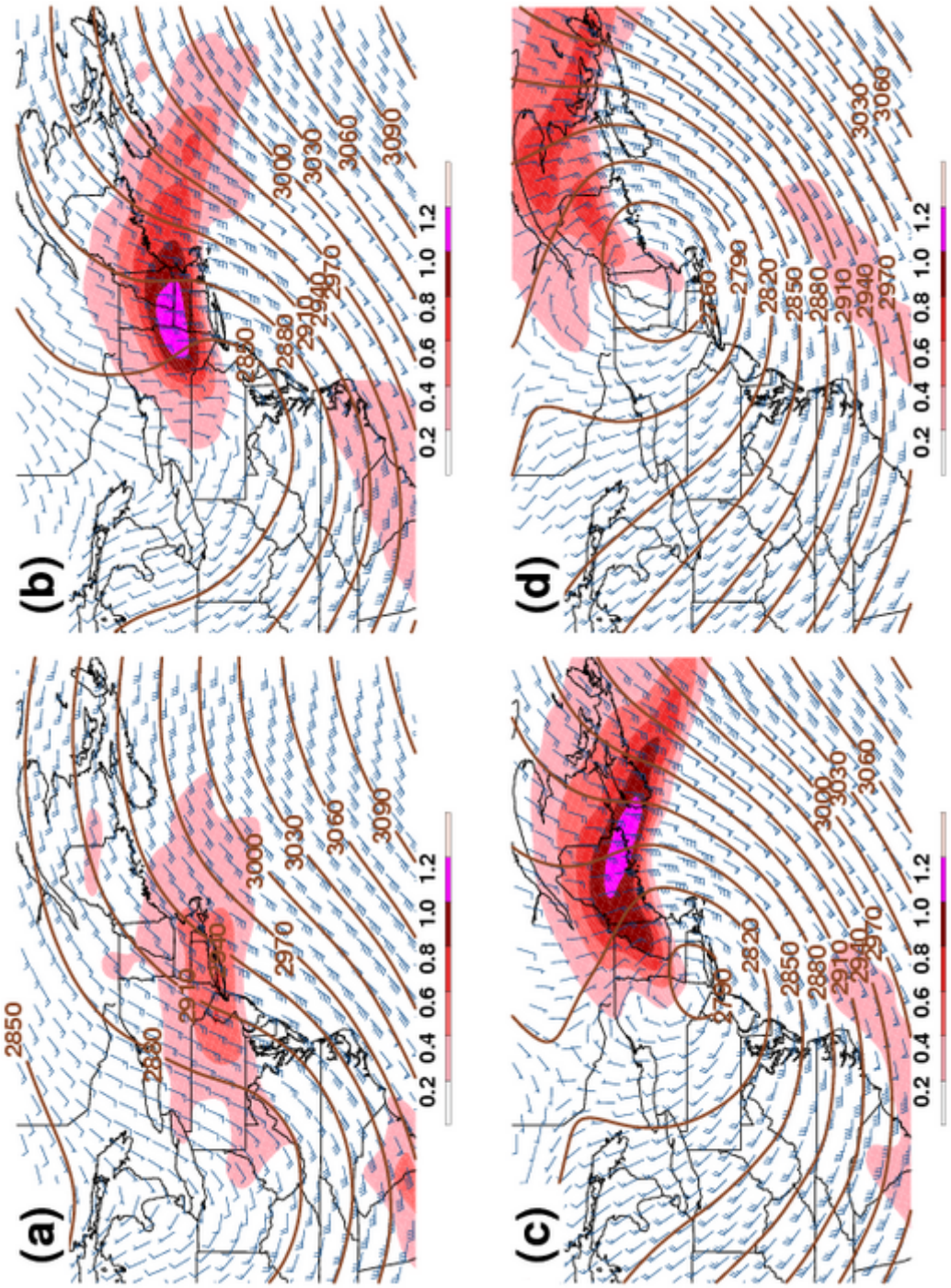

Figure 4.11: Northeast conceptual model 700-hPa geopotential height (solid brown; m) and Petterssen frontogenesis (shaded, K (100 km)$^{-1}$ (3 h)$^{-1}$) at: (a) t = 0 h; (b) t = +6 h; (c) t = +12 h; (d) t = +18 h.

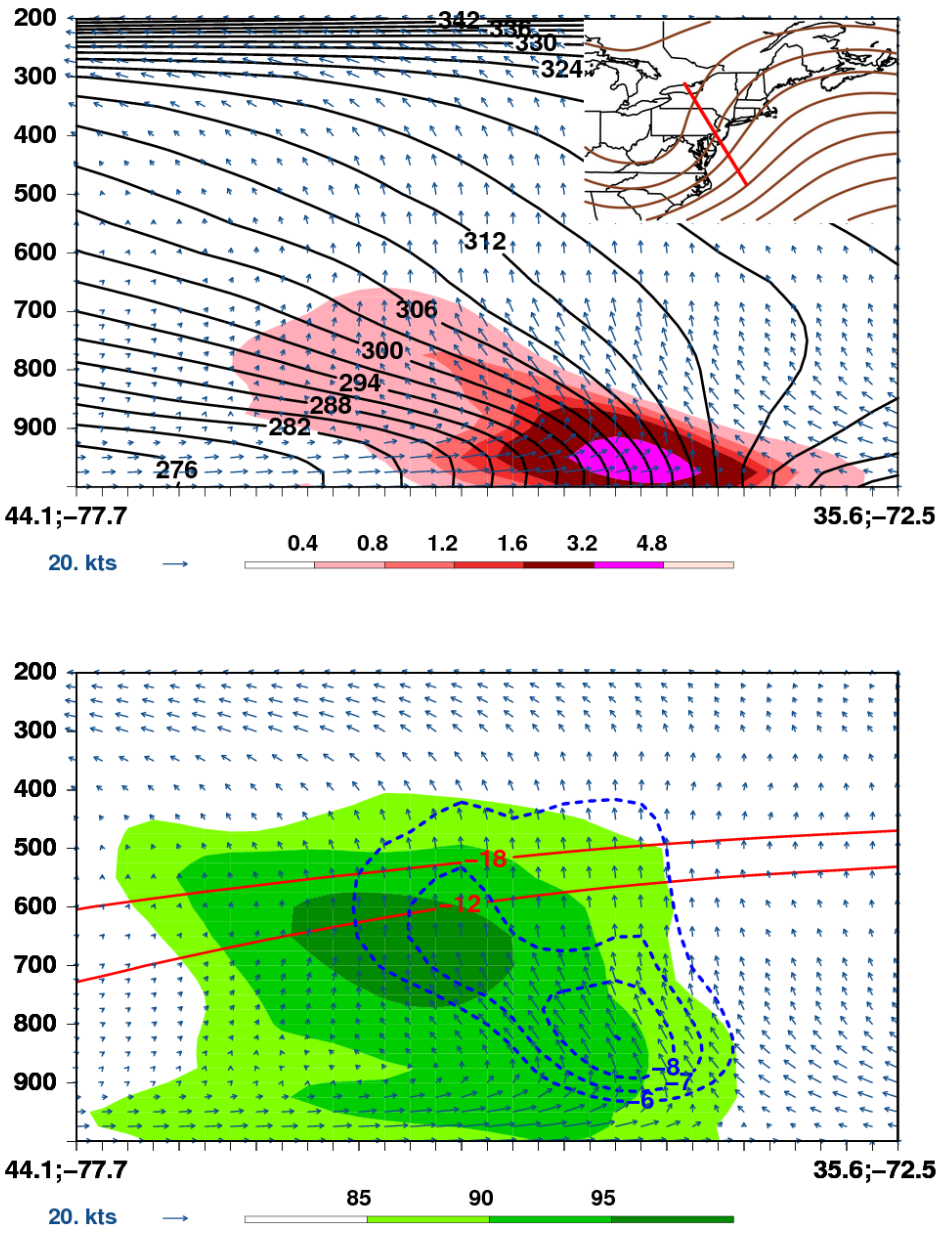

Figure 4.12: Northeast conceptual model vertical cross-section at t = 0 h: (top) saturation equivalent potential temperature (solid black, K), Petterssen frontogenesis (shaded, K (100 km)$^{-1}$ (3 h)$^{-1}$), and ageostrophic winds (arrows, kts); (bottom) omega (dashed blue, μb s^{-1}), relative humidity with respect to ice (shaded, >85%), dendritic growth zone from -12°C to -18°C (solid red, °C), and ageostrophic winds (arrows, kts). Inset Figure depicts the orientation of the vertical cross-section with 700-hPa heights (solid brown, m) for reference.

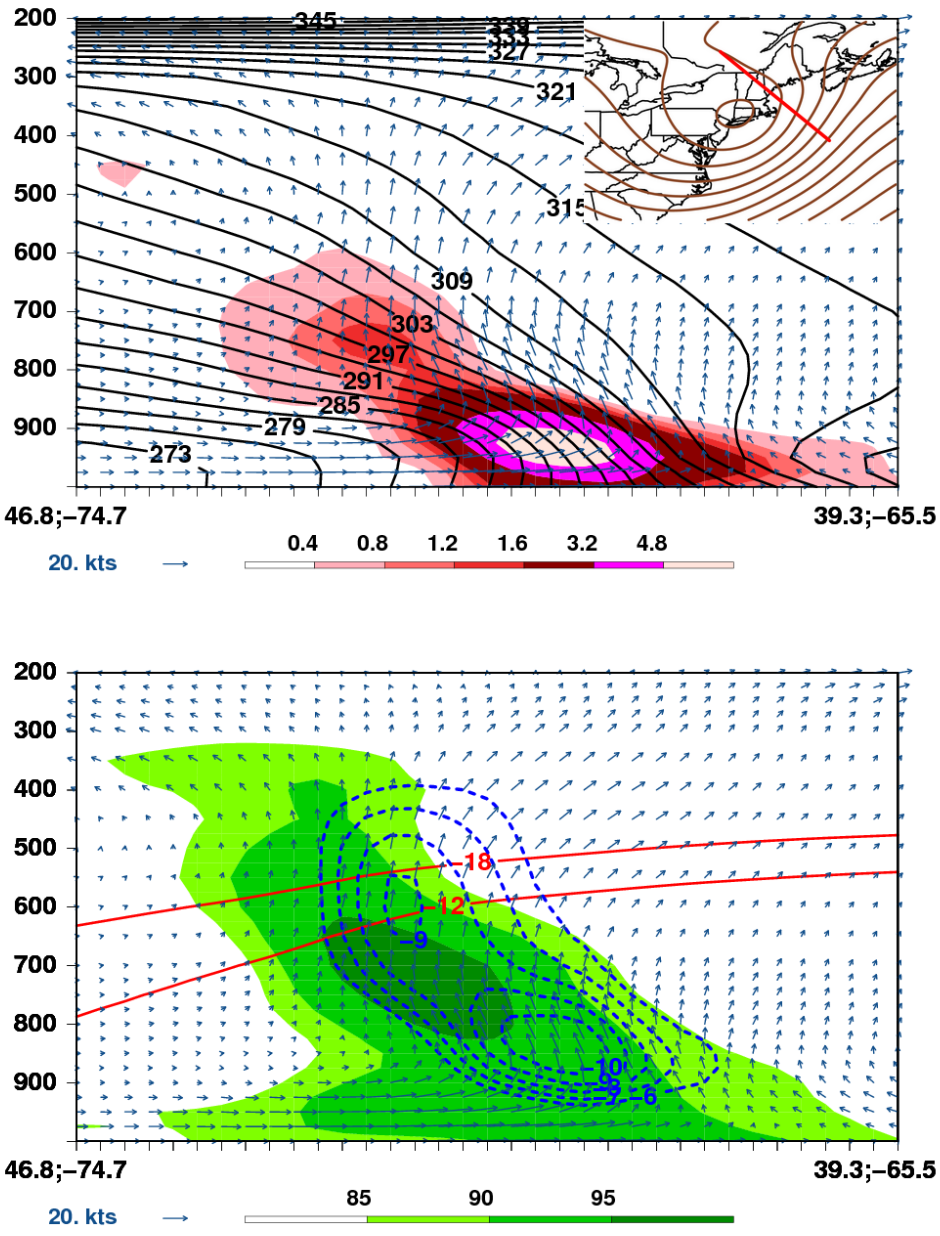

Figure 4.13: Northeast conceptual model vertical cross-section at t = +12 h: (top) saturation equivalent potential temperature (solid black, K), Petterssen frontogenesis (shaded, K (100 km)$^{-1}$ (3 h)$^{-1}$), and ageostrophic winds (arrows, kts); (bottom) omega (dashed blue, μb s^{-1}), relative humidity with respect to ice (shaded, >85%), dendritic growth zone from -12°C to -18°C (solid red, °C), and ageostrophic winds (arrows, kts). Inset Figure depicts the orientation of the vertical cross-section with 700-hPa heights (solid brown, m) for reference.

a broad axis of maximum θ_e associated with the WCB is located to the east of the surface low with a slight θ_e ridge extending to the northwest from the intersection of the 700-hPa cold and warm fronts. By t = +6 h, a well-defined TROWAL structure is evident to the east and north of the surface low (Fig. 4.14b) that extends to the deepening 700-hPa trough (not shown). Over the next 12 h, the TROWAL continues to become better defined as the WCB turns cyclonically to the north and west of the surface low (Figs. 4.14c and 4.14d). Cross sections oriented approximately 300-400 km east of their respectively surface lows and locally orthogonal to the θ_e axis (as in Posselt and Martin 2004), show the development of the TROWAL structure over a 12-h period. At t = 0 h, the cold front, warm front, and nose of the warm sector are clearly defined (Fig. 4.15, top). A broad, shallow frontogenesis maximum is located along the warm front, however, clear evidence of a TROWAL structure is not apparent. By t = +12 h, a sloping canyon of high θ_e air, characteristic of the TROWAL (e.g., Martin 1998a), is located above the intersection of the surface cold and warm fronts (Fig. 4.15, bottom). It can be hypothesized that the TROWAL airstream is at least partially responsible for strengthening the midlevel frontogenesis.

4.3.3 Potential Vorticity Analysis

Figure 4.16 shows the evolution of the upper-level positive PV anomaly associated with the NCM. The upper-level PV anomaly at t = 0 h is meridionally oriented and extends from a high-latitude PV reservoir across central Canada to a low-latitude PV anomaly. Upper-level PV advection is maximized on the eastern side of the PV anomaly across the Mid-Atlantic downwind of the upper-level trough axis and just west of the surface cyclone. Over the next 12 h,

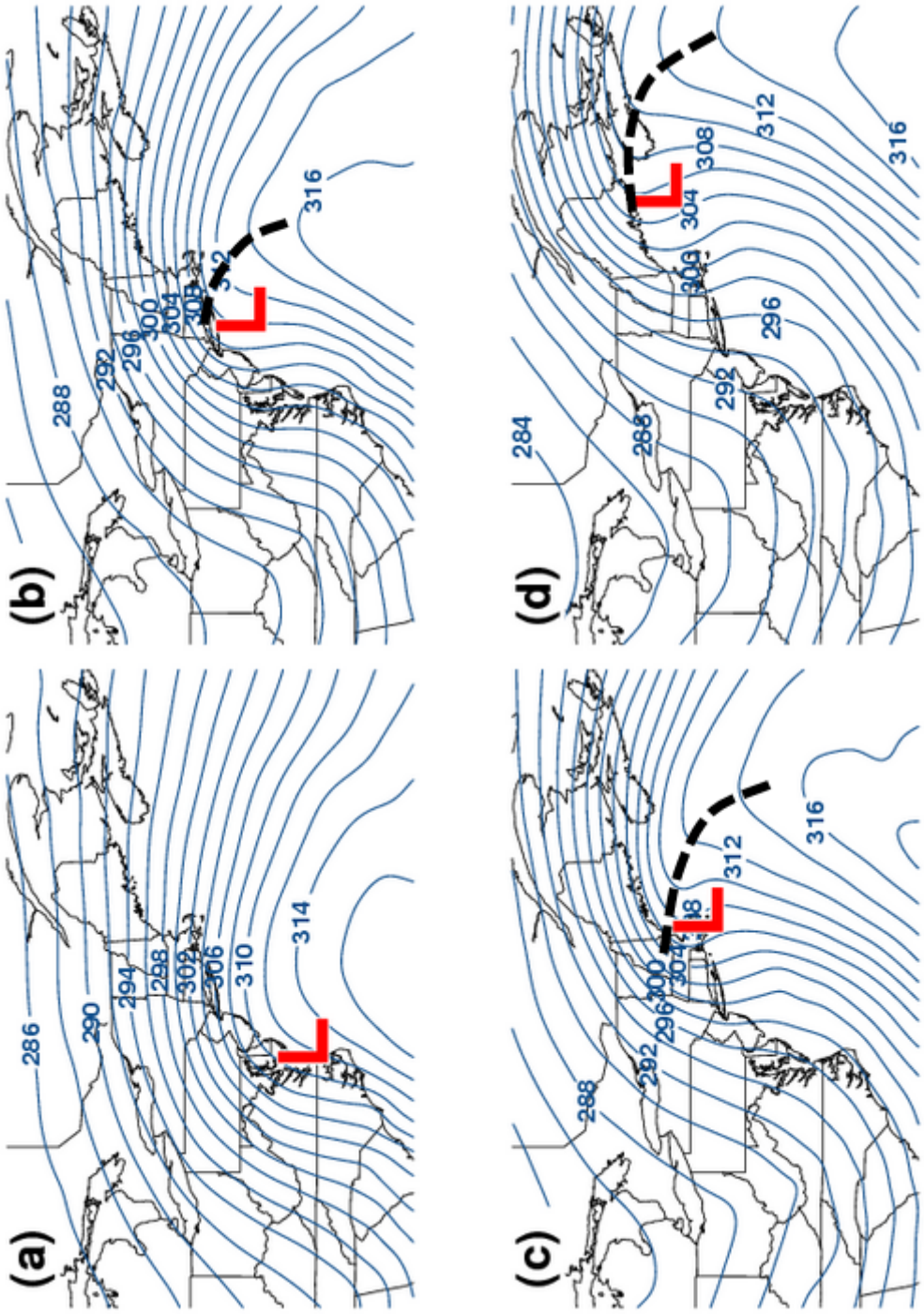

Figure 4.14: Northeast conceptual model 700-hPa equivalent potential temperature (solid blue, K) at: (a) t = 0 h; (b) t = +6 h; (c) t = +12 h; (d) t = +18 h. Thick dashed lines indicate the TROWAL position along the axis of maximum equivalent potential temperature.

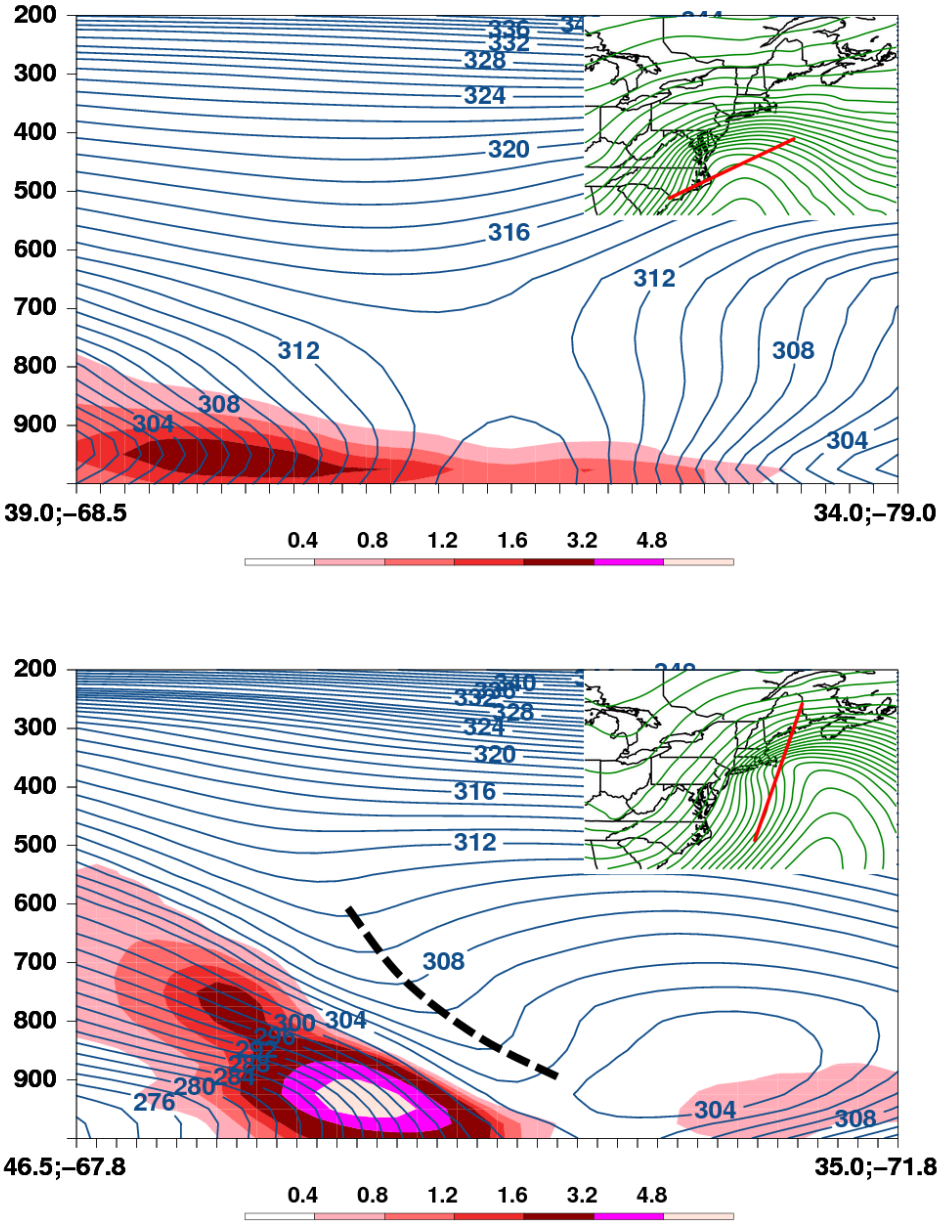

Figure 4.15: Northeast conceptual model vertical cross-section of equivalent potential temperature (solid blue, K) at: (top) t = 0 h; (bottom) t = +12 h. Inset Figure depicts the orientation of the vertical cross-section with 850-hPa equivalent potential temperature (solid green, K) for reference. Thick dashed line at t = +12 h indicates the TROWAL position along the axis of maximum equivalent potential temperature.

the PV anomaly cyclonically rotates into the "treble clef" shape found by Martin (1998a) where an axis of low PV (notch) is to the northwest of the PV anomaly (Figs. 4.16b,c). The upper-level PV advection maxima is located just downwind of the PV hook in a position to help strengthen the PV notch, and by t = +12 h the maxima is collocated with the surface cyclone (Figs. 4.16c).

Cross sections, oriented roughly west-east through the upper- and lower-level PV anomalies, as in Davis (1992) and Moore et al. (2008), are shown in Fig. 4.17. At t = 0 h, two PV anomalies are present in the NCM: an upper-level anomaly located over the Appalachian Mountains and a low-level anomaly associated with the surface cyclone near the border of Virgina and North Carolina (Fig. 4.17a,b). The low-level PV anomaly is located beneath the trough-ridge system and downwind of the upper-level PV anomaly to the northwest of a low-level potential temperature anomaly (Fig. 4.17a). Twelve hours later, the distance between the PV anomalies decrease which allows the cyclonic circulation associated with the upper-level PV anomaly to phase with the low-level anomaly (Fig. 4.17c,d). The interaction leads to a vertical expansion and increase in magnitude of the low-level PV anomaly, which in turn increases the potential temperature anomaly to the east of the strengthening surface cyclone shown in Fig. 4.17(c,d).

4.3.4 Summary

The four-dimensional NCM ETC (Figs. 4.5–4.9) has similar structure and features as previous heavy snow CMs in the literature (e.g., Bjerknes and Solberg 1923; Miller 1946; Palmen and Newton 1969; Uccellini and Kocin 1987; Kocin and Uccellini 1990; Nicosia and Grumm 1999; Banacos 2003; Novak et al. 2004, 2010).

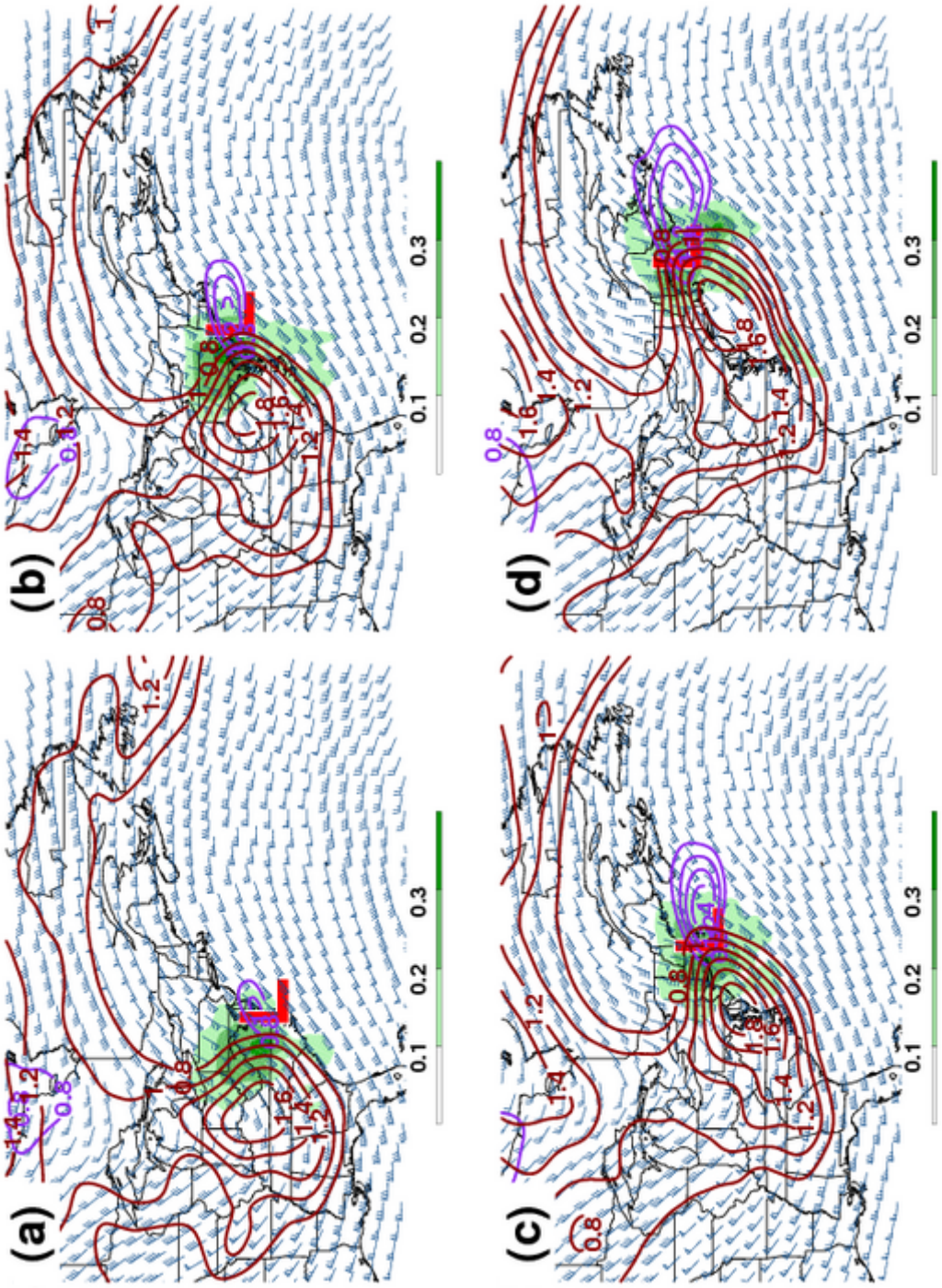

Figure 4.16: Northeast conceptual model 400-hPa PV (solid red; PVU), 975-hPa PV (solid purple; PVU), PV advection (shaded; PVU h^{-1}), and 400-hPa winds (barbs; kts) at: (a) t = 0 h; (b) t = +6 h; (c) t = +12 h; (d) t = +18 h. Surface low pressure centers are shown.

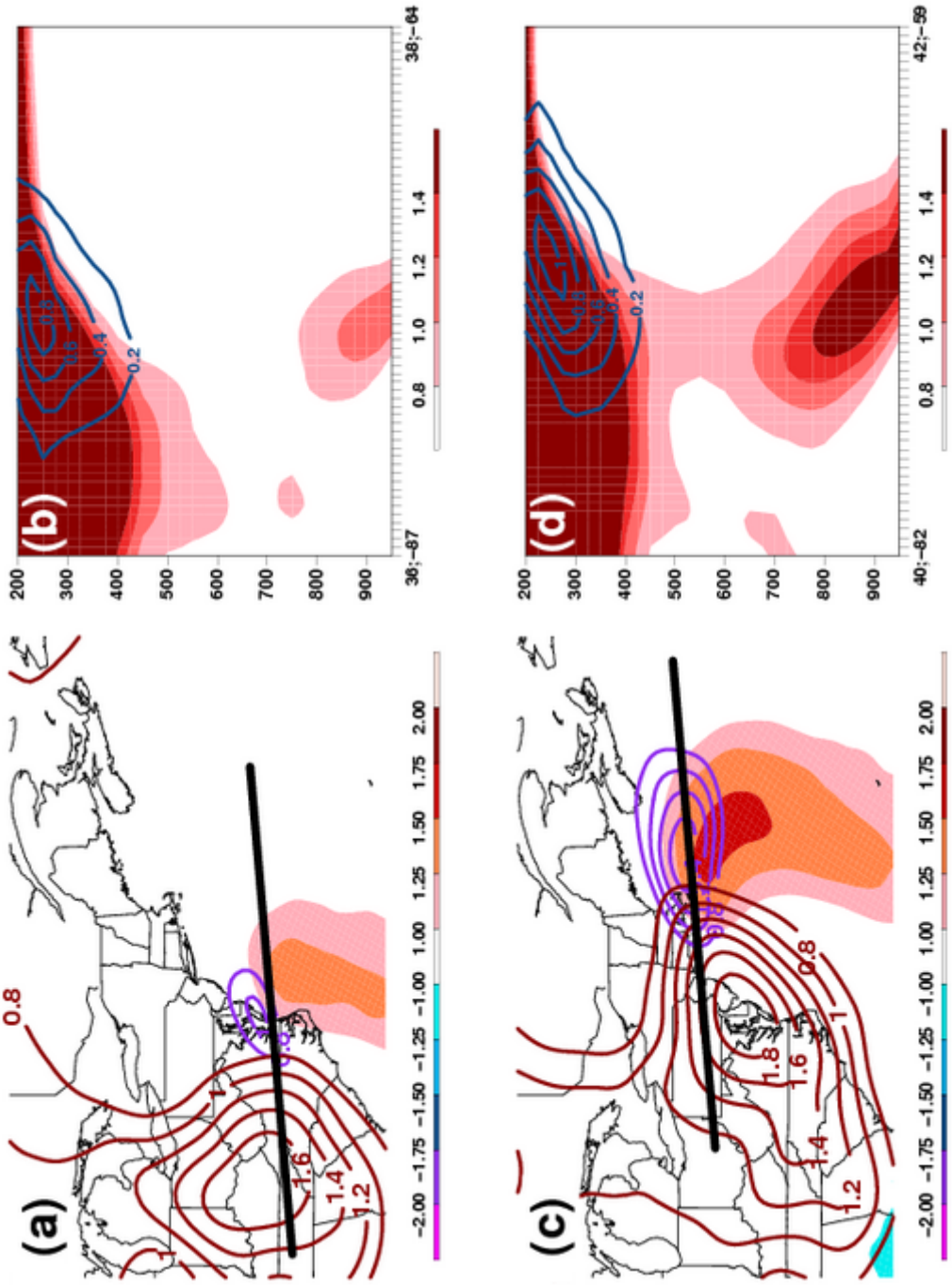

Figure 4.17: Northeast conceptual model at t = 0 h: (a) 400-hPa PV (solid red; PVU), 975-hPa PV (solid purple; PVU), and 2-m potential temperature standardized anomaly (shaded; σ); (b) vertical cross-section of PV (shaded; PVU) and PV advection (solid dk blue; PVU h^{-1}), and t = + 12h: (c) 400-hPa PV (solid red; PVU), 975-hPa PV (solid purple; PVU), and 2-m potential temperature standardized anomaly (shaded; σ); (d) vertical cross-section of PV (shaded; PVU) and PV advection (solid dk blue; PVU h^{-1}).

The NCM surface low circulation, cold and warm frontal positions, and warm sector resembles the ETC CM developed by Bjerknes and Solberg (1923) in Fig. 2.8. As the NCM surface low evolves between t = -6 h and t = + 18 h (Figs. 4.5a–4.9a), it occludes as the ETC life cycle CM does in Fig. 2.9. Harrold (1973), Carlson (1980), Danielsen (1964), and Moore et al. (2005) found that, through their analyses of the CCB, WCB, and DCB, the interaction of air streams determines precipitation intensity and type, moisture and thermal advections, and atmospheric stability within ETCs. The presence and juxtaposition of these air streams in the NCM are shown in Fig. 4.18 above the surface cyclone. As the NCM evolves, the conveyor belts are similar to the Moore et al. (2005) Fig. 2.14 (middle) at t = + 6 h and then to Fig. 2.14 (bottom) at t = + 18 h after the surface low became occluded. The self-development process (Sutcliffe and Forsdyke 1950; Palmen and Newton 1969) can be used as an approach to illustrate how the NCM strengthened. After the NCM surface cyclone developed (4.5a), low-level temperature advection increased which distorted the thermal field and upper-level flow pattern. As the amplitude of the upper-level wave increased (Figs. 4.6c–4.9c), an increase in vorticity advection and divergence occurred above the strengthening surface low. The positive feedback between the upper-level wave and surface low continued until the two became vertically aligned (not shown).

The vertical development of the NCM cyclone can also be described using PV fields as in Hoskins et al. (1985), Davis and Emanuel (1991), Davis (1992), Moore et al. (2008), and Brennan et al. (2008). The adapted CMs found in Brennan et al. (2008; their Figs. 2 and 3), illustrate the key features associated with a developing mid-latitude cyclone using PV framework: an upper-level cyclonic PV anomaly, a positive surface potential temperature anomaly, a

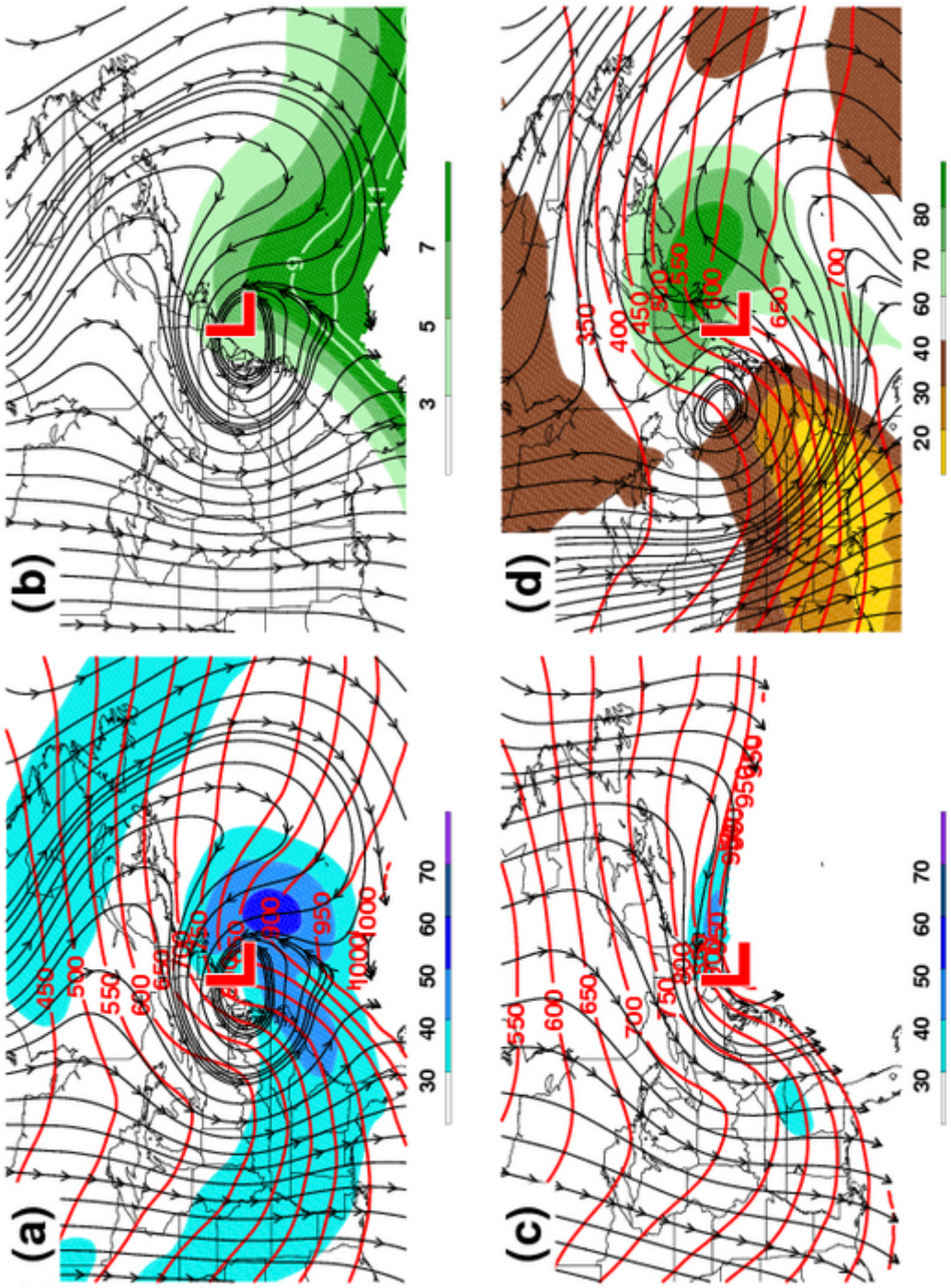

Figure 4.18: Northeast conceptual model at t = +6 h: (a) 294 K isentropic surface with system-relative streamlines (arrows), isobars (solid red, hPa), and isotachs (shaded, kts); (b) 294 K isentropic surface with system-relative streamlines (arrows) and mixing ratio (shaded; 10 $\times 10^{-3}$ g kg^{-1}); (c) 286 K isentropic surface with system-relative streamlines (arrows), isobars (solid red, hPa), and isotachs (shaded, kts); (d) 306 K isentropic surface with system-relative streamlines (arrows) and relative humidity (shaded, %). Surface low pressure centers are shown.

diabatically generated low-level cyclonic PV anomaly, and a diabatically generated upper-tropospheric anticyclonic PV anomaly. Figures 4.16 and 4.17a,c show these features with the NCM. Even though the flow associated with the PV anomalies is not explicitly shown, the presence of the features in the NCM implies that the circulations exist with the NCM members. The induced flow is important because coupling can occur between the upper-level cyclonic PV anomaly and the surface potential temperature anomaly, which can lead to a stronger feedback process and a more intense cyclone (Brennan et al. 2008). Cross sections through the PV anomalies suggest that between t = 0 h and t = +12 h (Fig. 4.17), the circulations were coupled as the PV tower develops as in Davis and Emanuel (1991), Davis (1992), and Moore et al. (2008).

CMs developed through investigating the mesoscale aspects of heavy snowfall (e.g., Martin 1998a, 1999; Nicosia and Grumm 1999; Novak et al. 2004; Posselt and Martin 2004; Moore et al. 2005; Novak et al. 2010), focus on the TROWAL and the interaction between stability and frontogenesis. An examination of the NCM's occluded structure (Figs. 4.14 and 4.15) revealed the development of a TROWAL as in Martin (1998a), Martin (1999), and Posselt and Martin (2004). Figure 4.14 illustrates how the NCM 700-hPa θ_e field evolved over 18 h. Similar to the case studies of Martin (1998a), Martin (1998b), Martin (1999), and Posselt and Martin (2004), the 700-hPa θ_e ridge becomes better defined and more removed from the warm sector as the cyclone continues to deepen. A vertical cross section through the NCM at t = +12 h (Fig. 4.15, bottom) showed the "three-dimensional sloping canyon" described by Martin (1998b) just above the surface occlusion. Furthermore, the placement and strength of the midlevel frontogenesis field, just poleward of the TROWAL, in Fig. 4.15 (bottom) is consistent to the results of Martin (1998a) and Martin (1998b). The analysis

suggests that the warm-occluded structure first appeared at midlevels, as in Martin (1998a), but due to member-to-member variability of the TROWAL location at t = 0 h and t = +6 h, some definition may be lost.

The low to midlevel frontogenesis associated with the NCM is similar to the climatological banded precipitation studies from Novak et al. (2004) and Novak et al. (2010). In Novak et al. (2004), utilizing the WSR-88D network, banded precipitation events were found for a five year period. The single-banded CM (Fig. 2.27) illustrates an area of frontogenesis that extends from ahead of the surface cyclone within warm advection to the northwest of the cyclone where the TROWAL would be located. The placement of the NCM 700-hPa frontogenesis field at t = +6 h (Fig. 4.11b) is similar to the results of Novak et al. (2004). In addition, cross-section analyses (Figs. 4.12 and 4.13) illustrate a comparable frontogenetical structure to the Novak et al. (2004) CM (their Fig. 16a). Both indicate a region of frontogenesis extends into midlevels that is embedded within weak conditional stability. This results in a narrow area of ascent that is equatorward of the frontal zone.

The evolution of the NCM 700-hPa frontogenesis field between t = 0 h and t = +18 h is similar to the PV hook CM of Novak et al. (2010) (Fig. 2.28). They found that during the six hours leading up to band formation, lower-tropospheric frontogenesis nearly doubles while a reduction in conditional stability above the frontal zone occurs (Figs. 4.11a,b). Frontogenesis continues to increase as the band reaches maturity and then decreases as it dissipates (Fig. 4.11c,d). Novak et al. (2010) state that the increase in frontogenesis occurs as changes in the kinematic flow occur through latent heat release and midlevel height falls. Upper-level PV advection along the northern portion of the hook, which can be responsible for the midlevel height falls, occurs in the Novak et al.

(2010) CM and in the NCM (Fig. 4.16b,c). The frontogenesis generally weakens as the flow is altered due to the development of a localized low-level PV anomaly to the east of the band (Novak et al. 2009). Even though weakening of the frontogenesis field occurs in the NCM between t = +12 h and t = + 18 h, the low-level (i.e., 925 hPa) diabatic PV anomaly signal is not present which is likely due to the spatial resolution of the NARR fields and/or the variability of the location of this feature. However, the similarities between the NCM and the CMs developed by Novak et al. (2004) and Novak et al. (2010) suggest that the NCM members are associated with banded snow events.

Chapter 5. Northeast Heavy Snow Near Misses

5.1 Determination of Potential Near Misses

To find Northeast heavy snow potential near misses, a collection of surface lows that did not include heavy snow was determined. For a surface low to be considered a potential near miss, the following criteria needed to be met:

- occur after 1 December 1980 and before 29 February 2008 during the months of December, January, and February.
- have at least 1 closed contour $\leq$ 1016 hPa.
- a coastal track that redeveloped south of 38°N, if redevelopment occurred.
- a coastal track that fell within the envelope of tracks with the NCM members.

In Fig. 5.1, the tracks of the 85 surface lows that met the above criteria are shown. The potential near-miss mean track begins over south-central North Carolina, continues over the Atlantic Ocean to 40°N and 70°W, and then northeast to the southeast of Nova Scotia. While the potential near-miss mean surface low track is more zonal than the mean NCM member track, the individual potential near-miss tracks are within the envelope of the NCM members. Similar to the methodology described in section 3.2.1 and implemented in section 4.2.2, field scores and total scores between the NCM and each potential near miss were computed when the potential near-miss surface low was in a location close to the NCM at t = +6 h. Each potential near-miss total score that exceeded the lowest

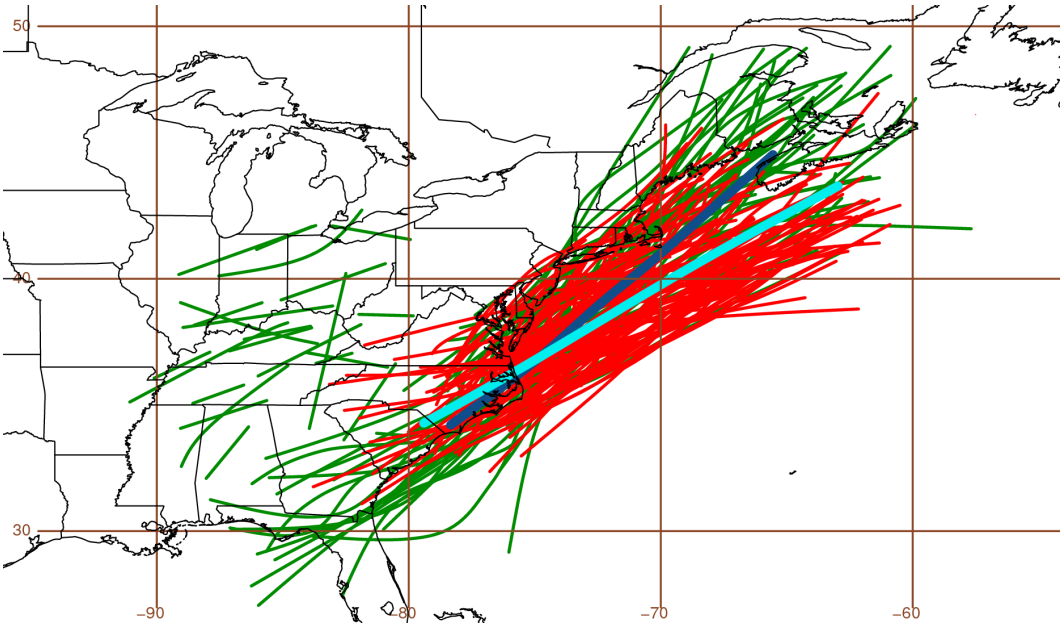

Figure 5.1: The 85 Northeast heavy snow potential near-miss coastal surface low tracks (red) and the 41 NCM member coastal surface low tracks (green) occurring during the months of December, January, and February between 1980 and 2008. The thick lines are the potential near miss (light blue) and NCM member (dark blue) average surface low tracks.

NCM member total score (10.291) was considered statistically similar to the NCM and a Northeast heavy snow near miss.

5.2 Analysis of Near-Miss Members

5.2.1 Overview

The twenty-five near misses that were identified as being similar to the NCM are listed in Table 5.1 and are associated with Northeast snow events of varying magnitudes. Organized snow events occurred with 16 of the near-miss members with maximum and median snow event anomalies of 0.95 and 0.65σ, respectively. The nine near-miss members without organized snowfall and the cluster of near-miss surface low tracks to the right of the mean near-miss track suggest that the development of these systems may have occurred too far off the

Table 5.1: The 25 Northeast heavy snow near-miss events identified by the NCM. Near-miss events are listed in ascending order of near-miss score.

Near miss rank	t = +6 h time	Near miss score	Anomaly rank	Anomaly (σ)
1	1200 UTC 5 Jan 1986	12.092	87	0.95
2	0600 UTC 8 Dec 1996	11.879	96	0.87
3	0600 UTC 5 Jan 1985	11.820	none	none
4	1800 UTC 6 Jan 2006	11.573	none	none
5	0000 UTC 7 Feb 1984	11.562	none	none
6	0000 UTC 9 Jan 2001	11.372	none	none
7	0600 UTC 31 Jan 2006	11.293	322	-0.42
8	1200 UTC 8 Feb 1981	11.268	93	0.90
9	1200 UTC 13 Jan 2002	11.208	199	0.19
10	1200 UTC 16 Dec 2005	11.184	101	0.83
11	0000 UTC 24 Jan 1983	11.108	none	none
12	0000 UTC 21 Jan 2001	10.952	91	0.91
13	1800 UTC 30 Dec 1986	10.938	none	none
14	1200 UTC 11 Dec 1987	10.851	none	none
15	1800 UTC 7 Feb 2003	10.849	95	0.87
16	1800 UTC 16 Dec 1980	10.845	115	0.71
17	0600 UTC 31 Dec 2007	10.845	147	0.50
18	0000 UTC 9 Jan 1990	10.836	347	-0.52
19	1200 UTC 16 Feb 1988	10.745	none	none
20	1200 UTC 5 Feb 1984	10.644	110	0.78
21	0600 UTC 1 Dec 1997	10.603	196	0.20
22	0600 UTC 2 Jan 2003	10.555	438	-1.14
23	1200 UTC 29 Dec 1987	10.535	135	0.60
24	0000 UTC 28 Dec 1997	10.519	292	-0.29
25	0600 UTC 30 Jan 1986	10.382	none	none

coast to affect the Northeast (Fig. 5.2). Over the 24-h period between t = -6 h and t = +18 h every near-miss member surface low deepened with an average 24-h pressure decrease and rate of 16.3 hPa and 4.5 hPa $(6\ \text{h})^{-1}$, respectively (Table 5.2). Even though the near miss surface cyclones deepened less than the NCM members, deepening rates exceeding -6 hPa $(6\ \text{h})^{-1}$ occurred with 9 near-miss members and -12 hPa $(12\ \text{h})^{-1}$ with 8 members.

Using the number of events that fall within each surface low category in Table 5.3, the climatological frequency of heavy snow events with coastal surface

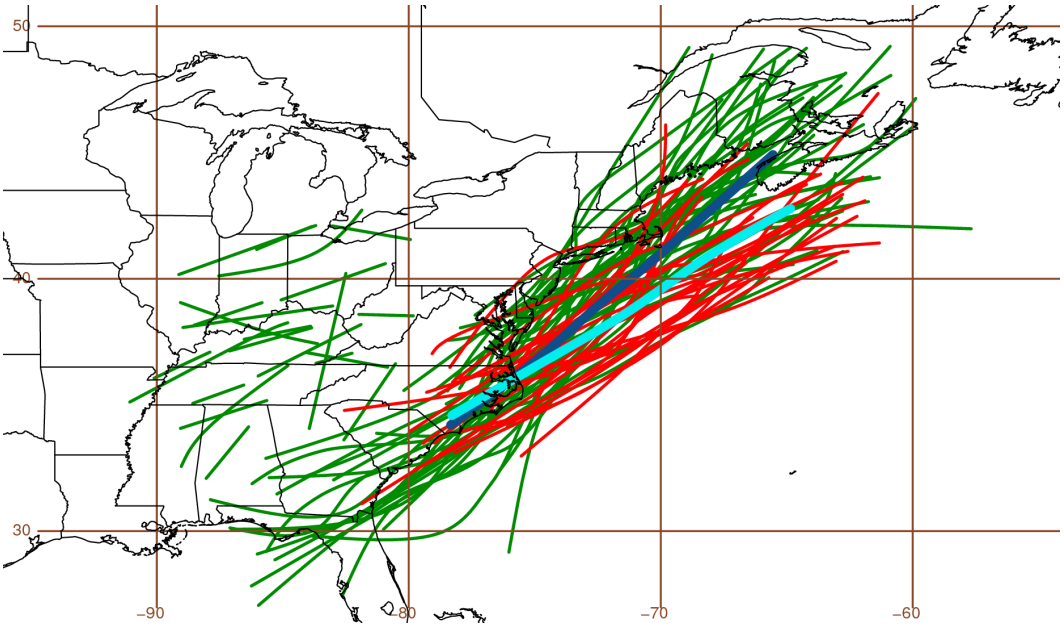

Figure 5.2: The 25 Northeast heavy snow near-miss coastal surface low tracks (red) and the 41 NCM member coastal surface low tracks (green) occurring during the months of December, January, and February between 1980 and 2008. The thick lines are the potential near miss (light blue) and NCM member (dark blue) average surface low tracks.

Table 5.2: Surface-low pressure summary statistics for the 25 Northeast heavy snow near-miss events.

	Surface low pressure at t = 0 h (hPa)	**Adjusted[1] 6-h surface low pressure tendency at t = 0 h (hPa)**	**24-h surface low pressure decrease (hPa)**	**Adjusted[1] 24-h surface low pressure decrease (hPa)**	**Avg 6-h surface low pressure tendency (hPa)**	**Avg Adjusted[1] 6-h surface low pressure tendency (hPa)**
Mean	1002.7	-2.6	-16.3	-11.3	-4.5	-2.9
Median	1004.0	-3.3	-14.7	-9.0	-4.0	-2.5
Std dev	4.7	2.3	8.2	7.5	2.5	2.4
75th pct	1001.3	-4.2	-19.1	-14.7	-5.5	-3.7
25th pct	1007.7	-0.5	-11.9	7.6	-3.0	-1.9

[1]The adjusted surface pressure tendency removes the climatological pressure decrease associated with the northward movement of the cyclone.

Table 5.3: The number of events that fall within each surface low track category.

Surface low category	No. of events
Coastal track surface lows	126
Northeast conceptual model members	41
Potential near misses	85
Near-miss composite members	25

lows can be determined. Roughly 1 in 3 (41 of 126) coastal surface lows that occurred during December, January, and February between 1980 and 2008 had heavy snowfall. The identification of the near-miss composite members allows a restricted climatological frequency to be determined. If the surface lows are restricted so they are similar to the NCM, the climatological frequency nearly doubles to 62% (41 of 66). Although this demonstrates the robustness of the NCM, it also motivates the investigation of the near-miss composite members by attempting to find distinguishing characteristics between them and the NCM. These results represent a climatological analysis of Northeast heavy snow events. However, it is important to remember that with only thirty years of data it is difficult to investigate climate trends and connections to climatological indices.

5.2.2 Statistical Analysis

Field and total score summary statistics at t = +6 h, computed by comparing the 25 near-miss members and the NCM on the full domains in Fig. 3.2, are listed in Table 5.4. Similar to the NCM member field score summary statistics in Table 4.5, measures of center statistics from mass fields decrease from 300-hPa to the surface, fields with large gradients were lower, and the 2-m temperature field was highest. In addition, the majority of fields have similar median values when

Table 5.4: Field and total score summary statistics for the 25 Northeast heavy snow near-miss events.

	300-hPa height	**500-hPa height**	**700-hPa height**	**850-hPa height**	**Sea-level pressure**	**300-hPa isotachs**
Mean	0.935	0.925	0.868	0.749	0.516	0.435
Median	0.941	0.932	0.878	0.751	0.494	0.461
Std dev	0.028	0.032	0.058	0.083	0.152	0.170
Maximum	0.970	0.961	0.964	0.916	0.751	0.683
Minimum	0.867	0.838	0.772	0.592	0.313	-0.055

	850-hPa isotachs	**500-hPa RH**	**700-hPa RH**	**925-hPa mixing ratio**	**PWTR**	**700-hPa θ_e**
Mean	0.519	0.239	0.207	0.820	0.778	0.756
Median	0.542	0.241	0.282	0.814	0.784	0.773
Std dev	0.114	0.249	0.177	0.059	0.059	0.077
Maximum	0.732	0.563	0.454	0.913	0.878	0.878
Minimum	0.215	-0.420	-0.078	0.709	0.635	0.524

	850-hPa θ_e	**850-hPa temp**	**2-m temp**	**700:850-hPa avg fgen**	**PV**	**Total score**
Mean	0.817	0.850	0.937	0.088	0.620	11.058
Median	0.813	0.858	0.940	0.078	0.628	10.938
Std dev	0.057	0.049	0.023	0.220	0.119	0.460
Maximum	0.909	0.928	0.971	0.487	0.806	12.092
Minimum	0.709	0.747	0.860	-0.353	0.341	10.382

the NCM members and near-miss members are compared. The largest median differences occur with the sea-level pressure (0.180), relative humidity (0.202 and 0.142), and frontogenesis (0.193) fields. Sea-level pressure median differences are supported by the near-miss members having weaker surface lows that deepen less (Table 5.2). Frontogenesis and relative humidity field score differences suggest less precipitation and weaker low-level flow that could be associated with weaker surface lows. However, at least on the full mesoscale domain, the low-level height median differences between the near-miss members and NCM members were not large.

To ensure the similarities and differences from the full-domain field statistics

between the near-miss members and the NCM are representative, median statistics were also computed after dividing the full domains into quadrants (i.e., northwest, northeast, southeast, southwest) and are listed in Table 5.5. For mass fields, the northwest quadrant has the lowest median values and all but the sea-level pressure field medians are statistically significant at the 99% confidence level as determined by a Mann-Whitney non-parametric test using a two-sided Student's *t* distribution when compared to the medians of the other quadrant domains. In addition, the near-miss member northwest quadrant 850-hPa height and sea-level pressure field scores are statistically significant at the 99% confidence level when compared to the northwest quadrant NCM member field scores (not shown). Since the WCB, the TROWAL, and deformation can be directly linked to flow and precipitation within the northwest portion of mid-latitude cyclones, these results suggest the importance the northwest quadrant of the NCM has on the development of heavy snowfall across the Northeast.

The near-miss member median field score values for temperature and moisture were lowest in the southeast quadrant domain and the 925-hPa mixing ratio, precipitable water, and 700- and 850-hPa equivalent potential temperature field scores were statistically significant at the 99% confidence level when compared to the other quadrant domains. However, when comparing the temperature and moisture southeast domain field scores to the NCM members field scores none were statistically significant at the 99% confidence level and only the 2-m temperature field score was significant at the 95% confidence level. These results suggest that temperature and moisture fields within the warm sector have more variability than in the other quadrants. Furthermore, the significant difference between the NCM and near-miss member 2-m temperature

Table 5.5: Field and total score median statistics computed on the full, northwest, northeast, southeast, and southwest domains for the 25 Northeast heavy snow near-miss events. Statistics in red are the lowest median value for each field score over the subdomains and those with an asterisks indicate statistical significance at the 99% confidence level as determined by a Mann-Whitney non-parametric test using a two-sided Student's t distribution when compared to the other quadrants.

	300-hPa height	**500-hPa height**	**700-hPa height**	**850-hPa height**	**Sea-level pressure**	**300-hPa isotachs**
Median Full	0.941	0.932	0.878	0.751	0.494	0.461
Median NW	**0.840***	**0.781***	**0.170***	**0.110***	**0.549**	0.384
Median NE	0.954	0.942	0.865	0.669	0.687	0.333
Median SE	0.965	0.959	0.915	0.836	0.782	0.684
Median SW	0.917	0.912	0.886	0.801	0.674	**0.071**

	850-hPa isotachs	**500-hPa RH**	**700-hPa RH**	**925-hPa mixing ratio**	**PWTR**	**700-hPa θ_e**
Median Full	0.542	0.241	0.282	0.814	0.784	0.773
Median NW	**-0.070***	0.192	**0.069**	0.826	0.872	0.816
Median NE	0.388	0.334	0.438	0.818	0.849	0.781
Median SE	0.612	0.172	0.272	**0.584***	**0.351***	**0.412***
Median SW	0.549	**0.011**	0.107	0.820	0.779	0.720

	850-hPa θ_e	**850-hPa temp**	**2-m temp**	**700:850-hPa avg fgen**	**PV**	**Total score**
Median Full	0.813	0.858	0.940	0.078	0.628	10.938
Median NW	0.830	0.810	0.880	-0.034	**0.239***	**7.806***
Median NE	0.805	0.854	0.934	0.083	0.734	11.303
Median SE	**0.602***	**0.780**	**0.769**	0.042	0.544	10.128
Median SW	0.781	0.811	0.922	**-0.203**	0.452	9.537

field scores highlight the importance of the low-level temperature anomalies discussed in section 4.3.4.

5.3 Analysis of Near-Miss Composite

5.3.1 Synoptic-Scale Analysis

The near-miss composite surface low is located near the border of North and South Carolina (Fig. 5.3a), and is associated with a broad neutrally-tilted

midlevel trough (Fig. 5.3c) at t = -6 h. A weak surface anticyclonic circulation is located well offshore from the surface low and the presence of an anticyclone across the Northeast is not visible (Fig. 5.3a). At 850 hPa, a broad, open cyclonic circulation and a southwest-northeast oriented 30-kt LLJ is located over the Mid-Atlantic (Fig. 5.3b). Aloft, a 300-hPa 110-kt upper-level jet streak just east of Maine is embedded within broad southwesterly flow that extends from the Gulf Coast to southeastern Canada (Fig. 5.3d).

At the initial analysis time, the near-miss composite surface low has deepened approximately 2 hPa as it moved northeastward along the East Coast. However, the amplitude of the low- and upper-level pattern has merely translated (Fig. 5.4). During the next 6 h, the surface low deepened to 1000 hPa and a 850-hPa circulation began to develop (Fig. 5.5a,b). The LLJ has strengthened to between 40 and 50 kts and is aligned from southwest to northeast beneath the right-entrance region of a 300-hPa jet streak (Fig. 5.5b,d). Low-level mixing ratio and temperature fields in Fig. 5.6 show broad moisture and thermal ridges extending into the near-miss composite cyclone center. Although the flow along the ridge axes implies excellent moisture transport and warm air advection, the broad extent of the moisture reservoir and warm sector implies that the transport and advection is unfocused. At t = +6 h, the near-miss composite pattern is similar to the nonbanded conceptual model in Novak et al. (2004) where a weak surface low and midlevel trough are located within the entrance region of an upper-level jet streak.

During the next 12 h, the near-miss composite surface low deepened to 992 hPa and the 850-hPa circulation became better defined (Figs. 5.7a,b). The modest strengthening of the composite surface low could be attributed to the interaction of upper-level jet streaks shown in Fig. 5.7d. Although low-level mass

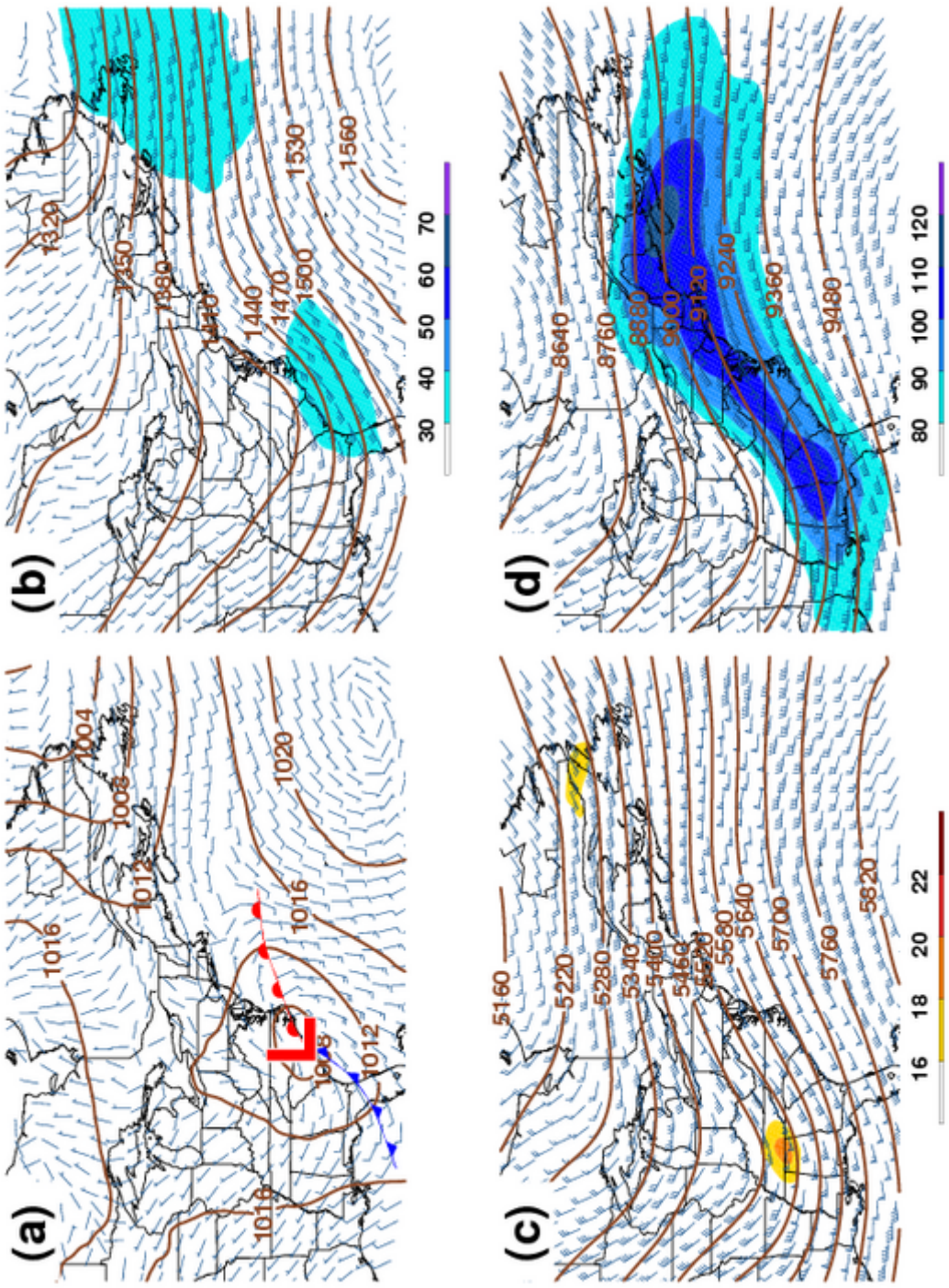

Figure 5.3: Near-miss composite at t = -6 h: (a) sea level pressure (solid brown; hPa) and 10-m wind (barbs; kts); (b) 850-hPa geopotential height (solid brown; m), wind speed (shaded; kts), and winds (barbs; kts); (c) 500-hPa geopotential height (solid brown; m), absolute vorticity (shaded; 10 $\times 10^{-5}$ s^{-1}), and winds (barbs; kts); (d) 300-hPa geopotential height (solid brown; m), wind speed (shaded; kts), and winds (barbs; kts). Surface low pressure center and fronts are shown in (a).

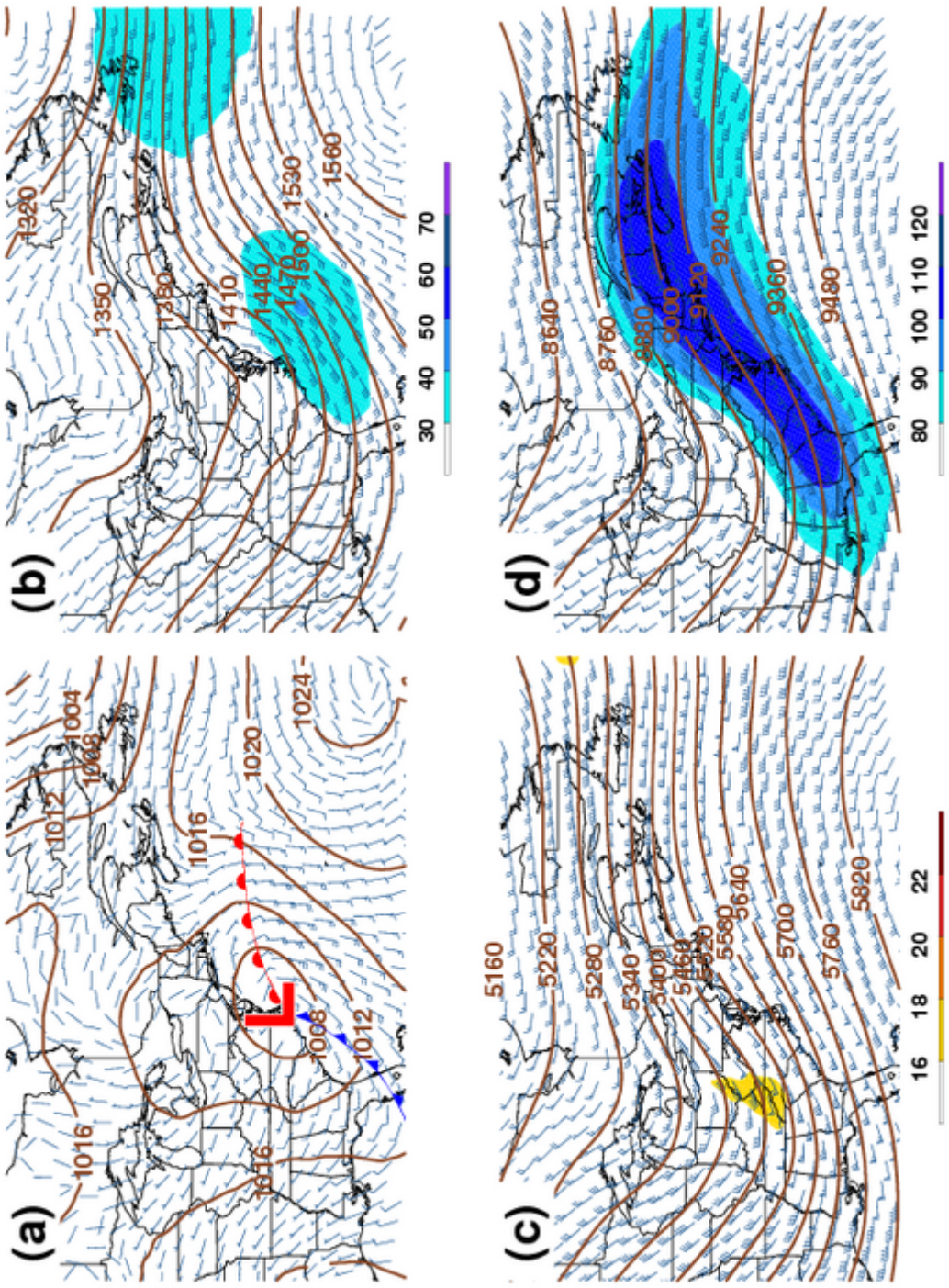

Figure 5.4: Near-miss composite at t = 0 h: (a) sea level pressure (solid brown; hPa) and 10-m wind (barbs; kts); (b) 850-hPa geopotential height (solid brown; m), wind speed (shaded; kts), and winds (barbs; kts); (c) 500-hPa geopotential height (solid brown; m), absolute vorticity (shaded; 10 $\times 10^{-5}$ s^{-1}), and winds (barbs; kts); (d) 300-hPa geopotential height (solid brown; m), wind speed (shaded; kts), and winds (barbs; kts). Surface low pressure center and fronts are shown in (a).

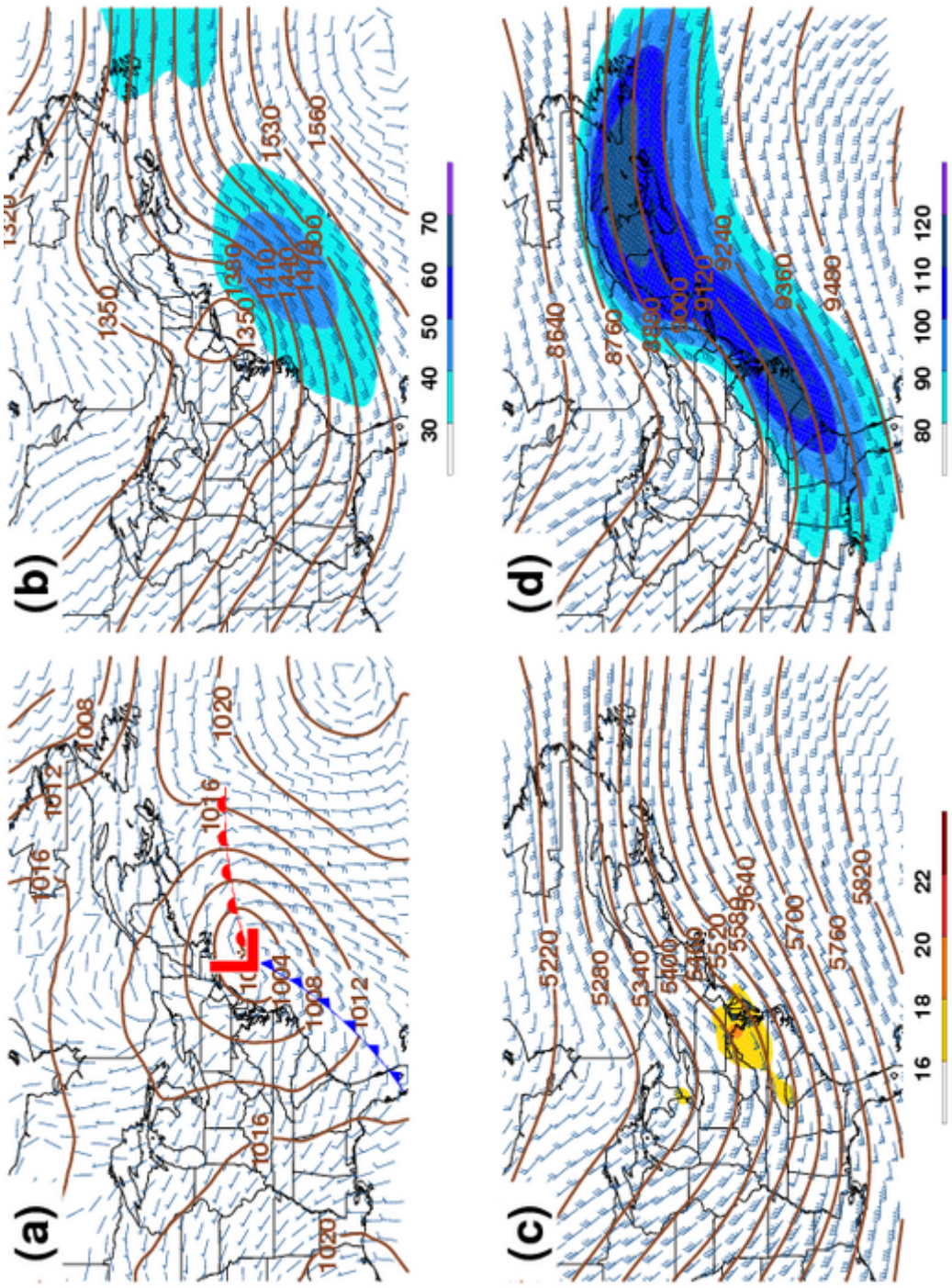

Figure 5.5: Near-miss composite at t = +6 h: (a) sea level pressure (solid brown; hPa) and 10-m wind (barbs; kts); (b) 850-hPa geopotential height (solid brown; m), wind speed (shaded; kts), and winds (barbs; kts); (c) 500-hPa geopotential height (solid brown; m), absolute vorticity (shaded; 10 $\times 10^{-5}$ s^{-1}), and winds (barbs; kts); (d) 300-hPa geopotential height (solid brown; m), wind speed (shaded; kts), and winds (barbs; kts). Surface low pressure center and fronts are shown in (a).

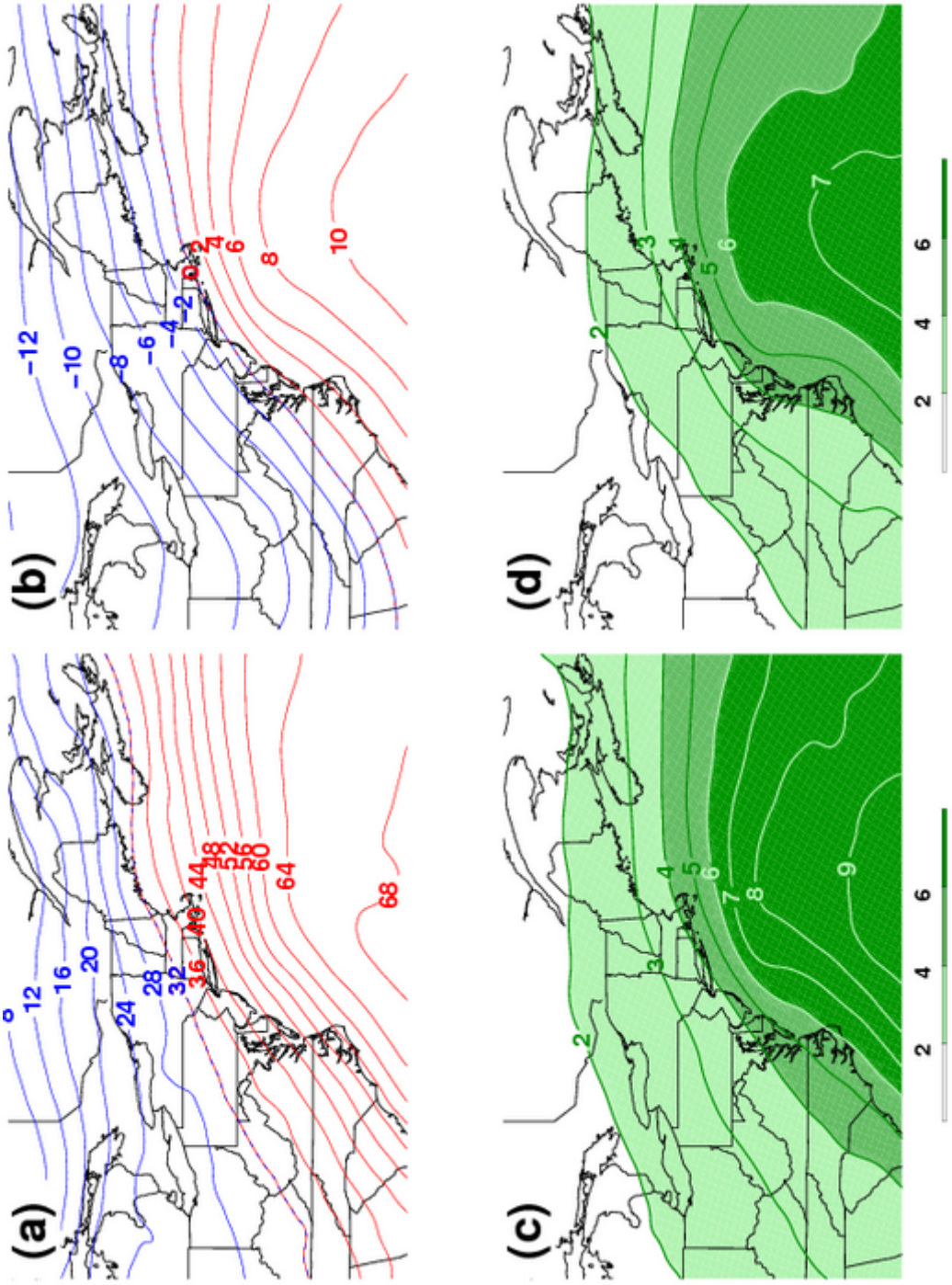

Figure 5.6: Near-miss composite at t = +6 h: (a) 2-m temperature (solid; °F); (b) 850-hPa temperature (solid; °C); (c) 925-hPa mixing ratio (shaded; 10 $\times 10^{-3}$ g kg^{-1}); (d) 850-hPa mixing ratio (shaded; 10 $\times 10^{-3}$ g kg^{-1}).

fields were stronger, the LLJ did not turn cyclonically to the north in the location of the TROWAL. Instead, the low-level wind max continued to exhibit a southwest-northeast orientation and was embedded within confluent flow. Furthermore, strengthening of the near-miss composite aloft was minimal as the 500- and 300-hPa heights are similar in magnitude as they were at t = +6 h (Figs. 5.7c,d).

The four-dimensional near-miss composite ETC is similar to the "moderate" snowstorms analyzed in Kocin and Uccellini (2005). They found differences involving cyclogenesis as being the major factor between these snowstorms and "major" snowstorms. As in the near-miss members, Kocin and Uccellini (2005) found that the surface lows were weaker, developed less intensity, and did not exhibit rapid deepening. Moderate snowstorms were also associated with small amplitude midlevel troughs that did not undergo a reduction in the trough-ridge half-wavelength or develop into closed systems. This upper-level flow evolution is similar to what was found in Figs. 5.3–5.7 and supports weaker surface cyclone development as listed in Table 5.2 and the mean zonal surface low track as shown in Fig. 5.2.

5.3.2 Mesoscale Analysis

At the initial analysis time, the near-miss composite has weak and unorganized 850- and 700-hPa frontogenesis oriented southwest-northeast just downwind of their respective trough axes (Figs. 5.8a and 5.9a). The areas of frontogenesis are embedded within confluent flow and are driven by shear deformation and broad warm-air advection. By t = +6 h, both frontogenetical axes strengthen and become better organized across southern New England. At

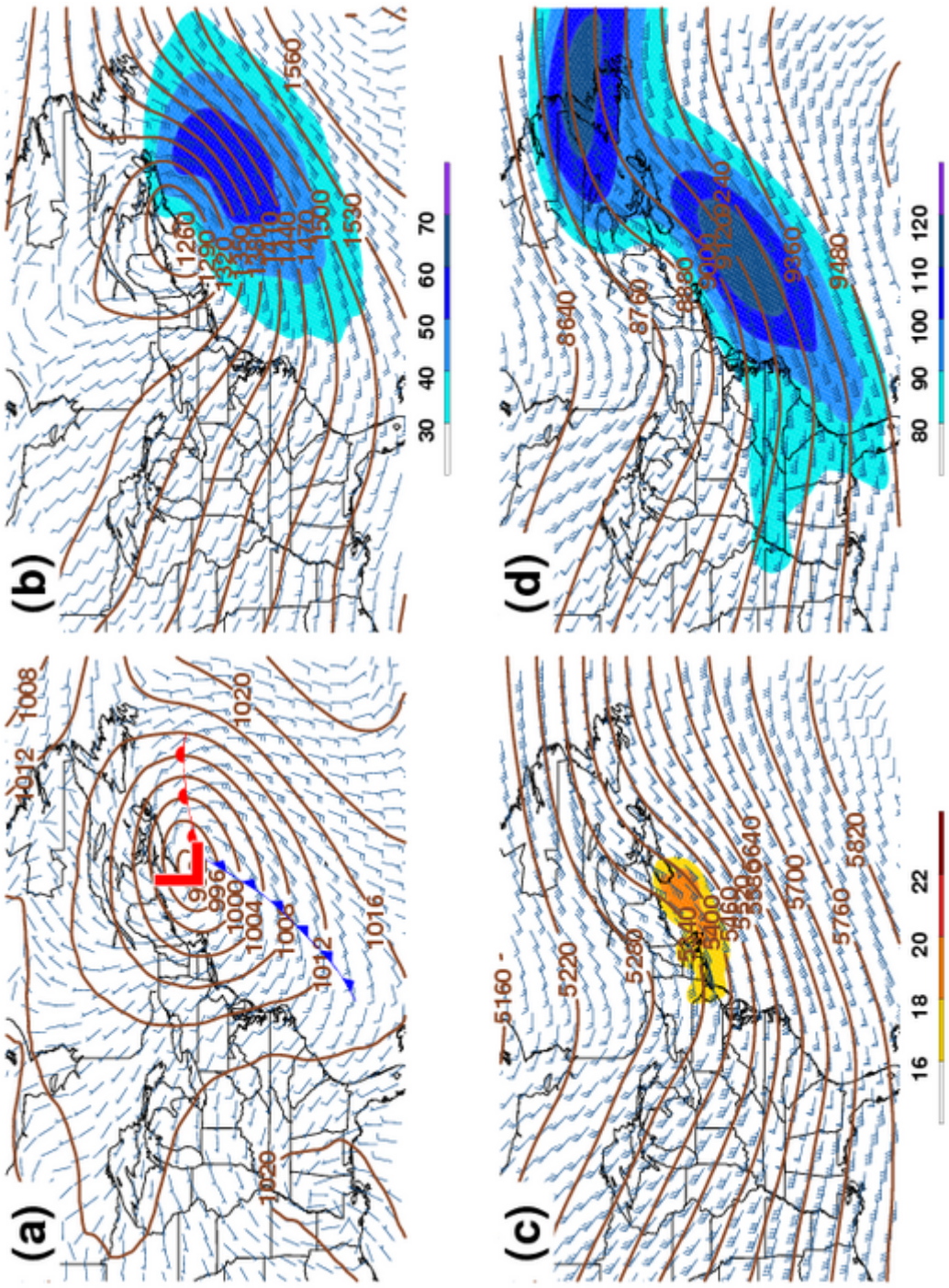

Figure 5.7: Near-miss composite at t = +18 h: (a) sea level pressure (solid brown; hPa) and 10-m wind (barbs; kts); (b) 850-hPa geopotential height (solid brown; m), wind speed (shaded; kts), and winds (barbs; kts); (c) 500-hPa geopotential height (solid brown; m), absolute vorticity (shaded; 10 $\times 10^{-5}$ s^{-1}), and winds (barbs; kts); (d) 300-hPa geopotential height (solid brown; m), wind speed (shaded; kts), and winds (barbs; kts). Surface low pressure center and fronts are shown in (a).

850 hPa, the strengthening is likely due to an increase in the low-level wind maximum (Fig. 5.5b) and speed convergence where the frontogenesis values more than doubles (Fig. 5.8b). Although the 850-hPa low deepens slightly over the next 12 h, at t = +18 h, the 700-hPa circulation remains open despite a strong frontogenetical signal just northeast of the trough axis. This would reduce the possibility of significant deformation and frontogenesis to the northwest of the surface cyclone (Novak et al. 2004).

Cross-section analysis of the near-miss composite at t = 0 h, oriented in a similar fashion to the cross sections in Figs. 4.12 and 4.13, is shown in Fig. 5.10. A broad, direct thermal circulation is associated with the northwest-sloping frontogenetical axis below a region of reduced stability. At this time, saturated ascent is relatively weak and unfocused, with magnitudes less than -7×10^{-1} μb s^{-1} (Fig. 5.10, bottom). At t = +12 h, the midlevel frontogenesis has increased along the equatorward side of the steep warm frontal zone (Fig. 5.11, top). Values within the 850–700-hPa layer along the band axis have nearly tripled as the direct thermal circulation and low-level northerly component of the ageostrophic wind have strengthened and increased. The changes within the frontal zone are evident as deep, sloping, saturated ascent is now present along the coast of southern Maine (Fig. 5.11, bottom).

The near-miss composite 700-hPa θ_e analysis t = 0 h depicts a broad θ_e axis within the warm sector (Fig. 5.12a). Six hours later, the 700-hPa θ_e ridge remains broad to the east and northeast of the surface low (Fig. 5.12b) and does not extend eastward until t = +12 h. This is evident in the cross section shown in Fig. 5.13 (bottom), where a TROWAL is located equatorward of the warm-frontal zone and within the 550–750-hPa layer. Although the TROWAL structure is present in the near-miss composite, its vertical extent is confined to the

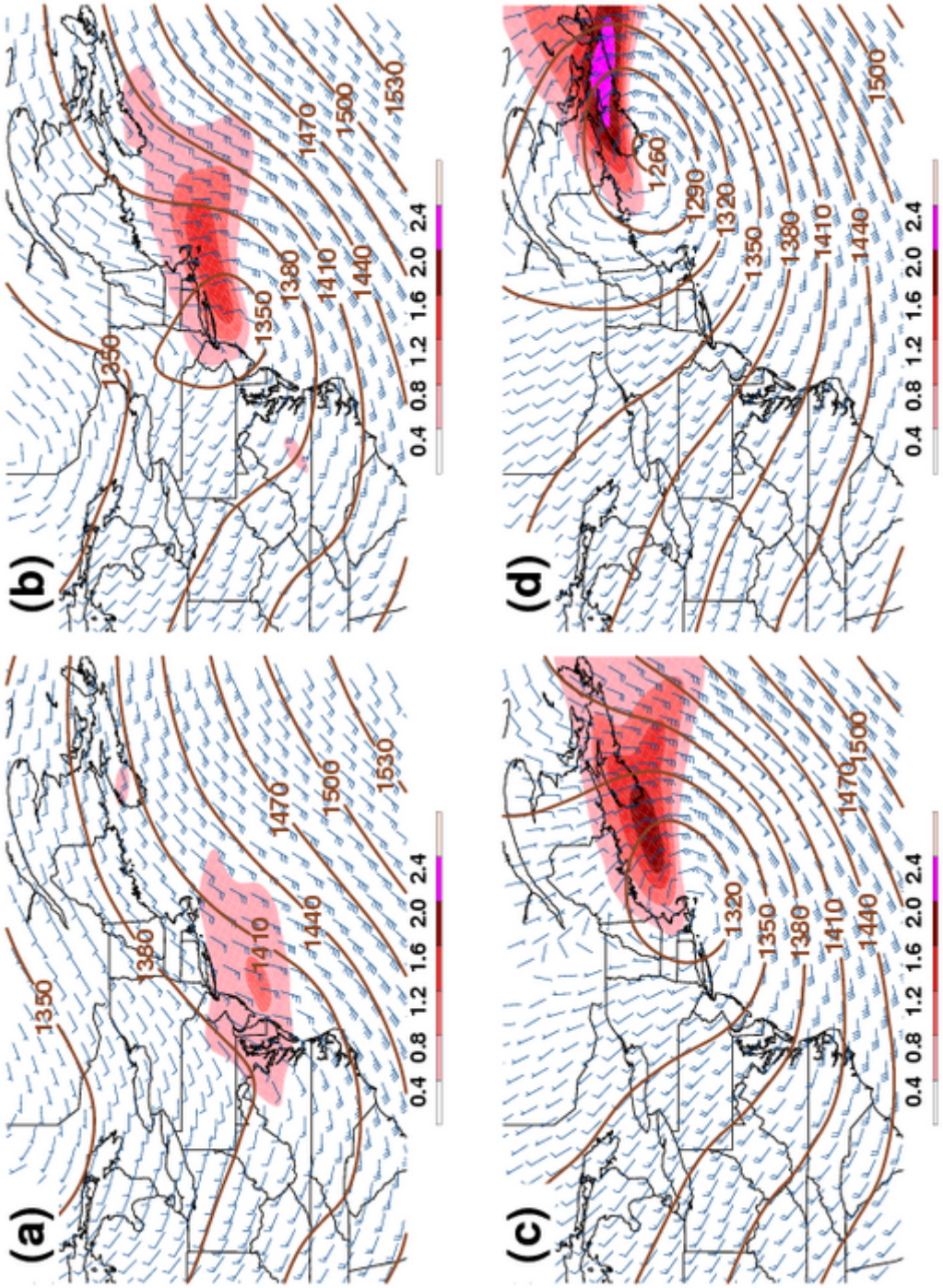

Figure 5.8: Near-miss composite 850-hPa geopotential height (solid brown; m) and Petterssen frontogenesis (shaded, K (100 km)$^{-1}$ (3 h)$^{-1}$) at: (a) t = 0 h; (b) t = +6 h; (c) t = +12 h; (d) t = +18 h.

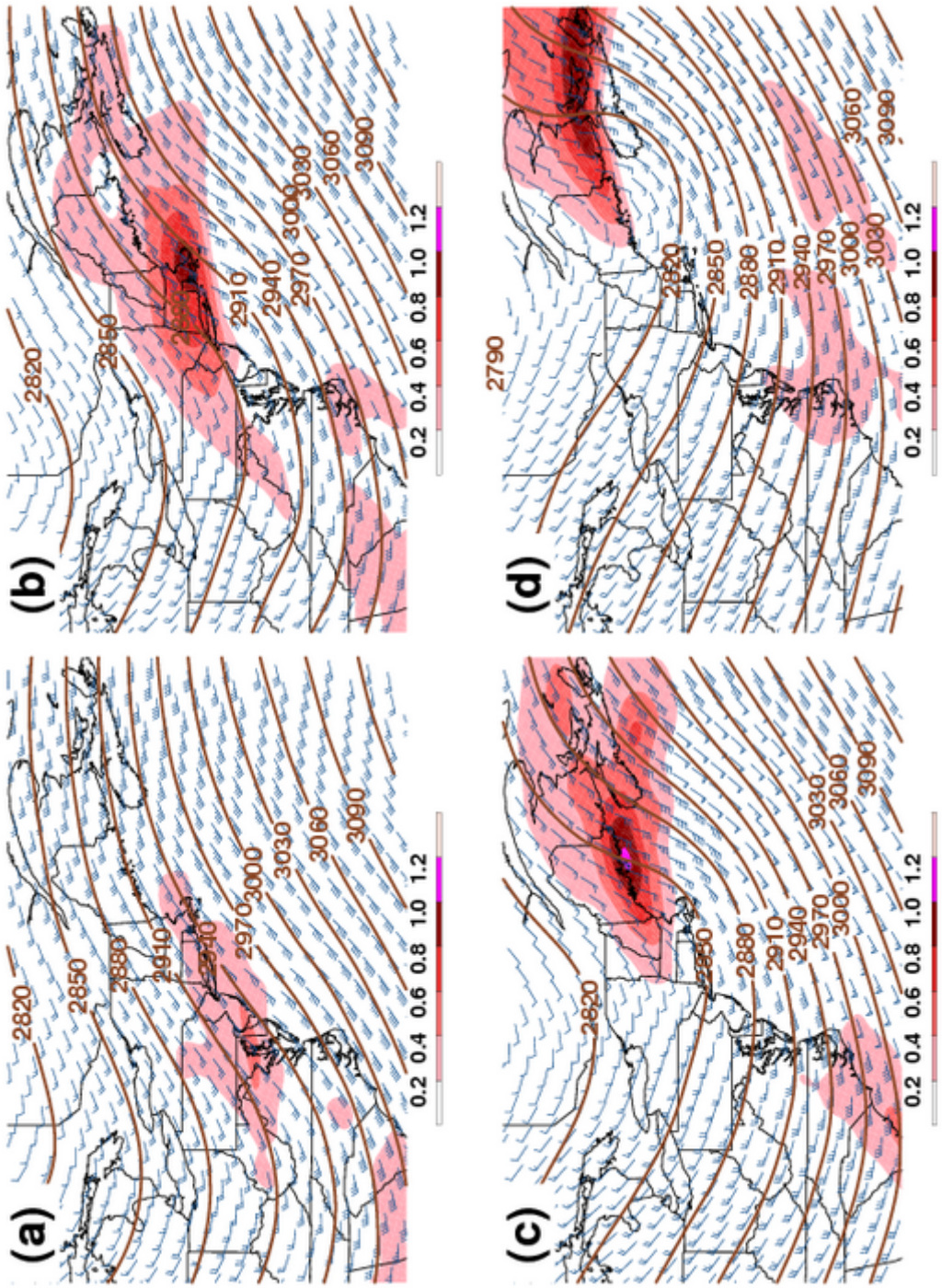

Figure 5.9: Near-miss composite 700-hPa geopotential height (solid brown; m) and Petterssen frontogenesis (shaded, K (100 km)$^{-1}$ (3 h)$^{-1}$) at: (a) t = 0 h; (b) t = +6 h; (c) t = +12 h; (d) t = +18 h.

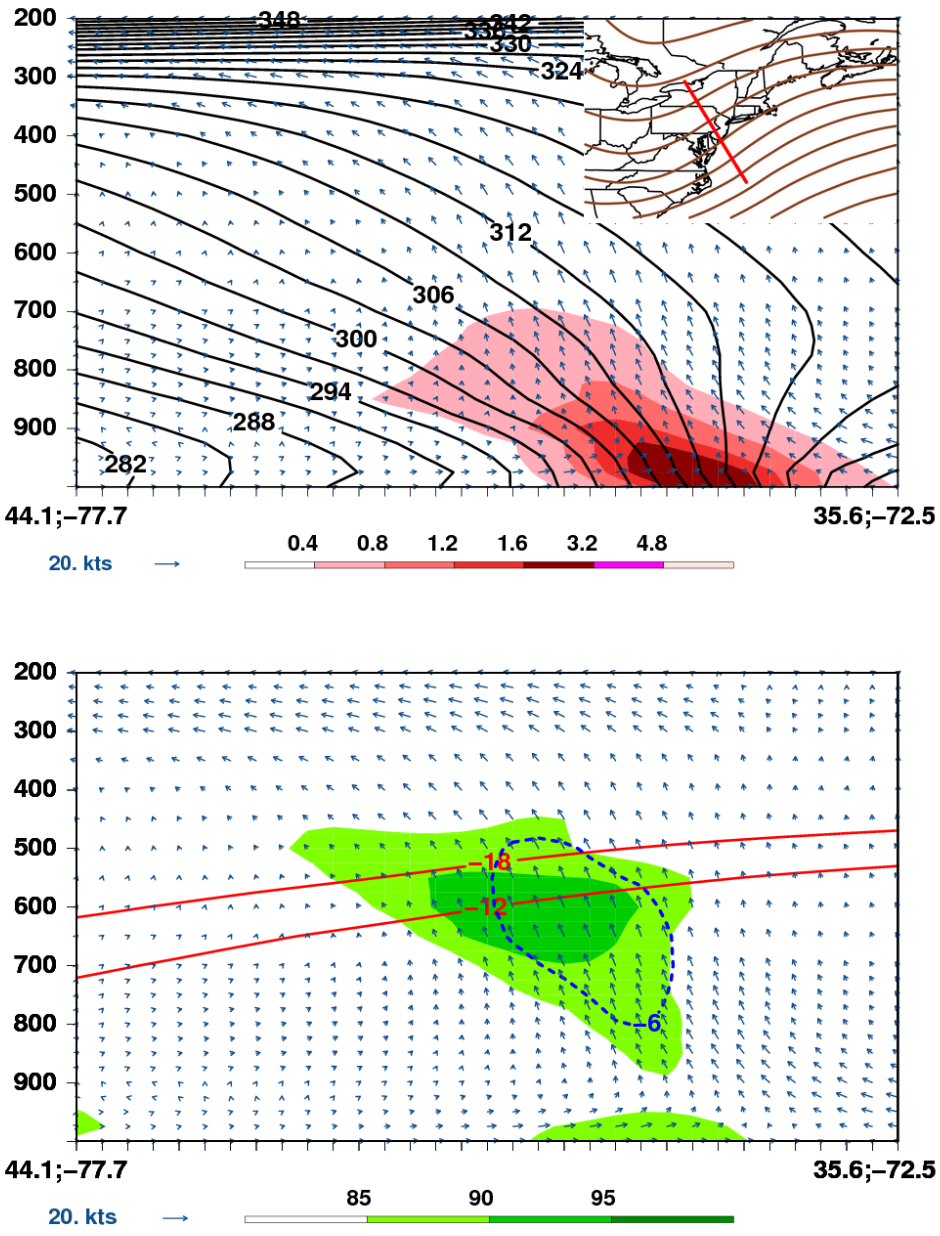

Figure 5.10: Near-miss composite vertical cross-section at t = 0 h: (top) saturation equivalent potential temperature (solid black, K), Petterssen frontogenesis (shaded, K (100 km)$^{-1}$ (3 h)$^{-1}$), and ageostrophic winds (arrows, kts); (bottom) omega (dashed blue, μb s^{-1}), relative humidity with respect to ice (shaded, >85%), dendritic growth zone from -12°C to -18°C (solid red, °C), and ageostrophic winds (arrows, kts). Inset Figure depicts the orientation of the vertical cross-section with 700-hPa heights (solid brown, m) for reference.

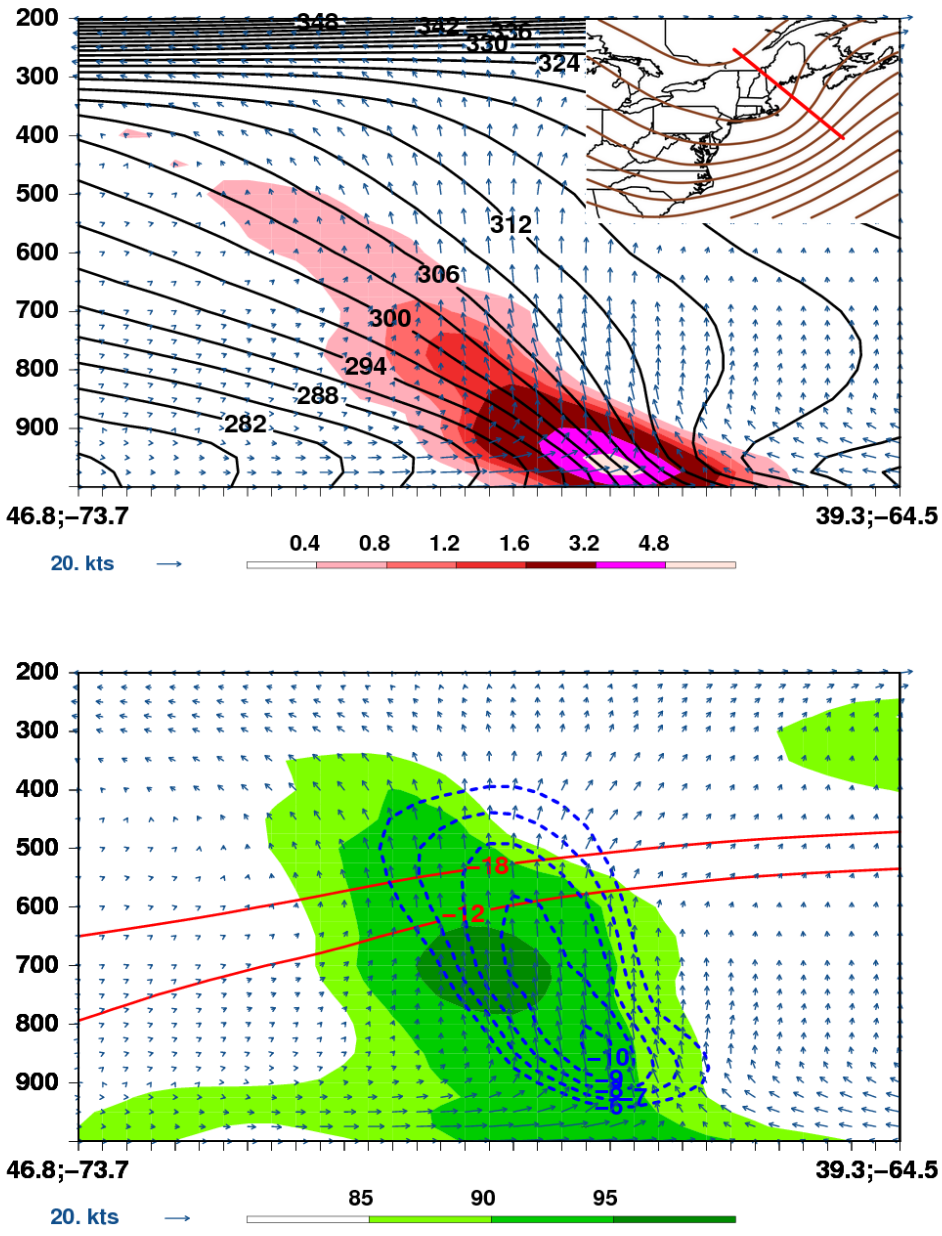

Figure 5.11: Near-miss composite vertical cross-section at t = +12 h: (top) saturation equivalent potential temperature (solid black, K), Petterssen frontogenesis (shaded, K (100 km)$^{-1}$ (3 h)$^{-1}$), and ageostrophic winds (arrows, kts); (bottom) omega (dashed blue, μb s^{-1}), relative humidity with respect to ice (shaded, >85%), dendritic growth zone from -12°C to -18°C (solid red, °C), and ageostrophic winds (arrows, kts). Inset Figure depicts the orientation of the vertical cross-section with 700-hPa heights (solid brown, m) for reference.

midlevels, which may affect the reduction of static stability adjacent to the frontal zone. Furthermore, the weaker cyclonic branch of the near-miss composite has an impact on the lack of westward extension of the 700-hPa θ_e ridge (Figs. 5.12c,d). This suggests more stability, weaker frontogenesis, and less moisture northwest of the surface cyclone where heavy snowfall would occur.

5.3.3 Potential Vorticity Analysis

The evolution of the near-miss composite upper-level positive PV anomaly is shown in Fig. 5.14. At t = 0 h, an unorganized low-latitude PV anomaly is oriented north-south just west of the Appalachian Mountains (Fig. 5.14a). PV advection associated with this feature is broad and unfocused and extends along the eastern side of the anomaly. Six hours later, even though upper-level PV advection becomes more organized to the northwest of the surface low, the PV notch is just beginning to form (Fig. 5.14b). It is hypothesized by Posselt and Martin (2004) that latent heat release, through clouds and precipitation, erodes the upper-level PV through diabatic dilution. The lack of a defined PV notch at t = +6 h and t = +12 h suggests the near-miss members are not associated with abundant clouds and precipitation to the northwest of their respective surface lows. This is supported by the no-latent-heat-release simulation by Posselt and Martin (2004) (their Fig. 11), which is similar to the upper-level PV evolution of the near-miss composite in Fig. 5.14. By t = +18 h, the upper-level PV hook and notch have developed despite being displaced from the PV advection maximum (Fig. 5.14d).

Cross sections of the PV anomalies, oriented similar to Fig. 4.17, are shown in Fig. 5.15. At t = 0 h, an upper-level cyclonic PV anomaly is visible upstream

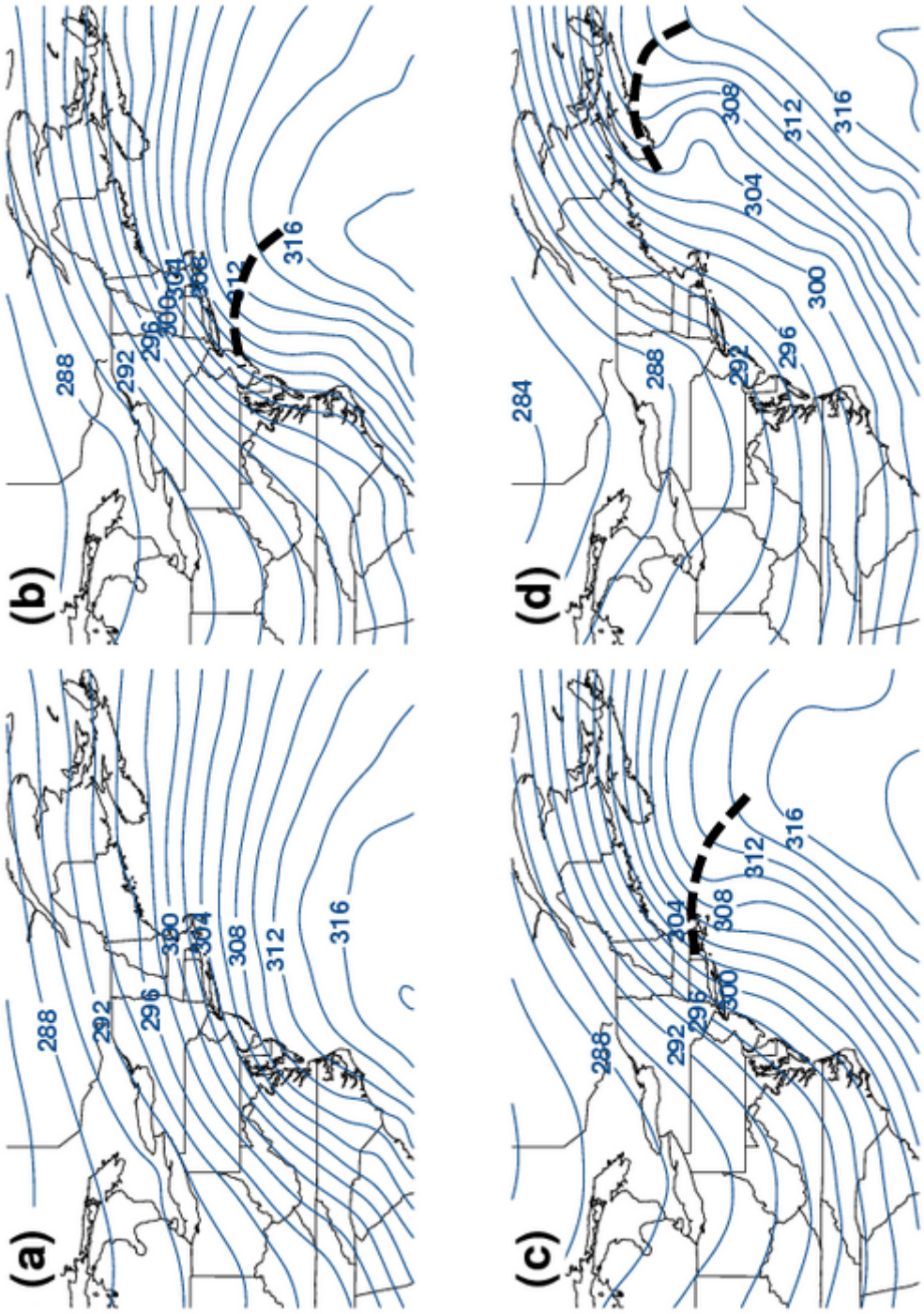

Figure 5.12: Near-miss composite 700-hPa equivalent potential temperature (solid blue, K) at: (a) t = 0 h; (b) t = +6 h; (c) t = +12 h; (d) t = +18 h. Thick dashed lines indicate the TROWAL position along the axis of maximum equivalent potential temperature.

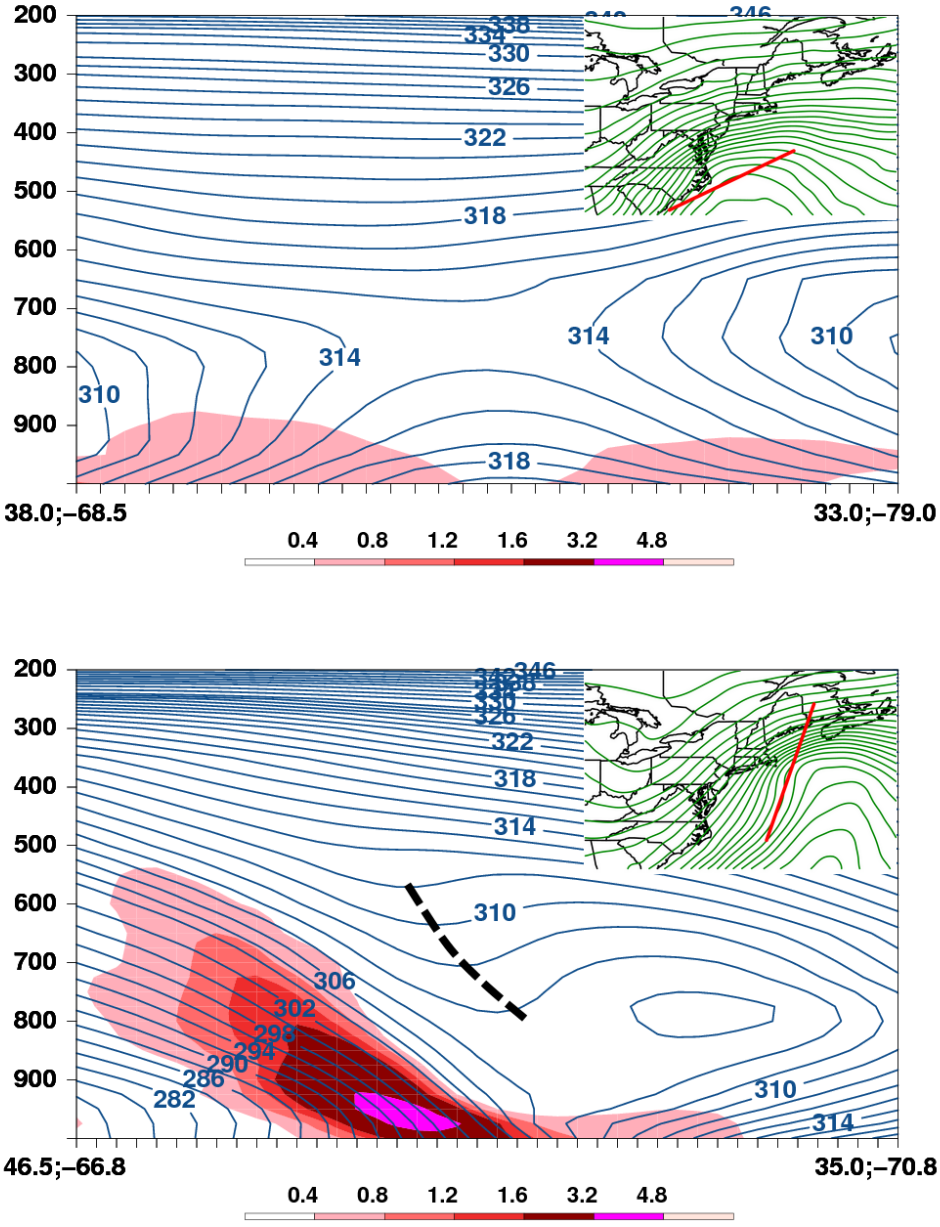

Figure 5.13: Near-miss composite vertical cross-section of equivalent potential temperature (solid blue, K) at: (top) t = 0 h; (bottom) t = +12 h. Inset Figure depicts the orientation of the vertical cross-section with 850-hPa equivalent potential temperature (solid green, K) for reference. Thick dashed line at t = +12 h indicates the TROWAL position along the axis of maximum equivalent potential temperature.

from the near-miss composite surface low (Fig. 5.15a,b). However, the downward penetration of the upper-level PV anomaly is only to approximately 500 hPa and the low-level PV anomaly is not visible. Twelve hours later, upper-level PV advection, the low-level PV anomaly (purple contours in Fig. 5.15c), and the potential temperature anomaly (shading in Fig. 5.15c) all increase. Although the low-level PV anomaly extends upward to approximately 700 hPa, the anomaly is weak and the PV circulations are not strongly coupled as in Davis and Emanuel (1991), Davis (1992), and Moore et al. (2008). This is further evidence that the near-miss composite is a weak three-dimensional ETC when it would be affecting the Northeast.

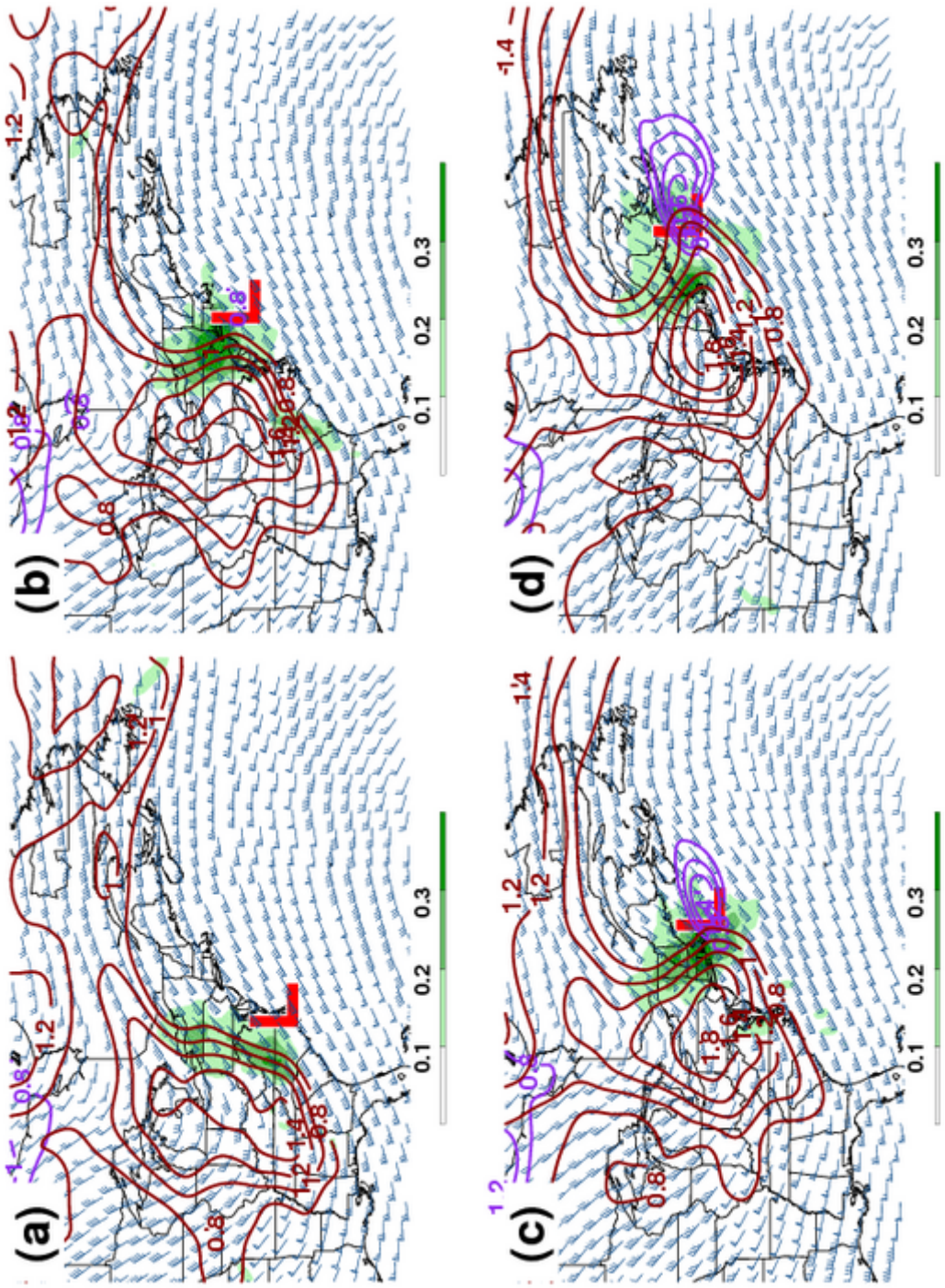

Figure 5.14: Near-miss composite 400-hPa PV (solid red; PVU), 975-hPa PV (solid purple; PVU), PV advection (shaded; PVU h^{-1}), and 400-hPa winds (barbs; kts) at: (a) t = 0 h; (b) t = +6 h; (c) t = +12 h; (d) t = +18 h. Surface low pressure centers are shown.

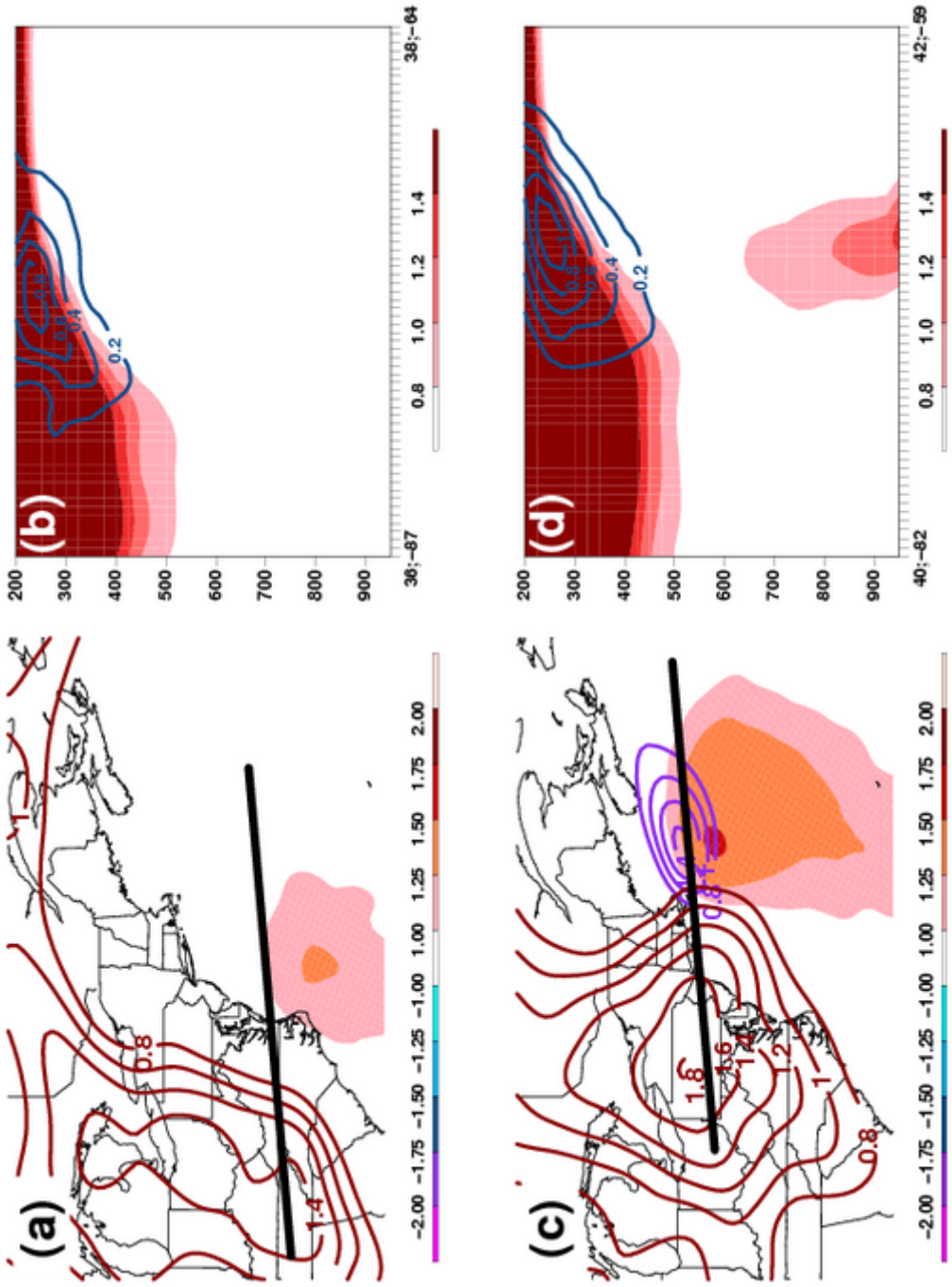

Figure 5.15: Near-miss composite at t = 0 h: (a) 400-hPa PV (solid red; PVU), 975-hPa PV (solid purple; PVU), and 2-m potential temperature standardized anomaly (shaded; σ); (b) vertical cross-section of PV (shaded; PVU) and PV advection (solid dk blue; PVU h^{-1}), and t = + 12h: (c) 400-hPa PV (solid red; PVU), 975-hPa PV (solid purple; PVU), and 2-m potential temperature standardized anomaly (shaded; σ); (d) vertical cross-section of PV (shaded; PVU) and PV advection (solid dk blue; PVU h^{-1}).

Chapter 6. Distinguishing Characteristics Between the Northeast Heavy Snow Conceptual Model and Near-Miss Composite

6.1 Analysis of Systematic Similarities and Differences

As discussed in Chapter 5, the near-miss composite ETC is similar to the "moderate" snowstorms analyzed in Kocin and Uccellini (2005). These moderate snowstorms were found to have fast-moving cyclones that could not sustain heavy snowfall rates for long periods. For the near-miss composite members, the surface cyclones were commonly associated with midlevel trough-ridge systems that did not amplify (Figs. 5.5c and 5.7c). After the 24-h composite period, the near-miss composite surface cyclone's position at t = +18 h was south of Nova Scotia (Fig. 5.7a) and approximately 400 km to the east of the NCM at the same time (Fig. 4.9a). This gives an indication that the majority of near-miss composite members have faster surface cyclone speeds. These are likely due to the reduction and amplification of the NCM midlevel trough-ridge half-wavelength (4.5c–4.9c) that eventually develops into a closed 500-hPa system (not shown). The intensification of the downstream ridge allows the NCM surface cyclone to track slower along a more meridional path compared with the near-miss composite.

The differences between the NCM and near-miss composite surface lows were indirectly shown in sections 4.2.1 and 5.2.1. A more direct comparison of the NCM and near-miss composite surface lows is shown through difference fields. In Fig. 6.1a, the strength of the NCM surface low is between 6 and 8 hPa

deeper than the near-miss composite, 6 h later that difference increases to more than 8 hPa (Fig. 6.2a), and 6 h later by more than 10 hPa (not shown). This suggests that even though the surface lows tend to deepen with both sets of members, the NCM members deepen at a faster rate. The differences in strength also occur with the 850-hPa height field as the NCM is 45–60 m deeper at t = +6 h (Fig. 6.1b) and 60–75 m deeper at t = +12 h (Fig. 6.2b). Furthermore, both the sea-level pressure and 850-hPa field scores are statistically significantly different at t = +6 h on the full domain at the 99% and 95% confidence levels, respectively. Aloft, mass fields do not exhibit large differences with respect to difference maps or statistics. The NCM 300- and 500-hPa height fields are deeper than the near-miss composite in the base of the midlevel and upper-level troughs at t = +6 h (Fig. 6.1c,d) and t = +12 h (Fig. 6.2c,d) but are not statistically different. Despite these slight differences, the character of the NCM midlevel trough is fundamentally different. For example, between t = +0 h and t = +18 h (Figs. 5.4c–5.7c) the NCM midlevel trough transitions from a neutrally to negatively tilted trough. This transition increases large-scale ascent and provides an environment conducive for strengthening the surface cyclone. During the same 18-h period, the near-miss composite midlevel trough does not undergo the same amplified transition. The differences observed between the NCM and near-miss composite midlevel troughs can, at the least, be partially responsible for the sea-level pressure differences in Figs. 6.1a and 6.2a.

The upper-level PV analyses of the NCM (Fig. 4.16) and near-miss composite (Fig. 5.14) both feature meridionally oriented PV anomalies that extend from a high-latitude PV reservoir to a low-latitude PV anomaly. Similar to Martin (1998a) and Posselt and Martin (2004), the anomalies eventually evolve into the treble clef structure or PV hook as the cyclones develop warm-occluded

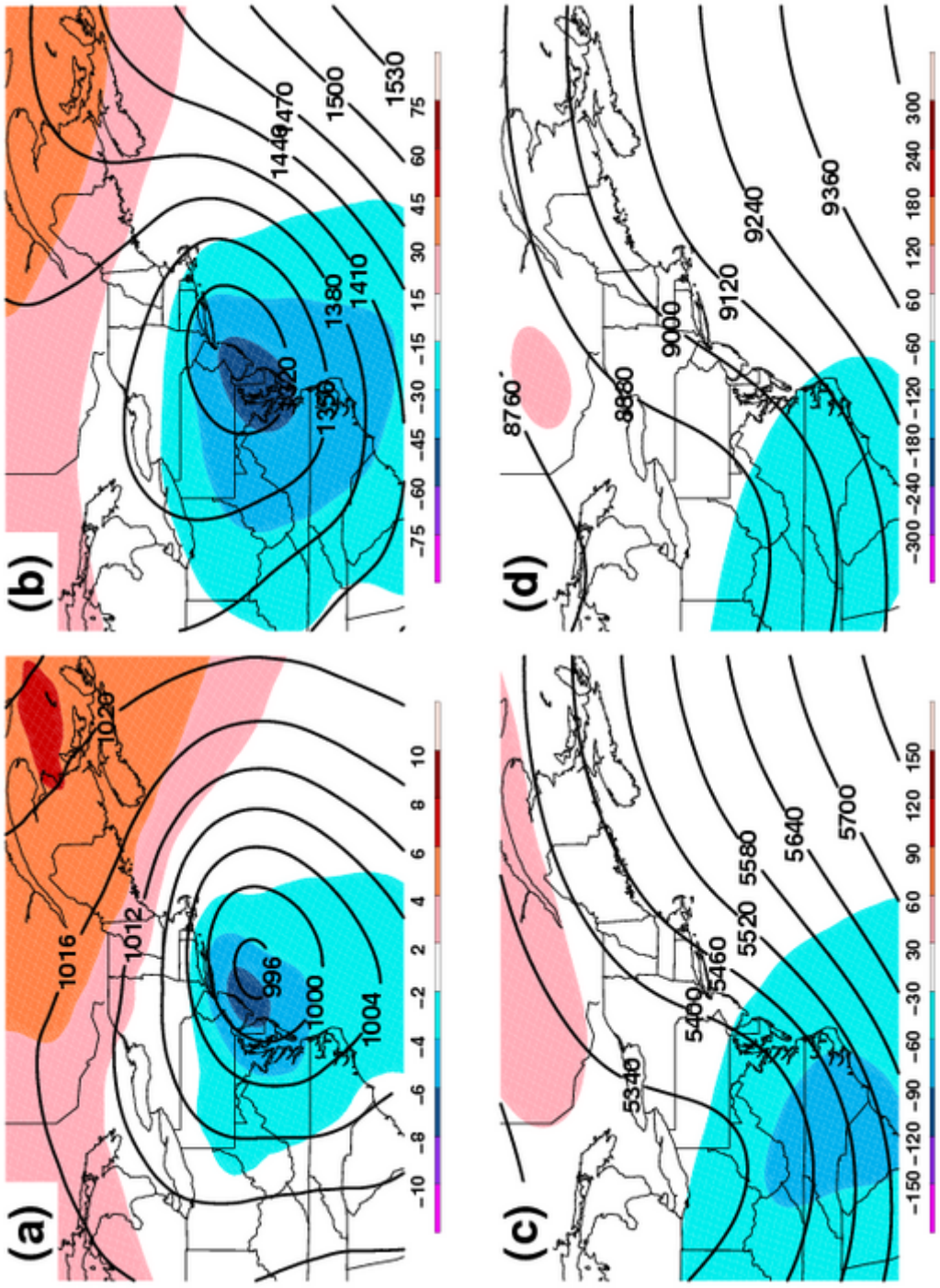

Figure 6.1: Difference fields (NCM – near-miss composite) at t = +6 h: (a) sea level pressure difference (shaded; hPa) and NCM sea level pressure (black; hPa); (b) 850-hPa geopotential height difference (shaded; m) and NCM 850-hPa geopotential height (black; m); (c) 500-hPa geopotential height difference (shaded; m) and NCM 500-hPa geopotential height (black; m); (d) 300-hPa geopotential height difference (shaded; m) and NCM 300-hPa geopotential height (black; m).

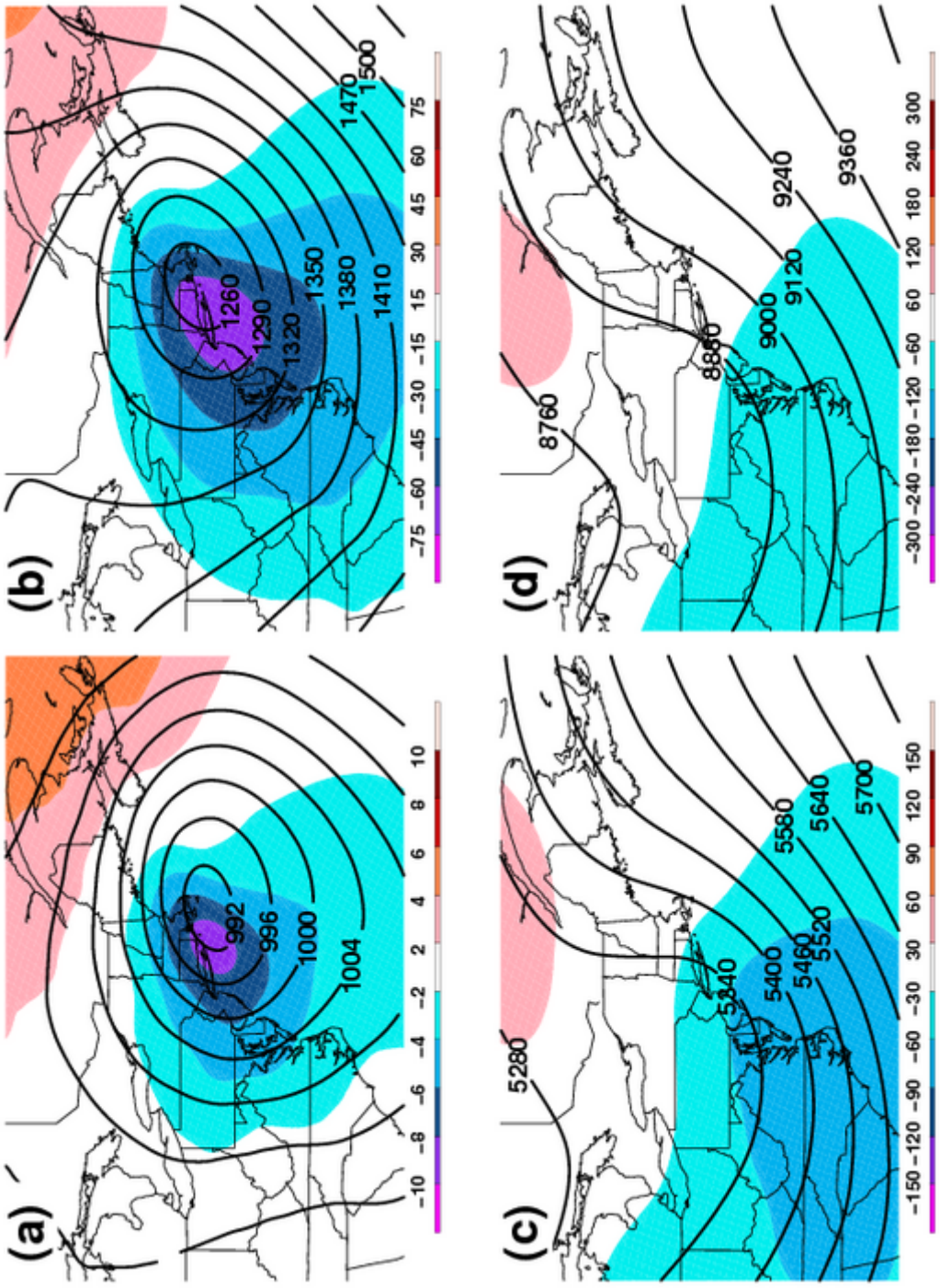

Figure 6.2: Difference fields (NCM – near-miss composite) at t = +12 h: (a) sea level pressure difference (shaded; hPa) and NCM sea level pressure (black; hPa); (b) 850-hPa geopotential height difference (shaded; m) and NCM 850-hPa geopotential height (black; m); (c) 500-hPa geopotential height difference (shaded; m) and NCM 500-hPa geopotential height (black; m); (d) 300-hPa geopotential height difference (shaded; m) and NCM 300-hPa geopotential height (black; m).

structures. The NCM begins to develop this structure at approximately t = 0 h and 6 h later is it fully developed (Figs. 4.16a,b). In contrast, the near-miss composite does not develop the PV hook until t = +18 h even though a low-latitude PV anomaly exists at t = 0 h (Figs. 5.14a,d). Posselt and Martin (2004) completed two simulations on a late winter East Coast cyclone, one with full physics (FP) and the other without latent heat release (NLHR). They noted that the NLHR simulation lagged the FP treble clef structure by about 6 h and was less intense through the remainder of the simulation. This suggests the importance of latent heat release in the development of the warm-occluded structure and the PV notch. Therefore, it can be argued that the near-miss composite lacks clouds and precipitation to the northwest of the surface cyclone between t = 0 h and t = +12 h when the cyclone would be affecting the majority of the Northeast.

The evolution of the NCM mesoscale environment is similar to the "banded PV hook" composite from Novak et al. (2010). The NCM 700-hPa frontogenesis field nearly doubles between t = 0 h and t = +6 h (Figs. 4.11a,b) as a midlevel trough forms and extends from the 700 hPa circulation along the southern coast of New England (Fig. 4.11c). Novak et al. (2009) found that as the heavy snow band dissipates, flow in the band region is altered by remote low-level diabatic PV anomalies that result in reduced deformation, convergence, and frontogenesis. A similar weakening in the NCM 700-hPa frontogenesis field occurs at t = +18 h (Fig. 4.11d) and while an isolated low-level PV anomaly was not present in the NCM, this is most likely due to small-scale variability of these anomalies. When comparing the NCM to the near-miss composite 700-hPa frontogenesis field, values were approximately 60% higher within the axis at t = +6 h. Furthermore, when the 700-850-hPa average frontogenesis fields

between the NCM members and near-miss composite members were compared across the northern half of the small domain in Fig. 3.2, the NCM members were found to be significantly higher at the 99% confidence level. This suggests that the midlevel frontogenesis field is a distinguishing characteristic between the NCM and near-miss composite.

6.2 In-Depth Analysis of Distinguishing Characteristics

Even though the near-miss composite members are statistically similar to the NCM, it is clear that there are distinguishing characteristics between the NCM and near-miss composite. The most significant are the structure and strength of the low-level (i.e., 700 and 850 hPa) mass fields and their impact on temperature and moisture transport into the system. At t = +6 h, the NCM and near-miss composite fields were compared and scored as described in Chapter 3. These comparative results reveal that the 700- and 850-hPa height scores in the northwestern quadrant are considerably lower than all other quadrants and fields (Table 6.1). To support these results, the NCM members and near-miss composite members are statistically significantly different at the 99% (850-hPa height) and 95% (700-hPa height) confidence levels in the northwestern domain. This indicates the importance of low-level mass fields and their resultant flow, in particular to the northwest of heavy snow producing ETCs. Therefore, the remainder of the comparative analysis will investigate how the differences in the mass fields develop and how those differences affect heavy snow production within East Coast ETCs.

The NCM develops a stronger 850-hPa closed cyclonic circulation between t = 0 h and t = +6 h, almost 12 h earlier than the near-miss composite (t = +12 h).

Table 6.1: Northeast conceptual model and near-miss composite comparison field and total scores.

	300-hPa height	**500-hPa height**	**700-hPa height**	**850-hPa height**	**Sea-level pressure**	**300-hPa isotachs**
Score Full	0.977	0.970	0.919	0.848	0.790	0.790
Score NW	0.956	0.935	0.332	0.125	0.866	0.818
Score NE	0.990	0.986	0.916	0.776	0.848	0.803
Score SE	0.982	0.978	0.940	0.900	0.882	0.864
Score SW	0.963	0.955	0.906	0.856	0.872	0.468

	850-hPa isotachs	**500-hPa RH**	**700-hPa RH**	**925-hPa mixing ratio**	**PWTR**	**700-hPa θ_e**
Score Full	0.805	0.834	0.779	0.939	0.938	0.933
Score NW	0.264	0.724	0.622	0.943	0.973	0.968
Score NE	0.728	0.883	0.882	0.927	0.955	0.941
Score SE	0.792	0.911	0.735	0.963	0.913	0.909
Score SW	0.917	0.589	0.761	0.906	0.870	0.874

	850-hPa θ_e	**850-hPa temp**	**2-m temp**	**700:850-hPa avg fgen**	**PV**	**Total score**
Score Full	0.940	0.932	0.975	0.640	0.885	14.894
Score NW	0.947	0.930	0.962	0.489	0.768	12.620
Score NE	0.931	0.930	0.973	0.595	0.925	14.989
Score SE	0.970	0.957	0.978	0.582	0.932	15.189
Score SW	0.902	0.886	0.966	0.356	0.831	13.878

This difference can be attributed to how the low-level flow evolves at, and before, the initial analysis time. Kocin and Uccellini (2005) state that sensible heat fluxes over the western Atlantic Ocean to the east of a surface low can act to increase the low-level thermal gradient, which can contribute to stronger low-level wind speeds that enhance thermal advections and cyclone deepening. The increase in wind speed (i.e., development of the LLJ) is related to changes in the horizontal and vertical pressure gradient forces with vertical parcel displacements being enhanced by sensible and latent heat fluxes and latent heat release (Kocin and Uccellini 2005). The increase in warm-air advection and latent heat release ahead of the surface cyclone strengthen and decrease the propagation of the upper-level ridge which has an important role in decreasing the half-wavelength of the trough-ridge system (Uccellini and Kocin 1987). Uccellini and Kocin (1987) also note that the formation of the southeasterly LLJ to the north and northeast of the developing cyclone and its impacts on cyclone deepening, thermal and moisture advections, and latent heat release through precipitation interact to support the self-development theory discussed in section 2.2.1.

Between t = -6 h and t = 0 h the NCM surface low strengthened 6 hPa to 1002 hPa, while the near-miss composite only strengthened approximately 2 hPa. A strengthening surface low with a more intense low-level wind field suggests stronger cold air advection along the eastern United States coastal plain. At t = -6 h, the axes and magnitudes of the NCM and near-miss composite 975-hPa temperature gradients are similar in position and strength (Fig. 6.3a,b). They extend behind the warm and cold fronts from the border of Virgina and North Carolina southwestward along the eastern side of the Appalachian Mountains. The low-level wind fields are also similar in the vicinity of the surface cyclone; however, the NCM surface winds are slightly stronger in the warm sector and

the 850-hPa winds are more southerly downstream of the 850-hPa trough axis (Fig. 4.5b).

By t = 0 h, the magnitude of the NCM 975-hPa temperature gradient has strengthened and expanded northeastward (Fig. 6.3c). The change in the NCM low-level thermal gradient is likely the result of the deepening cyclone and provides support for strengthening the LLJ and southeasterly flow just downstream of the deepening 850-hPa trough axis through the thermal wind concept. As the low-level thermal gradient increases, an increase in geostrophic shear and geostrophic wind takes place aloft thereby turning the real wind towards lower heights (i.e., northwest). At t = 0 h, the NCM 850-hPa ageostrophic component of the real wind was southeasterly and orthogonal to the low-level temperature gradient (not shown). This suggests an enhancement in the real wind and the development of the easterly (i.e., *u*-) component of the 850-hPa wind.

The LLJ plays an important role in enhancing and focusing thermal advections and moisture transport toward the area of heavy precipitation (Kocin and Uccellini 2005). In the NCM and near-miss composite, warm-air advection and moisture transport is implied as the LLJ is aligned along the aforementioned axes (Figs. 4.8 and 5.6). However, the stronger LLJ in the NCM results in increased low-level advections and transport. For example, at t = 0 h, strong NCM 850-hPa temperature advection is occurring along the nose of the low-level jet to the north and northeast of the surface cyclone (Fig. 6.4a). In contrast, weaker and less focused temperature advection is associated with near miss composite 850-hPa wind maximum and low-level thermal gradient (Fig. 6.4b). The structure and intensity of the NCM warm-air advection just upwind of the midlevel ridge, even at t = 0 h, suggests that the ridge will begin to strengthen

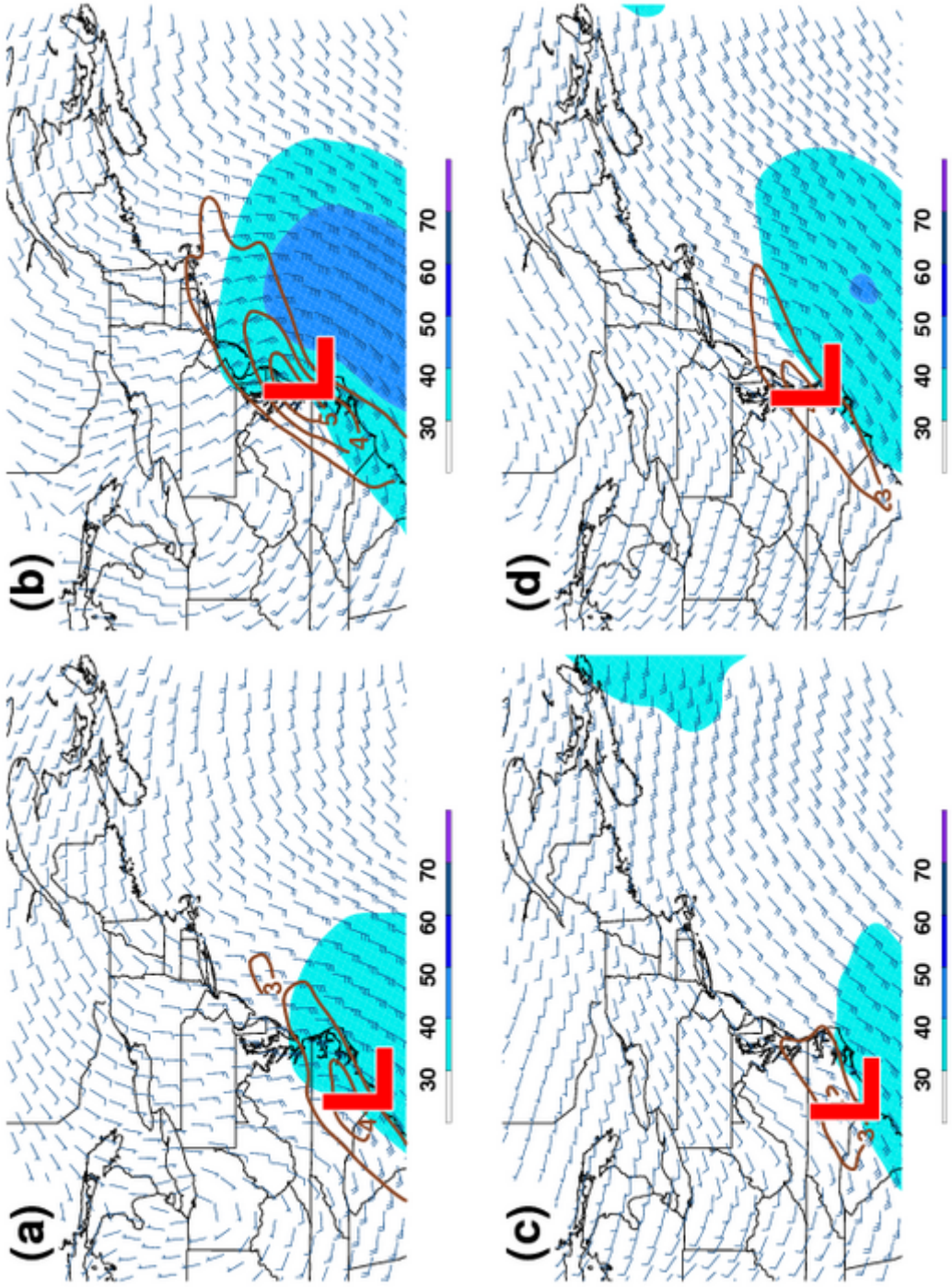

Figure 6.3: Northeast conceptual model (a) t = -6 h; (b) t = 0 h; and near-miss composite (c) t = -6 h; (d) t = 0 h; 975-hPa temperature gradient (solid brown; m), 850-hPa wind speed (shaded; kts), and 850-hPa winds (barbs; kts). Surface low pressure centers are shown.

and the downwind propagation slow. Twelve hours later, the NCM 850-hPa warm-air advection increases and is approximately twice as strong as the near-miss composite advection field. Strong thermal advection allows the NCM midlevel ridge to remain nearly stationary over the northeastern United States and it only begins to rotate cyclonically as the midlevel trough approaches.

In addition to thermal advections, considerable differences between moisture advection (not shown) and moisture convergence fields were also noted between the NCM and near-miss composite. At both t = +6 h and t = +12 h, the NCM 850-hPa moisture convergence field is approximately 66% stronger than the near-miss composite (Fig. 6.5). This suggests that more moist air is being transported northward into the cyclone and being lifted into the NCM low-level frontal zone than in the near-miss composite. In addition, the NCM 850-hPa moisture convergence and warm-air advection fields extend to the northwest of the surface low just on the equatorward side of the frontogenesis axis. Similar to the PV hook composite from Novak et al. (2010), the convergence is focused along the midlevel trough and just poleward of the TROWAL axis as the 850-hPa wind field turns cyclonically with an increase of the *u*- component of the wind.

Patterns and associated anomalies have been used to identify significant weather events and provide meteorological insight to the forecaster (Grumm and Hart 2001). Most of published literature has shown the use of anomalies in heavy precipitation events (e.g., Bell and Janowiak 1995; Junker et al. 2009), however, Grumm and Hart (2001) and Stuart and Grumm (2006) showed the importance of using low- and upper-level wind anomalies to indicate the severity of East Coast winter storms. For example, *u*- component wind anomalies on the northern side of an East Coast cyclone are an indication of strong easterly winds which can transport moisture from the Atlantic Ocean and provide forcing

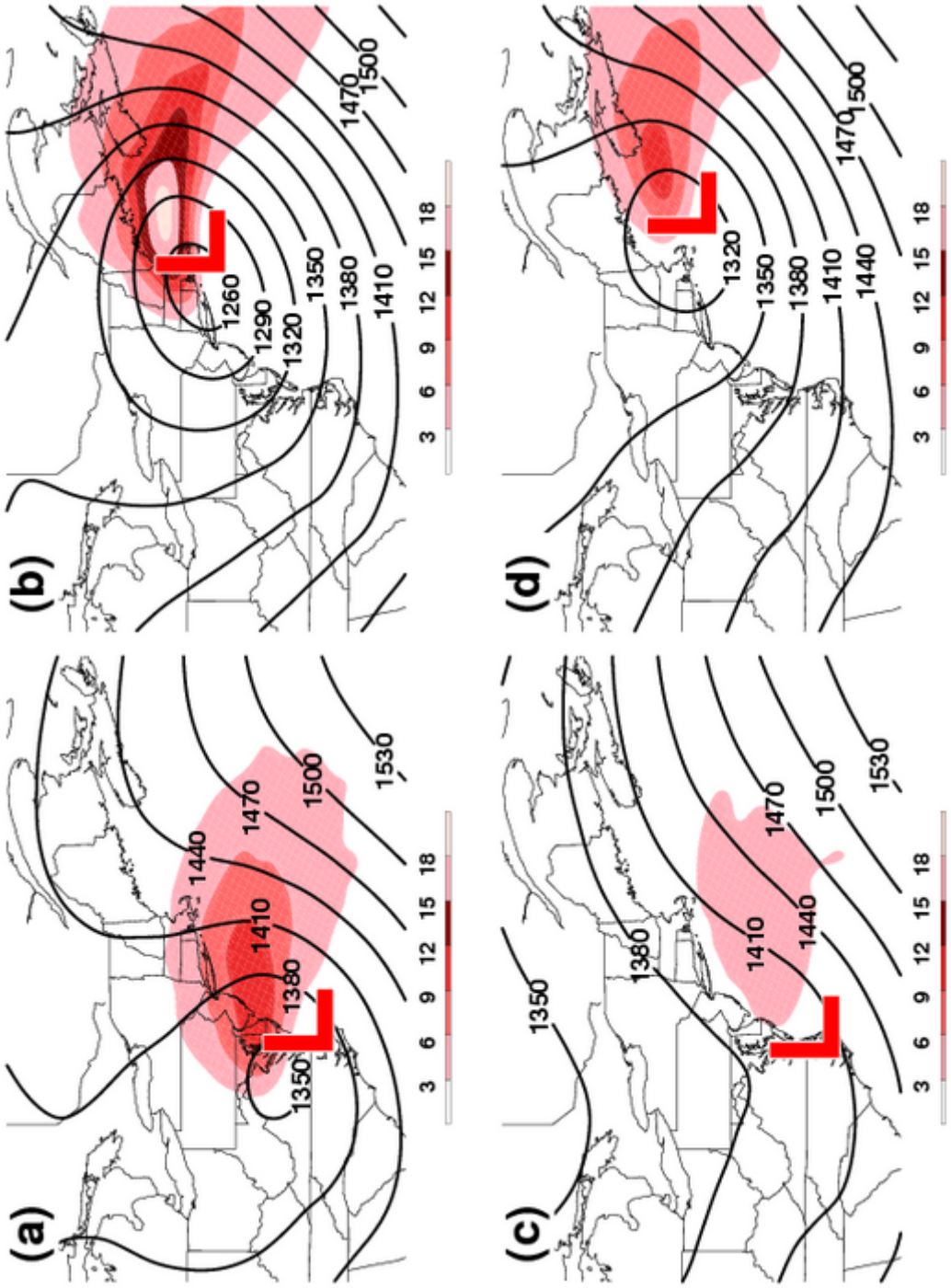

Figure 6.4: Northeast conceptual model (a) t = 0 h; (b) t = +12 h; and near-miss composite (c) t = 0 h; (d) t = +12 h; 850-hPa temperature advection (shaded; K $(6\ h)^{-1}$) and 850-hPa geopotential height (solid black; m). Surface low pressure centers are shown.

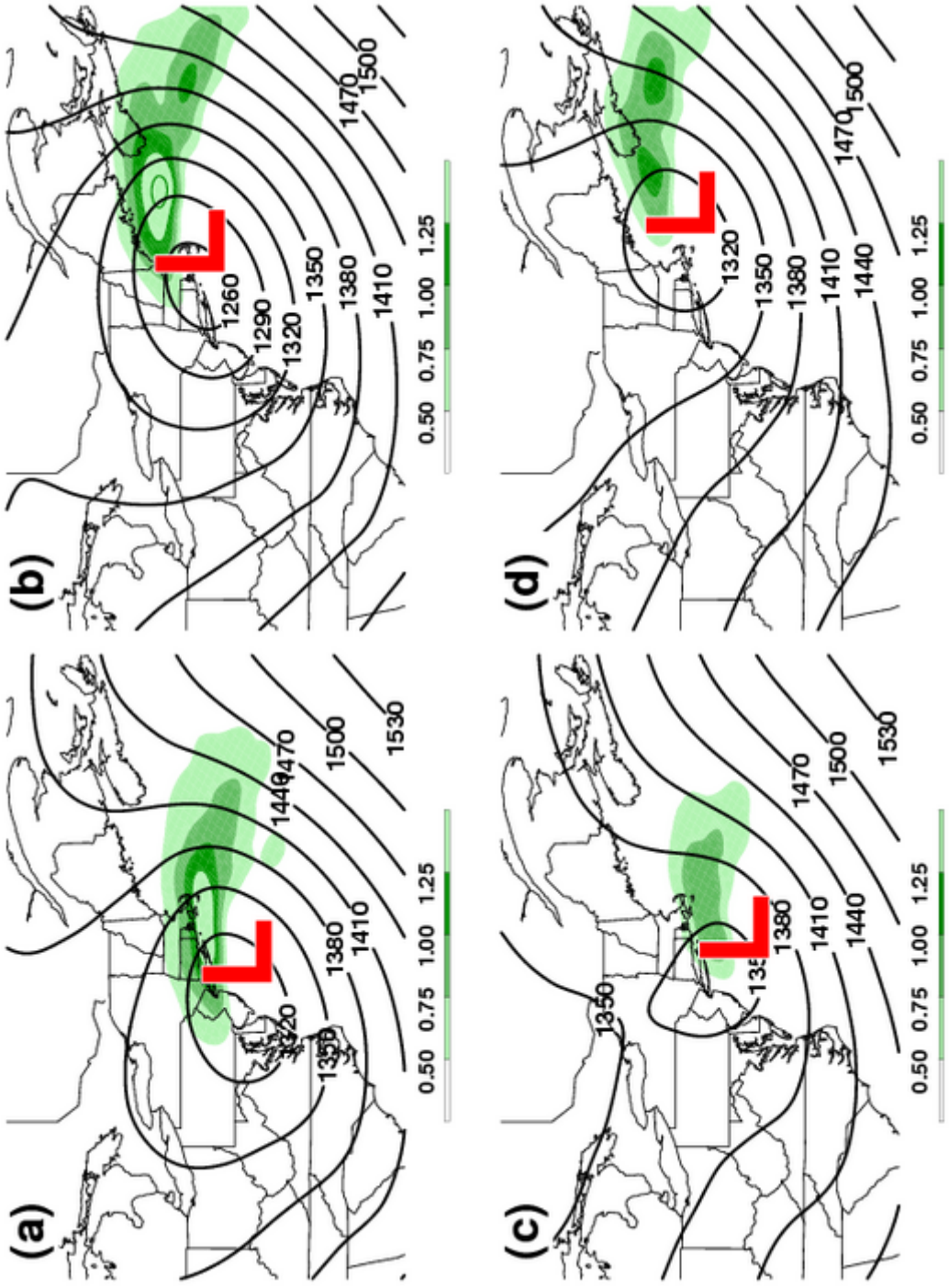

Figure 6.5: Northeast conceptual model (a) t = +6 h; (b) t = +12 h; and near-miss composite (c) t = +6 h; (d) t = +12 h; 850-hPa moisture convergence (shaded; g Kg^{-1} $(h)^{-1}$) and 850-hPa geopotential height (solid black; m). Surface low pressure centers are shown.

through convergence, thereby promoting vertical motions and precipitation production (Stuart and Grumm 2006). Grumm and Hart (2001) defined the term anomalous to fields that depart by more than 2.5 standard deviations from the 30-yr means. For a normal distribution, this departure implies that the anomalous field occurs only around 1% of the time at any given location (Hart and Grumm 2001; Grumm and Hart 2001).

As discussed at the beginning of section 6.2, the lowest field scores computed between the NCM and near-miss composite are clearly low-level geopotential height fields (i.e., 700 and 850 hPa), which is supported by the statistically significant differences in the northern and northwestern quadrants. These differences are magnified when the 850-hPa *u*- component of the wind and wind anomalies are analyzed. At t = 0 h, the NCM *u*- component of the wind to the north of the surface cyclone is approximately 15 kts (Fig. 6.6a) with an anomaly between -2.0 and -3.0σ (Fig. 6.6c). This signal becomes better defined over the next 6 h as the *u*- component of the wind increases to 25 kts and anomalies decrease to -3.0 and -4.0σ within the strongest portion of the *u*- wind (Fig. 6.7). The anomaly values visible in the NCM, occur only approximately 0.1% of the time over the 30-yr distribution (Grumm and Hart 2001). This leads to large differences between the NCM and near-miss composite at t = +6 h as a 10-kts *u*- component of the wind isotach is not visible and anomalies are only between -1.0 and -2.0σ. It is clear that the 850-hPa wind field to the north of the surface cyclone is the most distinguishing characteristic between the NCM and near-miss composite. Furthermore, this result supports the limited published research using wind anomalies in East Coast winter storms and shows the importance in using low-level wind anomalies when forecasting these high impact events.

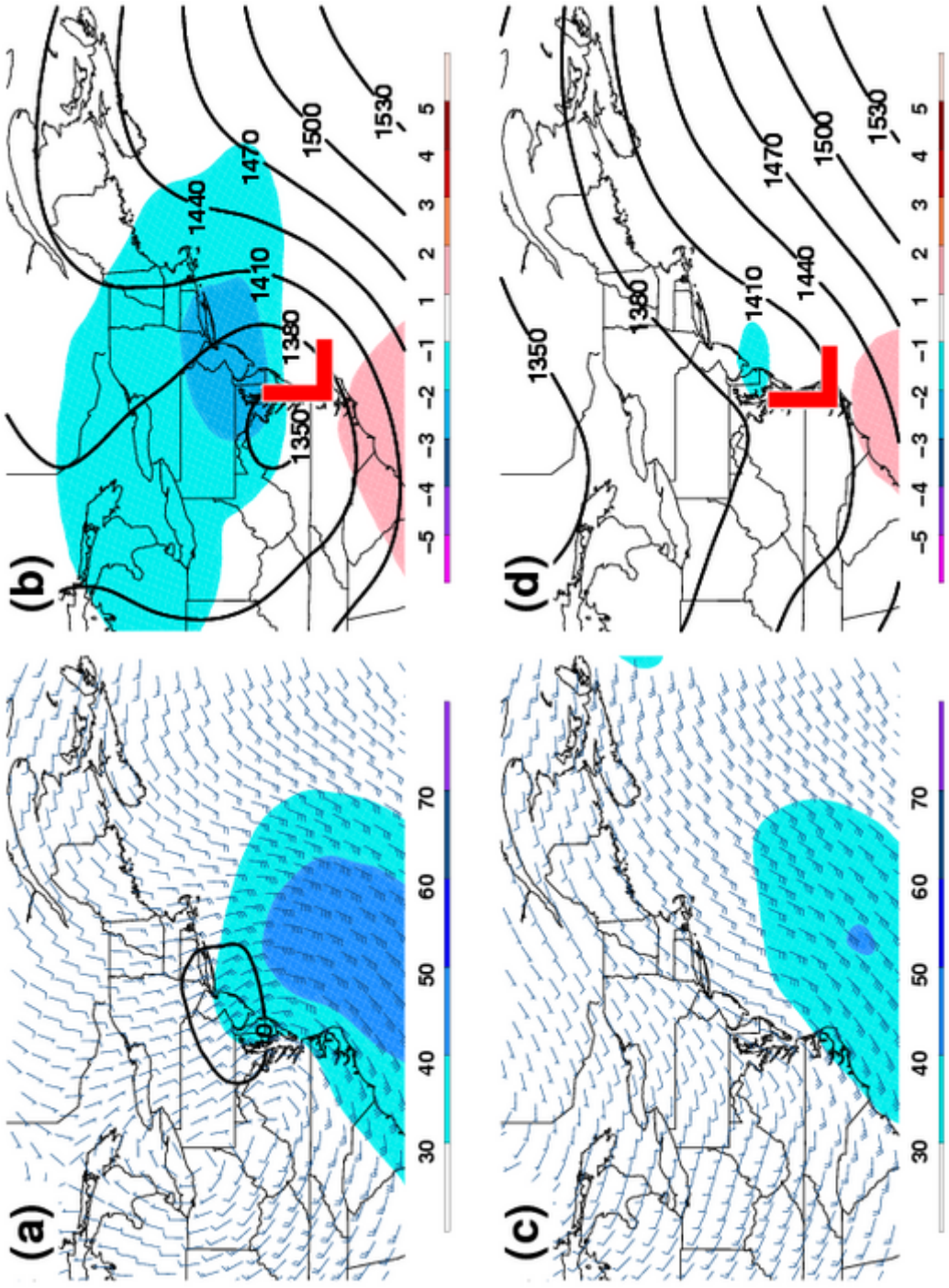

Figure 6.6: Northeast conceptual model (a) and near-miss composite (c) 850-hPa wind speed (shaded; kts), u- isotachs (solid black; kts), and winds (barbs; kts); and Northeast conceptual model (b) and near-miss composite (d) 850-hPa wind anomalies (shaded; σ) and geopotential height (solid black; m) at t = 0 h. Surface low pressure centers are shown.

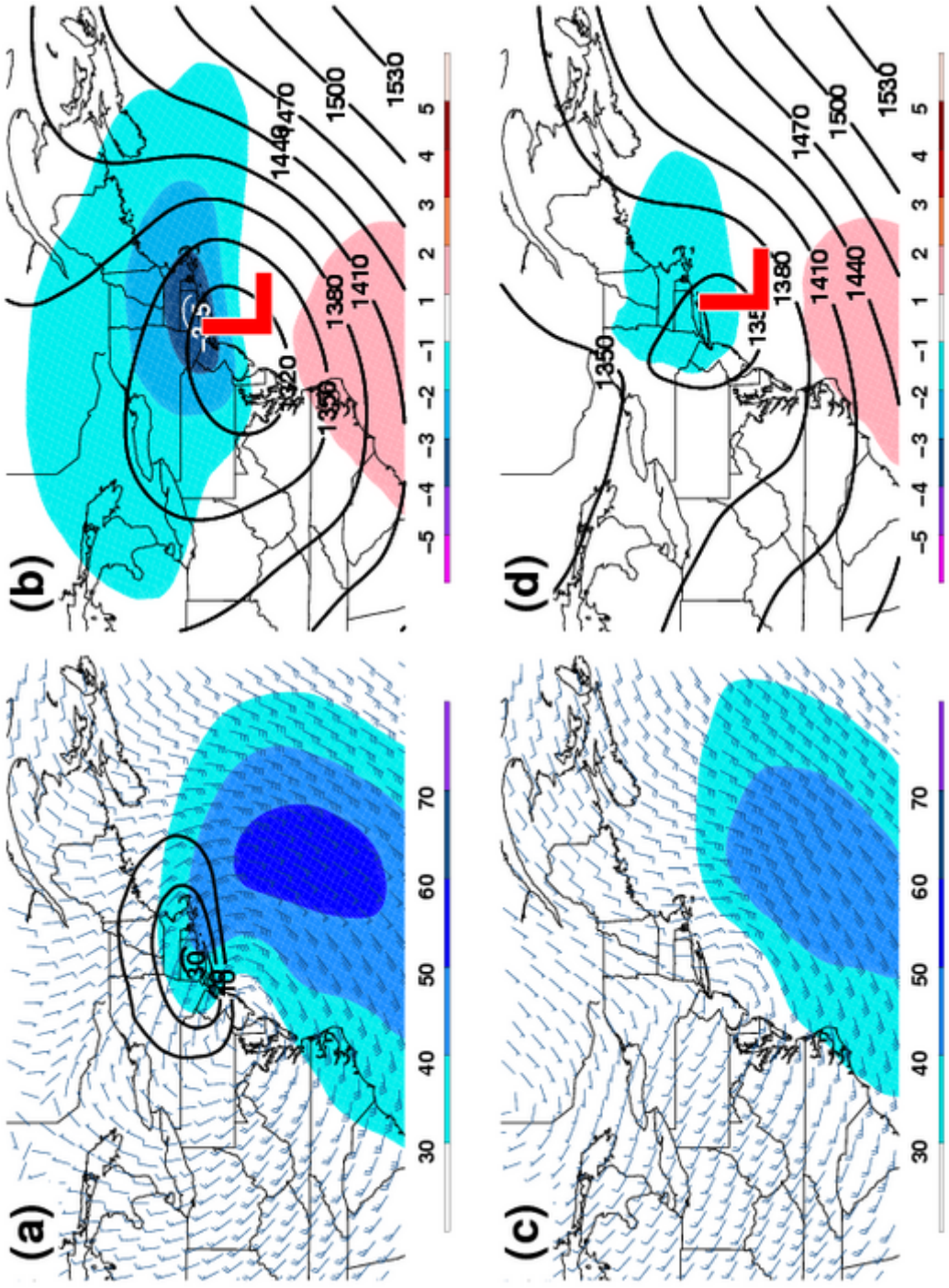

Figure 6.7: Northeast conceptual model (a) and near-miss composite (c) 850-hPa wind speed (shaded; kts), u- isotachs (solid black; kts), and winds (barbs; kts); and Northeast conceptual model (b) and near-miss composite (d) 850-hPa wind anomalies (shaded; σ) and geopotential height (solid black; m) at t = +6 h. Surface low pressure centers are shown.

Chapter 7. Summary and Conclusions

A 28-yr climatology and CM of coastal-track Northeast heavy snow events, near-miss coastal-track Northeast heavy snow events, and distinguishing characteristics between the NCM and near-miss composite were presented. The 41-member NCM confirmed Northeast heavy snow CMs in the literature. Numerous studies have analyzed Northeast heavy snow events, however few have investigated null events and none have identified them objectively. Using the NCM, 25 near-miss Northeast heavy snow events similar to the NCM were objectively identified and analyzed. A qualitative comparison between the NCM and near-miss composite highlighted several systematic differences that were confirmed with a statistical analysis. The 850-hPa easterly wind anomaly to the north of the cyclone center was the most distinguishing characteristic. The stronger NCM 850-hPa u- component of the wind increases thermal advection, moisture transport, and frontogenesis in the comma-head portion of the cyclone.

Although distinguishing characteristics were present in the statistical analysis, the NCM and near-miss heavy snow events had similar large-scale flow patterns. Therefore, a climatological frequency of Northeast coastal heavy snow events was determined. The result of this analysis revealed that during December, January, and February, 62% (41 of 66) of coastal-track surface lows similar to the NCM produce heavy snow in the Northeast. This suggests that surface lows that track north-northeastward along the East Coast and resemble the NCM are more likely to produce heavy snow across the Northeast.

The methodology applied in this study to find near-miss events similar to a CM has merit. The algorithm was able to objectively identify similar events to the CM while using simple diagnostics. Although the patterns of the CM were

captured, localized differences on the scale of the sub domains were present that had a significant impact on the sensible weather. This is the first study of this type, which gives numerous avenues for future research, including: refining the process to be completed more efficiently, applying to other meteorological phenomena, examining the sensitivity to the size of the spatial domains, and accounting for highly localized features.

References

Adams, R., L. Houston, and R. Weiher, 2004: *The Value of Snow and Snow Information Services*. Report prepared for NOAA's National Operational Hydrological Remote Sensing Center, [Available online at www.economics.noaa.gov/bibliography/econ-value-snow-final-report.doc].

Auer, A. H., and J. M. White, 1982: The combined role of kinematics, thermodynamics, and cloud physics associated with heavy snowfall episodes. *J. Meteor. Soc. Japan*, **60**, 500–507.

Banacos, P. C., 2003: Short-range prediction of banded precipitation associated with deformation and frontogenesis forcing. Preprints*, Tenth Conf. on Mesoscale Processes*, Amer. Meteor. Soc., Portland, OR, CDROM, P1.7.

Baumgardt, D., 2000: Precipitation type forecasting. [Available online at http://rammb.cira.colostate.edu/visit/ptype/title.asp].

Bell, G. D., and J. E. Janowiak, 1995: Atmospheric circulation associated with the Midwest floods of 1993. *BAMS*, **76**, 681–695.

Bennetts, D. A., and B. J. Hoskins, 1979: Conditional symmetric instability – a possible explanation for frontal rainbands. *Quart. J. Roy. Meteor. Soc.*, **105**, 945–962.

Bjerknes, J., 1919: On the structure of moving cyclones. *Geofys. Publ.*, **1**, 1–8.

Bjerknes, J., and J. Holmboe, 1944: On the theory of cyclones. *J. Atmos. Sci.*, **1**, 1–22.

Bjerknes, J., and H. Solberg, 1923: Life cycle of cyclones and the polar front theory of atmospheric circulation. *Geofys. Publ.*, **3**, 1–18.

Bluestein, H. B., 1992: *Synoptic-Dynamic Meterology in Midlatitudes, Volume I, Principles of Kinematics and Dynamics*. Oxford University Press, 431 pp.

—, 1993: *Synoptic-Dynamic Meterology in Midlatitudes, Volume II, Observations and Theory of Weather Systems*. Oxford University Press, 594 pp.

Bosart, L. F., G. J. Hakim, K. R. Tyle, M. A. Bedrick, M. J. Dickinson, and D. M. Schultz, 1996: Large-scale antecedent conditions associated with the 12–14 March 1993 cyclone ("superstorm '93") over eastern North America. *Mon. Wea. Rev.*, **124**, 1865–1891.

Bosart, L. F., and F. Sanders, 1986: Mesoscale structure in the Megalopolitan snowstorm of 11–12 February 1983. Part III: A large-amplitude gravity wave. *J. Atmos. Sci.*, **43**, 924–939.

Brandes, E. A., and J. Spar, 1971: A search for necessary conditions for heavy snow on the East Coast. *J. Appl. Meteor.*, **10**, 397–409.

Brennan, M. J., G. M. Lackmann, and K. M. Mahoney, 2008: Potential vorticity (PV) thinking in operations: The utility of nonconservation. *WAF*, **23**, 168–182.

Browne, R. F., and R. J. Younkin, 1970: Some relationships between 850-millibar lows and heavy snow occurences over the central and eastern United States. *Mon. Wea. Rev.*, **98**, 399–401.

Browning, K. A., 1999: Mesoscale aspects of extratropical cyclones: An observational perspective. *The Life Cycles of Extratropical Cyclones*, M. A. Shapiro and S. Gronas, Eds., Amer. Meteor. Soc., pp. 265–283.

Byrd, G. P., 1989: A composite analysis of winter season overrunning precipitation bands over the Southern Plains of the United States. *J. Atmos. Sci.*, **46**, 1119–1132.

Caplan, P. M., 1995: The 12–14 March 1993 Superstorm: Performance of NCEP global medium range model. *Bull. Amer. Meteor. Soc.*, **76**, 201–212.

Carlson, T. N., 1980: Airflow through midlatitude cyclones and the comma cloud pattern. *Mon. Wea. Rev.*, **108**, 1498–1509.

—, 1998: *Mid-latitude Weather Systems*. Amer. Meteor. Soc., 507 pp.

Changnon, S. A., and D. Changnon, 2006: A spatial and temporal analysis of damaging snowstorms in the United States. *Nat. Hazards*, **37**, 373–389.

COMET, 2002: Heavy Banded Snow by James T. Moore. [Available online at http://meted.ucar.edu/norlat/bandedsnow].

Crocker, A., W. Godson, and C. Penner, 1947: Frontal contour charts. *J. Appl. Meteor.*, **4**, 94–99.

Danielsen, E. F., 1964: Project Springfield Report. Defense Atomic Support Agency, DASA 1517, 97 pp. [NTIS AD-607980.].

Davis, C. A., 1992: A potential vorticity diagnosis of the importance of initial structure and condensational heating in observed extratropical cyclogenesis. *Mon. Wea. Rev.*, **120**, 2409–2428.

Davis, C. A., and K. A. Emanuel, 1991: Potential vorticity diagnostics of cyclogenesis. *Mon. Wea. Rev.*, **119**, 1929–1952.

desJardins, M. L., K. F. Brill, and S. S. Schotz, 1991: Use of GEMPAK on UNIX workstations. Proceedings, 7^{th} *Int. Conf. On Interactive Information and Processing Systems for Meteorology, Oceanography, and Hydrology*, New Orleans, LA, Amer. Meteor. Soc., 449–453.

Durnford, D., J. Gyakum, and E. Atallah, 2009: The conversion of total column ozone data to numerical weather prediction model initializing fields, with simulations of the 24–25 January 2000 East Coast snowstorm. *Mon. Wea. Rev.*, **137**, 161–188.

Emanuel, K., 1985: Frontal circulations in the presence of small moist symmetric stability. *J. Atmos. Sci.*, **42**, 1062–1071.

Fawcett, E. B., and H. K. Saylor, 1965: A study of the distribution of weather accompanying Colorado cyclongenesis. *Mon. Wea. Rev.*, **93**, 359–367.

Gilhousen, D. B., 1994: The value of the NDBC observations during March 1993's "Storm of the Century". *Wea. Forecasting*, **9**, 255–264.

Goree, P. A., and R. J. Younkin, 1966: Synoptic climatology of heavy snowfall over the central and eastern United States. *Mon. Wea. Rev.*, **94**, 633–668.

Grumm, R. H., and R. E. Hart, 2001: Standardized anomalies applied to significant cold season weather events: Preliminary findings. *WAF*, **16**, 736–754.

Gurka, J. J., E. P. Auciello, A. F. Gigi, J. S. Waldstreicher, K. K. Keeter, S. Businger, and L. G. Lee, 1995: Winter weather forecasting throughout the eastern United States. Part II: An operational perspective of cyclogenesis. *Wea. Forecasting*, **10**, 21–41.

Gyakum, J. R., 1987: Evolution of a surprise snowfall in the United States Midwest. *J. Atmos. Sci.*, **115**, 2322–2345.

Halcomb, C., and P. Market, 2003: Forcing, instability and equivalent potential vorticity in a Midwest USA convective snowstorm. *Meteor. Appl.*, **10**, 273–280.

Harrold, T. W., 1973: Mechanisms influencing the distribution of precipitation within baroclinic disturbances. *Quart. J. Roy. Meteor. Soc.*, **99**, 232–251.

Hart, R. E., and R. H. Grumm, 2001: Using normalized climatological anomalies to rank synoptic-scale events objectively. *MWR*, **129**, 2426–2442.

Holton, J. R., 1992: *An Introduction to Dynamic Meteorology*. 3rd ed. Academic Press, 511 pp.

Hoskins, B. J., I. Draghici, and H. Davies, 1978: A new look at the ω-equation. *Quart. J. Roy. Meteor. Soc.*, **104**, 31–38.

Hoskins, B. J., M. E. McIntyre, and A. W. Robertson, 1985: On the use and significance of isentropic potential vorticity maps. *Quart. J. Roy. Meteor. Soc.*, **111**, 877–946.

Huo, Z., D.-L. Zhang, J. R. Gyakum, and A. Stantiforth, 1995: A diagnostic analysis of the superstorm of March 1993. *Mon. Wea. Rev.*, **123**, 1740–1761.

Junker, N. W., M. J. Brennan, F. Pereira, M. J. Bodner, and R. H. Grumm, 2009: Assessing the potential for rare precipitation events with standardized anomalies and ensemble guidance at the Hydrometeorological Prediction Center. *BAMS*, **90**, 445–453.

Keeter, K. K., S. Businger, and L. G. L. J. S. Waldstreicher, 1995: Winter weather forecasting throughout the eastern United States. Part III: The effects of topography and the variability of winter weather in the Carolinas and Virginia. *Wea. Forecasting*, **10**, 42–60.

Keyser, D., B. D. Schmidt, and D. G. Duffy, 1992: Quasigeostrophic vertical motions diagnosed from along- and cross-isentrope components of the Q vector. *Mon. Wea. Rev.*, **120**, 731–741.

Kleist, D. T., and M. C. Morgan, 2005: Application of adjoint-derived forecast sensitivities to the 24–25 January 2000 U.S. East Coast snowstorm. *Mon. Wea. Rev.*, **133**, 3148–3175.

Kocin, P. J., P. N. Schumacher, R. F. Morales, and L. W. Uccellini, 1995: Overview of the 12–14 March 1993 superstorm. *Bull. Amer. Meteor. Soc.*, **76**, 165–182.

Kocin, P. J., and L. W. Uccellini, 1990: *Snowstorms Along the Northeastern Coast of the United States: 1955 to 1985. Meteor. Monogr.* No. 44, Amer. Meteor. Soc., 280 pp.

—, 2004: A snowfall impact scale derived from Northeast storm snowfall distributions. *Bull. Amer. Meteor. Soc.*, **85**, 177–194.

—, 2005: *Northeast Snowstorms*. Vols. 1 and 2, *Meteor. Monogr.*, No. 54, Amer. Meteor. Soc., 818 pp.

Lackmann, G. M., L. F. Bosart, and D. Keyser, 1996: Planetary- and synoptic-scale characteristics of explosive wintertime cyclogenesis over the western north atlantic ocean. *Mon. Wea. Rev.*, **124**, 2672–2702.

Langland, R. H., M. A. Shapiro, and R. Gelaro, 2002: Initial condition sensitivity and error growth in forecasts of the 25 January 2000 East Coast snowstorm. *Mon. Wea. Rev.*, **130**, 957–974.

Maglaras, G. J., J. S. Waldstreicher, P. J. Kocin, A. F. Gigi, and R. A. Marine, 1995: Winter weather forecasting throughout the eastern United States. Part I: An overview. *Wea. Forecasting*, **10**, 5–20.

Martin, J. E., 1998a: The structure and evolution of a continental winter cyclone. Part I: Frontal structure and the classical occlusion process. *Mon. Wea. Rev.*, **126**, 303–328.

—, 1998b: The structure and evolution of a continental winter cyclone. Part II: Frontal forcing of an extreme snow event. *Mon. Wea. Rev.*, **126**, 329–347.

—, 1999: Quasigeostrophic forcing of ascent in the occluded sector of cyclones and the trowal airstream. *Mon. Wea. Rev.*, **127**, 70–88.

Mesinger, F., and Coauthors, 2006: North American regional reanalysis. *Bull. Amer. Meteor. Soc.*, **87**, 343–360.

Miller, J. E., 1946: Cyclogenesis in the Atlantic coastal region of the United States. *J. Atmos. Sci.*, **3**, 31–44.

—, 1948: On the concept of frontogenesis. *J. Meteor.*, **5**, 169–171.

Mook, C. P., and K. S. Norquest, 1956: The heavy snowstorm of March 18-19, 1956. *Mon. Wea. Rev.*, **84**, 116–125.

Moore, J. T., and P. D. Blakley, 1988: The role of frontogenetical forcing and conditional symmetric instability in the midwest snowstorm of 30–31 January 1982. *Mon. Wea. Rev.*, **116**, 2155–2171.

Moore, J. T., F. H. Glass, C. E. Graves, S. M. Rochette, and M. Singer, 2003: The environment of warm-season elevated thunderstorms associated with heavy rainfall over the central United States. *Wea. Forecasting*, **18**, 861–878.

Moore, J. T., C. E. Graves, S. Ng, and J. L. Smith, 2005: A process-oriented methodology towards understanding the organization of an extensive mesoscale snowband: A diagnostic case study of 4–5 December 1999. *Wea. Forecasting*, **20**, 35–50.

Moore, J. T., and T. E. Lambert, 1993: The use of equivalent potential vorticity to diagnose regions of conditional symmetric instability. *Wea. Forecasting*, **8**, 301–308.

Moore, R. W., M. T. Montgomery, and H. C. Davies, 2008: The integral role of a diabatic rossby vortex in a heavy snowfall event. *MWR*, **136**, 1878–1897.

Mossop, S. C., 1970: Concentrations of ice crystals in clouds. *Bull. Amer. Meteor. Soc.*, **51**, 474–479.

Mote, T. L., D. W. Gamble, S. J. Underwood, and M. L. Bentley, 1997: Synoptic-scale features common to heavy snowstorms in the southeast United States. *Wea. Forecasting*, **12**, 5–23.

Namias, J., 1939: The use of isentropic analysis in short range forecasting. *J. Aeronaut. Soc.*, **5**, 295–298.

Nicosia, D. J., and R. H. Grumm, 1999: Mesoscale band formation in three major northeastern United States snowstorms. *Wea. Forecasting*, **14**, 346–368.

Nietfeld, D. D., and D. A. Kennedy, 1998: Forecasting snowfall amounts: An ingredients-based methodology supporting the Garcia method. Preprints *16^{th} Conf. on Weather Analysis and Forecasting*, Amer. Meteor. Soc., Phoenix, AZ, 385–387.

Niziol, T. A., W. R. Snyder, and J. S. Waldstreicher, 1995: Winter weather forecasting throughout the eastern United States. Part IV: Lake effect snow. *Wea. Forecasting*, **10**, 61–77.

NOAA, 2005: New priorities for the 21st century – NOAAs strategic plan. Tech. rep., National Oceanic and Atmospheric Administration, United States Department of Commerce, [Available online at http://www.ppi.noaa.gov/pdfs/Strategic_Plans/NOAA_Strategic_Plan.pdf].

Novak, D. R., L. F. Bosart, D. Keyser, and J. S. Waldstreicher, 2004: An observational study of cold season-banded precipitation in Northeast U.S. cyclones. *Wea. Forecasting*, **19**, 993–1010.

Novak, D. R., B. A. Colle, and A. R. Aiyyer, 2010: Evolution of mesoscale precipitation band environments within the comma head of northeast u.s. cyclones. *Monthly Weather Review*, **138**, 2354–2374.

Novak, D. R., B. A. Colle, and R. McTaggart-Cowan, 2009: The role of moist processes in the formation and evolution of mesoscale snowbands within the comma head of Northeast U.S. Cyclones. *MWR*, **137**, 2662–2686.

Novak, D. R., J. S. Waldstreicher, D. Keyser, and L. F. Bosart, 2006: A forecast strategy for anticipating cold season mesoscale band formation within eastern U.S. cyclones. *Wea. Forecasting*, **21**, 3–23.

Olsen, D. A., N. W. Junker, and B. Korty, 1995: Evaluation of 33 years of quantitative precipitation forecasting at the NMC. *Wea. Forecasting*, **10**, 498–511.

Palmen, E., and C. Newton, 1951: On the three-dimensional motions in an outbreak of polar air. *J. Atmos. Sci.*, **8**, 25–39.

Palmen, E., and C. W. Newton, 1969: *Atmospheric Circulation Systems*. Academic Press, 603 pp.

Penner, C., 1955: A three-front model for synoptic analyses. *Quart. J. Roy. Meteor. Soc.*, **81**, 89–91.

Petterssen, S., 1956: *Weather Analysis and Forecasting*. Vol. 1. McGraw-Hill, 428 pp.

Posselt, D. J., and J. E. Martin, 2004: The effect of latent heat release on the evolution of a warm occluded thermal structure. *Mon. Wea. Rev.*, **132**, 578–599.

Power, B. A., P. W. Summers, and J. D'Avignon, 1964: Snow crystal forms and riming effects as related to snowfall density and general storm conditions. *J. Atmos. Sci.*, **21**, 300–305.

Pruppacher, H. R., and J. D. Klett, 1997: *Microphysics of Clouds and Precipitation*. Kluwer, 954pp.

Roebber, P. J., 1984: Statistical analysis and updated climatology of explosive cyclones. *MWR*, **112**, 1577–1589.

Roebber, P. J., S. L. Bruening, D. M. Schultz, and J. V. Cortinas Jr., 2003: Improving snowfall forecasting by diagnosing snow density. *Wea. Forecasting*, **18**, 264–287.

Rogers, D. C., 1974: The aggregation of natural ice crystals. Rep. No. AR 110, Dept. Atmos. Resources, University of Wyoming, 35 pp.

Rogers, R. R., and M. K. Yau, 1989: *A Short Course in Cloud Physics*. Pergamon Press, 229 pp.

Sanders, F., 1986a: Explosive cyclogenesis in the west-central north atlantic ocean, 198184. part i: Composite structure and mean behavior. *MWR*, **114**, 1781–1794.

—, 1986b: Frontogenesis and symmetric stability in a major New England snowstorm. *Mon. Wea. Rev.*, **114**, 1847–1862.

Sanders, F., and L. F. Bosart, 1985a: Mesoscale structure in the Megalopolitan snowstorm, 11–12 February 1983. Part II: Doppler radar study of the New England snowband. *J. Atmos. Sci.*, **42**, 1398–1407.

—, 1985b: Mesoscale structure in the Megalopolitan snowstorm of 11–12 February 1983. Part I: Frontogenetical forcing and symmetric instability. *J. Atmos. Sci.*, **42**, 1050–1061.

Schmit, L., and T. Hultquist, 2009: A synoptic climatology of winter storms in the Twin Cities area. Preprints *23rd Conf. on Weather Analysis and Forecasting*, Omaha, NE, Amer. Meteor. Soc., JP3.8. [Available online at http://ams.confex.com/ams/pdfpapers/154067.pdf].

Schultz, D. M., 2001: Reexamining the cold conveyor belt. *Mon. Wea. Rev.*, **129**, 2205–2225.

Schultz, D. M., J. V. Cortinas Jr., and C. A. Doswell, 2002: Comments on "An operational ingredients-based methodology for forecasting midlatitude winter season precipitation.". *Wea. Forecasting*, **17**, 160–167.

Schultz, D. M., and P. N. Schumacher, 1999: The use and misuse of CSI. *Mon. Wea. Rev.*, **127**, 2709–2932.

Schumacher, P. N., 2001: Looking for a trowal: The January 29-30 snowstorm. [Available online at http://www.crh.noaa.gov/fsd/science/snow010130/index.php].

Shaw, W. N., 1911: *Forecasting Weather*. Van Nostrand, 380 pp.

Shaw, W. N., and R. G. K. Lempfert, 1906: *The life history of surface air currents. Met Office Memoir 174. Reprint, Selected Meteorological Papers of Sir Napier Shaw*. MacDonald and Co., 15-131.

Spiegler, D. B., and G. E. Fisher, 1971: A snowfall predicition method for the Alantic seaboard. *Mon. Wea. Rev.*, **99**, 311–325.

Stuart, N. A., and Coauthors, 2006: The future of humans in an increasingly automated forecast process. *Bull. Amer. Meteor. Soc.*, **87**, 1497–1502.

Stuart, N. A., and R. H. Grumm, 2006: Susing wind anomalies to forecast East Coast winter storms. *WAF*, **21**, 952–968.

Sutcliffe, R. C., and A. G. Forsdyke, 1950: The theory and use of upper air thickness patterns in forecasting. *Quart. J. Roy. Meteor. Soc.*, **76**, 189–217.

Thomas, B. C., and J. E. Martin, 2007: A synoptic climatology and composite analysis of the Alberta clipper. *Wea. Forecasting*, **22**, 315–333.

Uccellini, L. W., and P. J. Kocin, 1987: The interaction of jet streak circulations during heavy snow events along the East Coast of the United States. *Wea. Forecasting*, **2**, 298–308.

Uccellini, L. W., P. J. Kocin, R. S. Schneider, P. M. Stokols, and R. A. Dorr, 1995: Forecasting the 12–14 March 1993 Superstorm. *Bull. Amer. Meteor. Soc.*, **76**, 183–199.

Waldstreicher, J. S., 2001: The importance of snow microphysics for large snowfalls. [Available online at http://www.erh.noaa.gov/er/hq/ssd/snowmicro/sld001.html].

Weisman, R. A., K. G. McGregor, D. R. Novak, J. L. Selzler, M. L. Spinar, B. C. Thomas, and P. Schumacher, 2002: Precipitation regimes during cold-season central U.S. inverted trough cases. Part I: Synoptic climatology and composite study. *Wea. Forecasting*, **17**, 1173–1193.

Wetzel, S. W., and J. E. Martin, 2001: An operational ingredients-based methodology for forecasting midlatitude winter season precipitation. *Wea. Forecasting*, **16**, 156–167.

Wilks, D. S., 2006: *Statistical Methods in the Atmospheric Sciences*. 2nd ed. Academic Press, 627 pp.

Zhang, F., C. Snyder, and R. Rotunno, 2002: Mesoscale predictability of the "surprise" snowstorm of 24–25 January 2000. *Mon. Wea. Rev.*, **130**, 1617–1632.